Dissertation
submitted to the
Combined Faculties for the Natural Sciences and for
Mathematics
of the Ruperto-Carola University of Heidelberg, Germany

for the degree of
Doctor of Natural Sciences

presented by
Dipl.-Phys. **Viola Droujinina**
born in Olonec (Russia)

Oral examination: 23th July, 2003

On
Quantum Reflection
and
The Casimir Effect
application to atom-surface scattering

Referees:
Priv.-Doz. Dr. Maarten DeKieviet
Prof. Dr. Siegried Hunklinger

Zusammenfassung: Quantenreflexion des leichten neutralen und oberflächenempfindlichen ^{3}He-Atoms ist eine neue Methode zur Untersuchung des langreichweitigen attraktiven Atom-Oberflächen-Potentials. In dieser Dissertationsschrift wird die detaillierte Analyse der experimentellen Daten präsentiert, die mit dem ^{3}He-Spinecho-Spektrometer bei streifender Streuung des Atomstrahls von einer stark ungeordneten dielektrischen α-Quarzoberfläche und von einer atomar rauhen Au-(111)-Oberfläche aufgenommen wurden. Die Daten werden im Rahmen der vor kurzem entwickelten Theorie von Friedrich *et al.* interpretiert. Der Quantenreflexionskoeffizient wurde bei Energien zwischen μeV und neV gemessen und nimmt um ca. 5 Grössenordnungen zu. Die Parameter des langreichweitigen attraktiven Casimir-van der Waals-Potentials, die aus den Datenanpassungen extrahiert wurden, stimmen hervorragend mit den Literaturwerten überein. Die Analyse des Reflexionskoeffizienten von der α-Quarzoberfläche im Grenzbereich hoher Energien bestätigt das asymptotische Verhalten, das durch das nicht-retardierte van der Waal-Potential bestimmt ist. Das Experiment am ^{3}He-Au(111)-System stellt die erste quantitative Messung des Casimir-effekts bei der Wechselwirkung eines Atoms mit einer Oberfläche dar.

Abstract: Quantum reflection of the light, neutral and surface sensitive ^{3}He-atom is a novel method for investigating long-range attractive atom-surface potentials. This thesis presents the detailed analysis of experimental data obtained with the Atomic Beam Spin Echo (ABSE) spectrometer by scattering ^{3}He from a strongly disordered α-quartz dielectric surface and from an atomically rough gold surface under grazing incidence. The data are interpreted in terms of the quantum reflection theory recently developed by Friedrich *et al.*. The quantum reflection coefficient is measured at energies from μeV down to neV and increases by approximately 5 orders of magnitude. The influence of surface disorder is modelled and properly taken into account. The parameters of the long-range attractive Casimir-van der Waals potential extracted from the fits to the corrected data show excellent agreement with the values given in literature. The analysis of the reflection coefficient from α-quartz forms the first experimental confirmation of the high-energy asymptotic behavior determined by the non-retarded van der Waals potential. The scattering experiment on the ^{3}He-Au(111) system represents the first quantitative measurement of the Casimir effect for the interaction of a single atom with a single conductive surface.

To the memory of my grandmother
Jevgenia Petrovna Silina.

We live in a system of approximations.
Ralph Waldo Emerson (1844)

Contents

Chapter 1

Introduction

Many physical processes completely change their behavior at very low energies. Suprising quantum phenomena may occur when the wave nature of an atom becomes dominant with respect to its classical, particle-like behavior. The rapidly developing experimental techniques in atomic and solid state physics now allow consequent investigation of these phenomena, which so far were known only theoretically. One example of such a phenomenon is quantum mechanical above-barrier reflection of slow atoms, with incident kinetic energy exceeding the barrier height. Interestingly, the barrier does not need to be repulsive. In the quantum regime, reflection also takes place from a purely attractive potential, which falls off with distance r faster than r^{-2}.

In literature, quantum reflection (QR) was firstly used to describe the "non-sticking" of atoms to a surface upon ultracold collisions. Already 1936, the sticking coefficient was predicted to vanish at low incident energy proportionally to the normal momentum of the atom [Lennard-Jones and Devonshire, 1936]. This behavior of the sticking coefficient at very low energies is, however, the result of QR from the purely attractive part of the interaction potential which occurs long before the atom reaches the repulsive wall. The theoretical description of quantum mechanical above-barrier reflection was developed for the general case by [Pokrovskii et al., 1958]. This theory has been extended by [Friedrich et al., 2002] to very low scattering energies. For the system atom-surface this extended theory is presented in chapter 2. The term QR is also used in literature for the above-barrier reflection of slow atoms from an evanescent-wave mirror [Segev et al., 1997, Côté et al., 1998, Henkel et al., 1996]. The nature of this effect is identical to QR of an atom from a surface. In both systems, coupling to the short-range repulsive part of the interaction potential is absent. However, the shape of the barrier is quite different in the two cases.

The experiment on scattering of a ^{3}He atomic beam from a microscopically disordered α-quartz surface at grazing incidence was performed with the ^{3}He atomic beam spectrometer in our group. At that time the extented QR-theory was not yet published. The measured specularly reflected intensity approximately shows an exponential dependence of the cosine of the beam incident angle with respect to the surface normal. We initially tried to explain the data as semi-classical reflection from an adsorbing potential. The latter is defined by a complex function, the imaginary part of which appears because of the surface disorder. Since the de Broglie wavelength of slow atoms is large and the wave function vanishes at the classical turning point on the repulsive wall an increasingly large part of the wave function does not progress to above the potential. One then expects that the reflection probability for slow atoms increases. The simulation of the reflection coefficient was performed using the program described in Sec. 4.3.1. However, it was impossible to reproduce the experimental data quantitatively even at large values of the imaginary part of the potential. The strong deviation of the simulated values from the experimental data demonstrated that the measured reflection could not be explained by semi-classical scattering from a strongly adsorbing potential.

The next step was to simulate QR from a truncated potential in order to suppress reflection from the repulsive part of the potential. Again, no quantitative agreement between theory and experiment was achieved. The reason was the superposition of two non-separable quantum mechanical reflection effects: QR from the attractive part and reflection from the truncated edge of the potential (see Sec. 4.3.1). After the extended theory on QR was published we tried to simulate the quantum reflection coefficient using the same simulation program with a purely attractive potential. However, the singularity of the potential function close to the surface again produced additional quantum mechanical reflection making impossible to extract the experimentally measured QR-effect. Finally, a new simulation program was developed based on the suggestions given in [Côté et al., 1997] and which is discussed in Sec. 2.2. The simulated values for the reflection coefficient are in excellent agreement with the experimental data when taking into account the influence of surface disordering. Since the experiment is performed at energies perpendicular to the surface in the range from μeV down to neV QR occurs at the distance 3-10 nm from the surface. At such energies the asymptotic behavior of the QR coefficient determined by the non-retarded van der Waals potential, given by a simple form in chapter 2, was confirmed for the first time [Druzhinina and DeKieviet, 2002].

Being very sensitive to the local value of the potential, the measurement of the QR coefficient as a function of the energy of the incident atom is

a powerful instrument for the investigation of long-range attractive atom-surface potentials. The very delicate Casimir effect, which is presented in chapter 3, can thus be quantitatively studied. A corresponding measurement using ^{3}He scattering from Au(111) is analyzed in detail in chapter 4. The possibility of measuring QR and therewith probing the attractive potential very close to the surface allows to investigate surface roughness and disorder by means of ^{3}He atomic beam scattering in future experiments. Due to the properties of QR, an atomically rough or a specially prepared surface (see Sec. 4.4) can eventually be used as an efficient mirror for ultra-cold atoms.

Chapter 2

Theory of quantum reflection

This chapter presents the theoretical description of quantum reflection by [Pokrovskii et al., 1958, Friedrich et al., 2002]. A numerical model is developed based on the suggestions of [Côté et al., 1997] in order to interpret recent experiments (see chapter 4). The different energy criteria for the occurence of quantum reflection given in literature are evaluated and compared. Analytic expressions for the asymptotic behavior of the reflection coefficient are derived. The validity range for the high-energy asymptote of quantum reflection coefficient is calculated. Recent experimental results on quantum reflection close to the high-energy range obtained with the ^{3}He spectrometer are excellently described by the extended theory of quantum reflection. The universal form of the sticking coefficient is shown to appear only in the low-energy quantum regime which is also detailed in this chapter.

2.1 From classical to quantum reflection

2.1.1 Classical reflection

Before we speak about reflection in the frame of quantum mechanics, it is necessary to clarify, what "reflection" means in classical mechanics. In the course of this work we concentrate on the system of an atom scattering from the surface of a solid body. In this case, the basic understanding of the nature of reflection is obtained by treating the problem in one dimension. Because of averaging of the interaction parallel to the surface only the perpendicular motion is important. The perpendicular interaction potential, $V(r)$, as a function of the distance between an atom and a surface, r, is schematically illustrated in Fig. 2.1 (a).

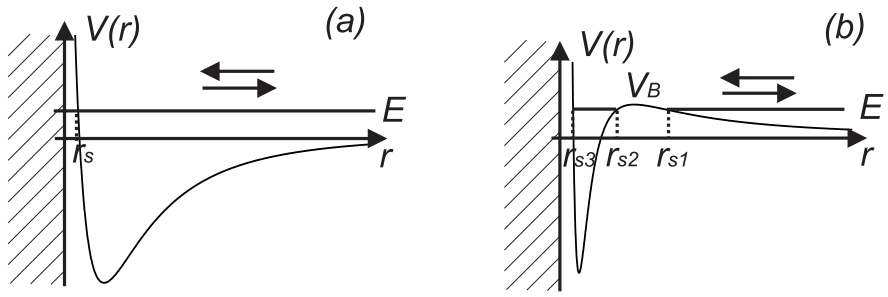

Figure 2.1: (a) Schematic representation of the interaction potential between an atom with the initial kinetic energy E and a surface situated at $r = 0$. r_s denotes the classical turning point, $V(r_s) = E$, from which an impinging atom is reflected (indicated by the arrows). (b) A potential barrier of height V_B can e.g. be caused by a layer of adsorbed molecules on the surface. r_{s1} denotes the classical turning point, r_{s2} and r_{s3} are additional points at which $V(r_s) = E$.

Classical turning point An incident atom with primary kinetic energy E is accelerated towards the surface from infinity due to the long-range attractive potential. At a few Angström before hitting the surface it slows down through the short-range repulsive potential, resulting from the overlap of the electrons of the incident atom and the surface atoms. At the distance r_s the potential energy $V(r_s)$ is equal to the total energy of the atom-surface system, E, so that the kinetic energy $E_{kin} = E - V(r_s)$ vanishes. The velocity of the atom with mass m at the distance r_s is given by $v(r_s) = \sqrt{2E_{kin}/m} = 0$. Thus, at this distance the atom stops. Before the atom reaches the point r_s the total energy exceeds the potential energy ($E > V(r)$), and the atom velocity $v(r) = \sqrt{2(E - V(r))/m}$ is real. But at distances $r < r_s$ the potential energy $V(r) > E$ and the atom velocity $v(r) = i\sqrt{2(V(r) - E)/m}$ is an imaginary value. From the classical point of view observables such as velocity must be real to have a physical meaning. The motion of the atom at the distances $r < r_s$ is therefore classically forbidden. This means that the atom reaching the point r_s stops there and turns back, i.e. it is reflected, as depicted in Fig. 2.1 (a). The coordinate r_s, at which reflection occurs, is called classical turning point.

The same classical reflection can occur from a potential barrier, if the primary kinetic energy E is lower than the barrier height V_B. Such barrier can be created, for instance, by molecules adsorbed on a surface. As shown in

Fig. 2.1 (b), there are three points r_{s1}, r_{s2} and r_{s3}, at which $E = V$. However, there is only one turning point r_{s1}, from which the atom is reflected, because the motion at r between r_{s1} and r_{s2} is classically forbidden. If the energy E exceeds the barrier height V_B there is again only one turning point r_{s3} at the repulsive wall. This case corresponds to the one illustrated in Fig. 2.1 (a). If the repulsive wall were absent, the atom would not be reflected at all. This means that there is no above-barrier reflection in the classical representation.

2.1.2 Semi-classical representation.

In analogy to the dual nature of light one describes particles with mass m quantum mechanically as a wave with the de Broglie wavelength $\lambda_{dB} \propto (mv)^{-1}$, where v is the velocity of the particle. The value of λ_{dB} determines how well the physical process, which involves the particle, can be described classically. For light and fast moving particles (small λ_{dB}) the dynamics only slightly differs from classical motion. This is true, for instance, for the deviation of a beam of electrons in an electron-beam tube or for scattering of thermal atoms from a surface. Such systems can be treated in the frame of semi-classical approximation. In this approximation, a usually complicated wave function can be substantially simplified.

Debye-Waller-Factor and Beeby correction When reaching the classical turning point at the repulsive wall of the interaction potential the incident wave would be completely reflected, if the crystal lattice atoms were absolutely rigid. There are, however, thermal lattice oscillations, which lead to a reduction of the elastically reflected wave intensity by the well-known Debye-Waller-Factor $D = \exp(-4k_\perp^2 \langle u_\perp^2 \rangle)$. Here, $\langle u_\perp^2 \rangle$ denotes the mean square deviation of the lattice atom from its equilibrium position and $k_\perp = k_0 \cos\theta_i$ is the wave number perpendicular to the surface of the wave impinging under the angle θ_i with respect to the surface normal. Since the oscillations of the lattice atoms increase with surface temperature T_s, the dependence of the Debye-Waller-Factor on the surface temperature is given by [Hellwege, 1981]

$$D(T_s) = \exp\left(-3k_\perp^2 \frac{\hbar^2}{m_s k_B \Theta_{D_\perp}} P(\frac{T_s}{\Theta_{D_\perp}})\right), \tag{2.1}$$

with

$$P(\frac{T_s}{\Theta_{D_\perp}}) = 1 + 4\left(\frac{T_s}{\Theta_{D_\perp}}\right)^2 \int_0^{\Theta_{D_\perp}/T_s} \frac{dy\, y}{e^y - 1}. \tag{2.2}$$

Here, m_s and k_B denote the mass of a surface atom and the Boltzmann constant, respectively. $\Theta_{D_\perp}$ stands for the Debye temperature perpendicular to the surface, which is a material constant with typical values between

1/4 and 3/4 of the bulk Debye temperature. At $T_s/\Theta_{D_\perp} \gg 1$ the function $P(T_s/\Theta_{D_\perp}) \simeq 4T_s/\Theta_{D_\perp}$ and $D(T_s) \simeq \exp(-12k_\perp^2\hbar^2 T_s/(m_s k_B \Theta_{D_\perp}^2))$. At $T_s/\Theta_{D_\perp} \ll 1$ the function $P(T_s/\Theta_{D_\perp})$ takes approximately the value $1 + (2\pi^2/3)(T_s/\Theta_{D_\perp})^2$ and the Debye-Waller-Factor will be about $D(T) \simeq \exp(-3k_\perp^2\hbar^2/(m_s k_B \Theta_{D_\perp})) \times \exp(-2\pi^2 k_\perp^2 \hbar^2 T_s^2/(m_s k_B \Theta_{D_\perp}^3))$. Even at $T_s = 0$ the lattice atoms perform zero-temperature oscillations and the elastically scattered intensity is reduced by the factor $\exp(-3k_\perp^2\hbar^2/(m_s k_B \Theta_{D_\perp}))$. For a gold surface (Au(111)) the perpendicular Debye temperature is measured in our group by using ^{3}He-atom scattering to be (135 ± 10) K [Stöferle, 2001].

Since the incident wave "feels" the lattice oscillations at the distance of some Angström before reaching the surface, the so-called Beeby correction can be applied. This correction assumes, that the atom accelerating into the potential well is reflected from the classical turning point, which lies at the hard repulsive wall (see Fig. 2.2, Eq. (2.23)). The fact, that the repulsive part of the potential is in fact soft, is not taken into account because of its effective range being only some Angström. The wave number $k_\perp$ in the expression (2.1) is corrected by Beeby to [Beeby, 1971]

$$k_\perp = k_0 \sqrt{\cos^2\theta_i + \frac{V_0}{E}}. \tag{2.3}$$

Here, V_0 and E denote the value of the potential depth and the incident kinetic energy, respectively. k_0 is the initial wave number, $k_0 = \sqrt{2mE/\hbar^2}$.

In the experiment discussed in this work, the incident kinetic energy of the wave E is of order of 1 meV and the value of the potential depth V_0 is approximately equal to 10 meV. The perpendicular wave number $k_\perp \simeq k_0\sqrt{V_0/E}$ and the Debye-Waller-Factor are thus expected to be independent of the incident angle θ_i.

WKB-approximation In quantum mechanics, the wave function of an atom is represented by a complex function $\Psi(r) = e^{i\,S(r)/\hbar}$. Atom-surface scattering processes are generally gouverned by the stationary Schrödinger equation

$$-\frac{\hbar^2}{2m}\frac{d^2\Psi(r)}{dr^2} + (V(r) - E)\,\Psi(r) = 0. \tag{2.4}$$

From this equation we find an expression for the phase of the wave function $S(r)$,

$$\frac{1}{2m}\left(\frac{dS(r)}{dr}\right)^2 - \frac{i\hbar}{2m}\cdot\frac{d^2S(r)}{dr^2} + V(r) - E = 0. \tag{2.5}$$

In equations (2.4) and (2.5) $V(r)$ represents the local potential energy of an atom at distance r from the surface, and E is the primary kinetic energy of

the atom before interacting with the surface. The solution of Eq. (2.5) is found in the form of a series

$$S = \sum_{n=0}^{\infty} S_n \left(\frac{\hbar}{i}\right)^n . \tag{2.6}$$

The coefficients S_n are independent on $\hbar$. By placing Eq. (2.6) into Eq. (2.5) we obtain

$$\frac{1}{2m}\left(\frac{dS_0}{dr} + \frac{\hbar}{i}\cdot\frac{dS_1}{dr} + ...\right)^2 - \frac{i\hbar}{2m}\left(\frac{d^2S_0}{dr^2} + \frac{\hbar}{i}\cdot\frac{d^2S_1}{dr^2} + ...\right) + V(r) = E. \tag{2.7}$$

There are two ways to state a validity condition of the semi-classical Wentzel-Kramers-Brillouin (WKB) approximation, which are described and compared below:

- The first way is to compare the coefficients of $\hbar$ in the terms of identical order in $\hbar$ in Eq. (2.7) [Davydov, 1976]. We obtain the set of equations

$$\hbar^0 : \quad \frac{1}{2m}\left(\frac{dS_0}{dr}\right)^2 + V(r) = E, \tag{2.8}$$

$$\hbar^1 : \quad 2\frac{dS_0}{dr}\cdot\frac{dS_1}{dr} + \frac{d^2S_0}{dr^2} = 0, \tag{2.9}$$

$$\dots \tag{2.10}$$

Eq. (2.8) is the classical Hamilton-Jacoby equation and its solution is given by

$$S_0 = \pm\int_{r_0}^{r} p(r)dr, \tag{2.11}$$

where $p(r) = \sqrt{2m(E - V(r))}$ represents the momentum of the particle at distance r from the surface. By substituting Eq. (2.11) into Eq. (2.9) we obtain the expression for S_1,

$$S_1 = -\frac{1}{2}\ln p(r) + const. \tag{2.12}$$

Thus, to an accuracy of the first order of $\hbar$, $S(r)$ is given by

$$S(r) = \pm\int_{r_0}^{r} p(r)dr - \frac{1}{2}\cdot\frac{\hbar}{i}\ln p(r) + const_1 \tag{2.13}$$

and the wave function of the particle for $E > V(r)$ has the well-known form of the wave function in the semi-classical approximation,

$$\Psi(r) = C_1\frac{1}{\sqrt{p(r)}}\exp\left[\frac{i}{\hbar}\int_{r_0}^{r} p(r)dr\right] + C_2\frac{1}{\sqrt{p(r)}}\exp\left[-\frac{i}{\hbar}\int_{r_0}^{r} p(r)dr\right], \tag{2.14}$$

where C_1 and C_2 are some constants. At the classical turning point ($E = V$) the momentum $p(r)$ vanishes and expression (2.14) becomes unphysical. Obviously, the interval of coordinates, in which the particle wave function is given by Eq. (2.14), must not contain classical turning points.

The semi-classical approximation is defined through the fact that the terms in equation (2.7) containing $\hbar$ in the first order, which are of quantum mechanical nature, contribute much less than the zero-order term of classical nature,

$$\left|\frac{1}{2m}\left(\frac{dS_0}{dr}\right)^2\right| \gg \left|\frac{2\hbar}{2mi}\cdot\frac{dS_0}{dr}\cdot\frac{dS_1}{dr} - \frac{i\hbar}{2m}\cdot\frac{d^2S_0}{dr^2}\right|. \tag{2.15}$$

Taking into account that $dS_0/dr = \pm p(r)$ and $dS_1/dr = -(2p(r))^{-1}\, dp(r)/dr$ we obtain the well-known WKB-approximation

$$\boxed{\frac{\hbar}{p^2(r)}\left|\frac{dp(r)}{dr}\right| \ll 1} \tag{2.16}$$

or in terms of the potential gradient

$$\boxed{\frac{\hbar m}{p^3(r)}\left|\frac{dV(r)}{dr}\right| \ll 1.} \tag{2.17}$$

Thus, the semiclassical approximation is valid for fast particles (large $p(r)$) moving in a slowly varying potential (small $dV(r)/dr$).

- The second way to define the validity of the semiclassical approximation is to solve equation (2.7) for its real and imaginary parts separately (thereby the phase S is taken with an accuracy up to the first order of $\hbar$, $S = S_0 + \frac{\hbar}{i}S_1$),

$$\Re: \quad \frac{1}{2m}\left(\frac{dS_0}{dr}\right)^2 - \frac{\hbar^2}{2m}\left(\left(\frac{dS_1}{dr}\right)^2 + \frac{d^2S_1}{dr^2}\right) + V(r) = E, \tag{2.18}$$

$$\Im: \quad 2\frac{dS_0}{dr}\cdot\frac{dS_1}{dr} + \frac{d^2S_0}{dr^2} = 0. \tag{2.19}$$

Eq. (2.19) is similar to expression (2.9) and Eq. (2.18) tends to the classical Hamilton-Jacoby equation (2.8) if

$$\left|\frac{\hbar^2}{2m}\left(\left(\frac{dS_1}{dr}\right)^2+\frac{d^2S_1}{dr^2}\right)\right| \ll \left|\frac{1}{2m}\left(\frac{dS_0}{dr}\right)^2\right|. \tag{2.20}$$

By placing into this inequality the expressions for dS_0/dr and dS_1/dr we obtain an alternative condition for the validity of the WKB-approximation,

$$\boxed{\left|\frac{\hbar^2}{p^{3/2}(r)}\cdot\frac{d^2p^{-1/2}(r)}{dr^2}\right| \ll 1.} \tag{2.21}$$

This criterion for the semi-classical approximation is introduced in [Friedrich, 1994].

Which one of these conditions of validity of the WKB-approximation is more accurate, we will see in section 2.3. The left parts in the inequalities (2.16-2.17) and (2.21) are named "badlands functions".

2.1.3 Badlands functions

The badlands function $B(r)$ determines, how well the semi-classical theory is applicable at some distance r from the surface. At very low primary kinetic energy of the incident atom the WKB-approximation breaks down. As detailed in the next section, the break down occurs in the vicinity of the distance r_0, at which the absolute values of the incident kinetic and local potential energies are equal, $E = |V(r_0)|$ (see Fig. 2.2). In this case quantum reflection appears, which is a purely quantum mechanical effect and cannot be explained by classical or semi-classical theory.

Some theoretical works ([Böheim and Brenig, 1982], [Carraro and Cole, 1998]) have suggested that the occurence of quantum reflection is correlated to the break-down of the WKB approximation. These works calculate the critical value of the incident kinetic energy, below which quantum reflection takes place. For this, the dependence of the maximum of the badlands function on incident energy has to be analyzed. If the maximum of the badlands function $|Max[B(r)]| \ll 1$ then the WKB approximation is valid and no quantum reflection is expected. If however $|Max[B(r)]|$ is comparable or even larger than unity, then the semi-classical

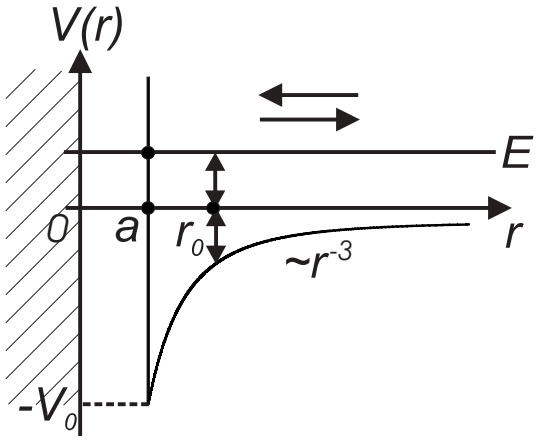

Figure 2.2: Schematic representation of a hard wall atom-surface interaction potential described by Eq. (2.23). $V_0 = |V(a)|$ denotes the potential depth. At the distance r_0 the absolute value of the potential energy is equal to the initial kinetic energy of the incoming atom, $|V(r_0)| = E$.

approximation breaks down and quantum reflection occurs in the vicinity of the position of the maximum of the badlands function.

In this section we discuss the dependence on distance and energy of the badlands functions $|B_1(r)| = |\hbar p^{-2}(r)\ dp(r)/dr|$ (2.16) and $|B_2(r)| = |\hbar^2 p^{-3/2}(r)\ \ d^2p^{-1/2}(r)/dr^2|$ (2.21). We will show that the location of $|Max[B_2(r)]|$ approximately coincides with the distance r_0.

For simplicity we consider the homogeneous non-retarded attractive interaction potential

$$V(r) = -\frac{\hbar^2}{2m} \cdot \frac{\beta_n^{n-2}}{r^n} \tag{2.22}$$

depending on the length parameter β_n and scaling as the $(-n)$-th power of the distance r. Moreover, this potential will be identified with the attractive part of the total hard wall non-retarded interaction potential

$$V_{total}(r) = \begin{cases} V(r) = -V_0 \frac{a^3}{r^3} & \text{at } r \geq a, \\ +\infty & \text{at } r < a. \end{cases} \tag{2.23}$$

Here, a and V_0 denote the position and absolute value of the potential minimum, respectively (see Fig. 2.2). This representation allows easy comparison of our calculations with literature. By normalizing the coordinate r to a ($r \to r/a$) we obtain the dimensionless attractive potential $-2ma^2V(r)/\hbar^2 = -g^2/r^n$ and local wave number $k(r) = \sqrt{k_0^2 + g^2/r^n}$ with the dimensionless parameter $g = \sqrt{2ma^2V_0/\hbar^2} = \beta_n^{(n-2)/2}$, representing the coupling constant.

The location of the maximum of the badlands function, r_{max}, is obtained from solving the equation

$$\left.\frac{dB(r)}{dr}\right|_{r_{max}} = 0. \tag{2.24}$$

The calculated maxima of the badlands functions

$$B_1(r) = \frac{\hbar}{p^2(r)} \cdot \frac{dp(r)}{dr} = \frac{1}{k^2(r)} \cdot \frac{dk(r)}{dr} = \frac{\beta_n^{n-2} n}{2k^3(r) r^{n+1}}, \tag{2.25}$$

$$B_2(r) = \frac{\hbar^2}{p^{3/2}(r)} \cdot \frac{d^2 p^{-1/2}(r)}{dr^2} = \frac{5n^2 \beta_n^{2n-4}}{16 r^{2n+2} k^6(r)} - \frac{n(n+1)\beta_n^{n-2}}{4 r^{n+2} k^4(r)} \tag{2.26}$$

are located at the distances

$$r_{max}^{(1)} = k_0^{-\frac{2}{n}} \left[\frac{(n-2)\beta_n^{n-2}}{2(n+1)}\right]^{\frac{1}{n}}, \tag{2.27}$$

$$r_{max_{1,2}}^{(2)} = k_0^{-\frac{2}{n}} \left[\beta_n^{n-2} F(n)_\pm\right]^{\frac{1}{n}} \tag{2.28}$$

with $F(n)_\pm = \frac{5}{4} - \frac{9}{2(n+2)} \pm \frac{9n}{4(n+2)}\sqrt{1 - \frac{20}{27}\frac{n+2}{n+1}}$. The lower indices 1 and 2 in expression (2.28) denote the fact that for some potential power n two maxima of $B_2(r)$ appear. Plus and minus in $F(n)_\pm$ correspond to the first and the second maximum of $B_2(r)$, respectively. The upper indices (1) and (2) in expressions (2.27) and (2.28) and in the following indicate the correspondence to the first and second badlands function, respectively.

Taking into account, that $\beta_n^{n-2} k_0^{-2/n} = r_0$, we can calculate the positions of the maxima as compared to the distance r_0,

$$r_{max}^{(1)} = \left[\frac{n-2}{2(n+1)}\right]^{\frac{1}{n}} \cdot r_0, \tag{2.29}$$

$$r_{max_{1,2}}^{(2)} = F(n)_\pm^{\frac{1}{n}} \cdot r_0. \tag{2.30}$$

The same results are presented for $r_{max}^{(1)}$ in [Carraro and Cole, 1998] and for $r_{max_{1,2}}^{(2)}$ in [Friedrich et al., 2002]. The maximal values of $B_1(r)$ and $B_2(r)$, $Max[B_1(r)] = B_1(r_{max}^{(1)})$ and $Max_{1,2}[B_2(r)] = B_2(r_{max_{1,2}}^{(2)})$, are given by

$$Max[B_1(r)] = (k_0\beta_n)^{-(1-\frac{2}{n})} \left[\frac{2(n+1)^{(n+1)}(n-2)^{(\frac{n}{2}-1)}}{(27n)^{\frac{n}{2}}}\right]^{\frac{1}{n}}, \tag{2.31}$$

$$Max_{1,2}[B_2(r)] = (k_0\beta_n)^{-(2-\frac{4}{n})} \frac{F(n)_\pm^{1-\frac{2}{n}}}{4F1(n)_\pm^2} \left(\frac{5n}{4F1(n)_\pm} - n(n+1)\right) \tag{2.32}$$

n	3	4	5	6	7
$F(n)_+$	0.717	1	1.199	1.349	1.464
$F(n)_-$	-0.017	0	0.015	0.026	0.036
$r^{(1)}_{max}/r_0$	0.50	0.67	0.76	0.81	0.85
$r^{(2)}_{max_1}/r_0$	0.895	1	1.037	1.051	1.056
$r^{(2)}_{max_2}/r_0$	–	–	0.431	0.546	0.621
$\lvert B_1(r^{(1)}_{max})\rvert$	$0.89\lvert k_0\beta_3\rvert^{-\frac{1}{3}}$	$1.12\lvert k_0\beta_4\rvert^{-\frac{1}{2}}$	$1.18\lvert k_0\beta_5\rvert^{-\frac{3}{5}}$	$1.36\lvert k_0\beta_6\rvert^{-\frac{2}{3}}$	$1.54\lvert k_0\beta_7\rvert^{-\frac{5}{7}}$
$\lvert B_2(r^{(2)}_{max_1})\rvert$	$0.41\lvert k_0\beta_3\rvert^{-\frac{2}{3}}$	$0.62\lvert k_0\beta_4\rvert^{-1}$	$0.91\lvert k_0\beta_5\rvert^{-\frac{6}{5}}$	$1.26\lvert k_0\beta_6\rvert^{-\frac{4}{3}}$	$1.68\lvert k_0\beta_7\rvert^{-\frac{10}{7}}$
$\lvert B_2(r^{(2)}_{max_2})\rvert$	–	–	$0.02\lvert k_0\beta_5\rvert^{-\frac{6}{5}}$	$0.04\lvert k_0\beta_6\rvert^{-\frac{4}{3}}$	$0.07\lvert k_0\beta_7\rvert^{-\frac{10}{7}}$

Table 2.1: The constants $F(n)_\pm$, the positions of the maxima of the badlands functions compared to r_0 and the absolute values of the maxima of the B-functions for different potential power n.

with $F1(n)_\pm = F(n)_\pm + 1$.

The location and absolute values of the maxima of the badlands functions and also the constants $F(n)_\pm$ are given in Table 2.1 for different potential power n. The maximal absolute values of both B-functions, listed in Table 2.1, do not differ significantly. However, the positions of the maxima are very different. The first maximum of $B_2(r)$ lies near r_0, whereas the maximum of $B_1(r)$ is situated at a distance much closer to the surface. For very small incident energies, when r_0 lies very far from the surface, this difference becomes very important. From two maxima of $B_2(r)$ we take into account only the first, because its value is much larger than the value of the second (see Table 2.1). Since all theoretical works agree that the incident wave is reflected from the vicinity of r_0, we conclude that $B_2(r)$ and not $B_1(r)$ is the badlands function, which determines the WKB-approximation break-down more accurately.

According to [Böheim and Brenig, 1982, Carraro and Cole, 1998], the critical values for the dimensionless product $k_0\beta_n$ and for the incident energy $E = \hbar^2 k_0^2/(2m)$ are obtained from the condition that the absolute value of the maximum of the badlands function reaches unity, i.e.

$$|Max[B_{1,2}(r)]| = 1. \tag{2.33}$$

The calculated critical values for $k_0\beta_n$ are given by

$$(k_0\beta_n)^{(1)}_{crit} = \left[\frac{2(n+1)^{(n+1)}(n-2)^{(\frac{n}{2}-1)}}{(27n)^{\frac{n}{2}}}\right]^{\frac{1}{n-2}}, \tag{2.34}$$

$$(k_0\beta_n)^{(2)}_{crit} = \frac{\sqrt{F(n)_+}}{(2F1(n)_+)^{\frac{2}{n-2}}}\left(\frac{5n}{4F1(n)_+} - n(n+1)\right)^{\frac{1}{n-2}} \tag{2.35}$$

n	3	4	5	6	7
$\lvert k_0\beta_n\rvert^{(1)}_{crit}$	0.702	1.035	1.318	1.578	1.824
$\lvert k_0\beta_n\rvert^{(2)}_{crit}$	0.705	1.046	1.226	1.337	1.412
$E^{(1)}_{crit}/V_0$	$0.49g^{-6}$	$1.07g^{-4}$	$1.74g^{-3.3}$	$2.49g^{-3}$	$3.33g^{-2.8}$
$E^{(2)}_{crit}/V_0$	$0.07g^{-6}$	$0.38g^{-4}$	$0.86g^{-3.3}$	$1.41g^{-3}$	$2.07g^{-2.8}$

Table 2.2: The critical values for $|k_0\beta_n|$ and the incident kinetic energy E with respect to the potential depth V_0, obtained from the two different badlands functions $B_1(r)$ and $B_2(r)$ for different potential power n.

for $Max[B_1(r)]$ and $Max_1[B_2(r)]$, respectively. Correspondingly, for two badlands functions the critical values for the incident kinetic energy $E_{crit} = \hbar^2 k^2_{0_{crit}}/(2m)$ are represented by

$$E^{(1)}_{crit} = V_0 g^{\frac{2n}{2-n}} \left[\frac{4(n+1)^{2(n+1)}(n-2)^{(n-2)}}{(27n)^n}\right]^{\frac{1}{n-2}}, \tag{2.36}$$

$$E^{(2)}_{crit} = V_0 g^{\frac{2n}{2-n}} \frac{F(n)_+}{(2F1(n)_+)^{\frac{4}{n-2}}} \left(\frac{5n}{4F1(n)_+} - n(n+1)\right)^{\frac{2}{n-2}}. \tag{2.37}$$

Table 2.2 gives a list of all calculated critical values for different n, derived from the criterion (2.33). The dependence of $E^{(1)}_{crit}/V_0$ on the parameter g is given in [Böheim and Brenig, 1982]. In this work it was proposed that quantum reflection can appear only at energies smaller or equal to this critical value. Since the g-parameter in real atom-surface systems is of the order of 10, the critical energy is at highest 10^{-6} of the potential depth value V_0 (for the non-retarded potential, $n = 3$). This is a rather coarse estimate, because the WKB-approximation already breaks down at much higher energies than this critical value.

In Table 2.2 the corresponding "critical" values for the dimensionless product $|k_0\beta_n|$ are presented. We see, that these values are of the order of unity. In the following we show, that quantum reflection appears at $|k_0\beta_n| \gg 1$, too. This proves that the criterion (2.33) represents only a very rough estimate. In fact, the experimental data presented below confirm the appearance of quantum reflection at energies much higher than $10^{-6}V_0$.

By taking into account the retardation of the potential at large distances $r \gg l$

$$V(r) = -\frac{\hbar^2}{2m} \cdot \frac{\beta_n^{n-2}}{r^{n-1}(r+l)}, \tag{2.38}$$

the badlands functions have more complicated forms

$$B_1(r) = \frac{\beta_n^{n-2}[l - n(r+l)]}{2k^3(r)r^n(r+l)^2}, \tag{2.39}$$

$$B_2(r) = \frac{5\beta_n^{2n-4}[nr+(n-1)l]^2}{16k^6(r)r^{2n}(r+l)^4} - \frac{\beta_n^{n-2}[n(n+1)r^2+2(n^2-1)rl+n(n-1)l^2]}{4k^4(r)r^{n+1}(r+l)^3} \tag{2.40}$$

with the local wave number $k(r) = \sqrt{k_0^2 + \frac{\beta_n^{n-2}}{r^{n-1}(r+l)}}$. They are larger in systems with a light incident atom or with a weaker potential retardation [Friedrich et al., 2002], avoiding larger values of the quantum reflection coefficient.

2.2 Simulation of quantum reflection

In this section we present a numerical model for simulating quantum reflection. This model is based on assumptions discussed in [Côté et al., 1997]. The idea is to compare the semi-classical wave function with the exact numerical solution of the Schrödinger equation inside the potential, using a matching procedure.

We have already discussed, that quantum reflection occurs in the vicinity of the maximum of the badlands function (see 2.1.3). This maximum lies approximately at the distance r_0, where the absolute values of the incident kinetic and the local potential energies are equal. The smaller the incident energy, the broader the region, which yields non-negligible contributions to quantum reflection.

We will consider the incidence of an atom from $r = -\infty$ onto the surface. Since we calculate the above-barrier reflection from a purely attractive long-range potential, it is correct to say, that there are three intervals of distances r:
1) $r < r_1$, where the WKB approximation is valid. From this interval no quantum reflection appears.
2) $r_2 \leq r \leq r_1$, where the WKB-approximation breaks down. From this interval the incident wave is partially reflected.
3) $r > r_2$, where the WKB approximation is valid again.
The interval boundaries r_1 and r_2 are losely defined by the validity condition of the WKB-approximation.

In the first and third intervals the incident wave function can be given in the usual semi-classical form

$$\Psi(r) = \frac{A}{\sqrt{p(r)}} \exp\left(\frac{i}{\hbar}\int^r p(r')dr'\right). \tag{2.41}$$

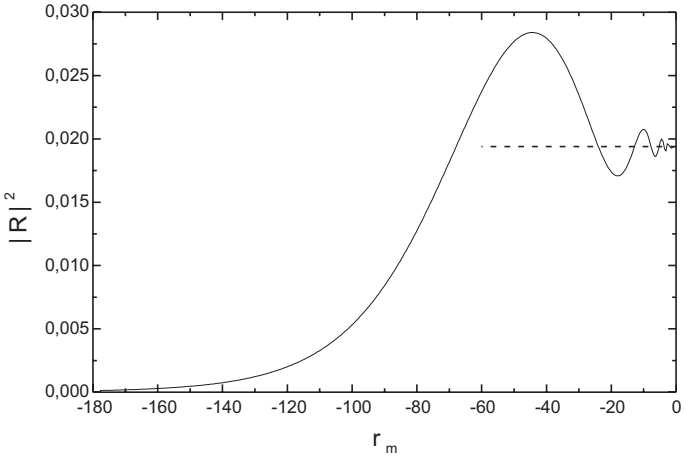

Figure 2.3: The reflection coefficient $|R|^2$ plotted against the matching point r_m. As the atom propagates from $-\infty$ through a badland the reflection coefficient increases. When leaving the badland it oscillates around a well-defined value (here, 0.019), approaching this value at very small r_m. The higher the incident energy, the quicker the reflection approaches a constant value since the badland region becomes narrower.

Because of the occurence of the reflection from the second interval we can write the wave function in every interval of distances as

$$\Psi(r) = \frac{A}{\sqrt{p(r)}} \left[\exp\left(\frac{i}{\hbar} \int_{r_m}^{r} p(r)dr \right) + R_{WKB}(r_m) \exp\left(-\frac{i}{\hbar} \int_{r_m}^{r} p(r)dr \right) \right]. \tag{2.42}$$

Here, $r \leq r_m$ and r_m is a matching point, which we discuss below. It is clear, that $R_{WKB}(r_m) = 0$ at $r_m \leq r_1$ since no reflection occurs from the first interval. At $r_m \geq r_2$, the reflection has already occured from the second interval and the third interval does not contribute to reflection at all. Therefore, $R_{WKB}(r_m) = const.$ By shifting r_m through the second (reflecting) interval we can see that $R_{WKB}(r_m)$ changes because of the changing of the local badlands function. At $r \to -\infty$ the wave function has the form (2.47). The expression

$$R = R_{WKB}(r_m) \exp[-i\eta(r_m)] \tag{2.43}$$

connects $R_{WKB}(r_m)$ with the reflection amplitude R. The phase $\eta(r_m)$ has the form

$$\eta(r_m) = 2 \lim_{r \to -\infty} \left(\frac{1}{\hbar} \int_{r_m}^{r} p(r')dr' - k_0 r \right). \tag{2.44}$$

In order to calculate $R_{WKB}(r_m)$ we make use of a matching procedure. We assume that the wave function Eq. (2.42) coincides with the exact solution of the Schrödinger equation $\Psi_1(r)$ with an accuracy of a constant, $\Psi(r) = const\ \Psi_1(r)$. In this case the matching condition

$$\frac{\Psi'(r_m)}{\Psi(r_m)} = \frac{\Psi_1'(r_m)}{\Psi_1(r_m)} \tag{2.45}$$

is fulfilled in every matching point r_m. Here, $\Psi'(r) = d\Psi(r)/dr$. By substituting the ratio $\Psi_1'(r_m)/\Psi_1(r_m) = z$ and taking into account the expression (2.42) for $R_{WKB}(r_m)$ we obtain

$$R_{WKB}(r_m) = -\frac{z - \frac{i}{\hbar}p(r_m) + \frac{p'(r_m)}{2p(r_m)}}{z + \frac{i}{\hbar}p(r_m) + \frac{p'(r_m)}{2p(r_m)}}. \tag{2.46}$$

By solving numerically the Schrödinger equation and injecting the solution into Eq. (2.46) we calculate the reflection coefficient $|R_{WKB}|^2$ from the multitude of points inside the potential. Fig. 2.3 shows the dependence of $|R_{WKB}|^2$ on the matching point r_m. The reflection coefficient grows from zero outside the reflecting interval and approaches the well-defined constant value at very small r_m. At this distance the phase $\eta(r_m)$ is a real number and we take the constant value of $|R_{WKB}|^2$ at very small r_m as a final value of the reflection coefficient $|R|^2$.

2.3 Asymptotic behavior of quantum reflection

As we have seen in Sec. 2.1.1, reflection from a potential barrier is classically forbidden in the case of the total energy E exceeding the potential height V_B. This is also the case in the semi-classical picture, when the WKB-approximation is valid. The atom is reflected only at the classical turning point at the repulsive wall (see the Fig. 2.1 (b)).

In semi-classical as well as in quantum scattering theory the wave function of an atom far from the surface is represented by a sum of an incoming and an outgoing plane waves,

$$\Psi(r) = A(e^{ik_0 r} + Re^{-ik_0 r}). \tag{2.47}$$

Here, $k_0 = 2mE/\hbar^2$ is the incident wave number, A and R denote the wave function amplitude and the reflectivity from the repulsive wall, respectively. In the case of elastic scattering from a cold surface $|R| \simeq 1$.

In the WKB-approximation the quantum effect of above-barrier reflection is absolutely absent. This results from the fact that reflection is treated using perturbation theory, i.e. the phase of the wave function is expanded into a series of terms of rising order in λ_{dB}. However, the effect of the above-barrier reflection is of order $e^{-const_1/\lambda_{dB}^{const_2}}$. Here, $const_1 > 0$ and $0 < const_2 \leq 1$. Hence, the later effect is suppressed.

2.3.1 Above-barrier reflection

The first method for calculating above-barrier reflection was suggested by [Pokrovskii et al., 1958]. For simplicity, the Schrödinger equation is written in the dimensionless form (see App. A, Eq. (A.3))

$$\alpha^2 \frac{d^2\Psi(\xi)}{d\xi^2} + k^2(\xi)\Psi(\xi) = 0. \tag{2.48}$$

Here, $\alpha = \lambda_{dB}/(2\pi a)$ is the incident de Broglie wavelength λ_{dB} normalized to 2π and some coordinate a, $\xi = r/a$ denotes the dimensionless coordinate and $k(\xi) = \sqrt{1 - V(\xi)/E} = k(x)/k_0$ represents the local wave number, normalized to the incident wave number $k_0 = 2\pi/\lambda_{dB}$. The coordinate a can denote, for instance, the width of the potential barrier.

The incoming wave function in the dimensionless coordinate is given by (see App. A, Eq. (A.8))

$$\Psi(\xi) = \frac{1}{\sqrt{k(\xi)}} \exp\left(\frac{i}{\alpha}\int_{\xi_0}^{\xi} k(\xi)d\xi\right). \tag{2.49}$$

We want to transform the Schrödinger equation (2.48) to a form, which is convenient for using perturbation theory. After renaming $\int_{\xi_0}^{\xi} k(\xi)d\xi \stackrel{def}{=} \alpha t$ and $\exp(\frac{i}{\alpha}\int_{\xi_0}^{\xi} k(\xi)d\xi) \stackrel{def}{=} y(\xi)$ the semi-classical wave function Eq. (2.49) takes the form $\Psi(\xi) = y(\xi)/\sqrt{k(\xi)}$. By substituting this expression into Eq. (2.48) we obtain the desired equation for the function $y(t)$,

$$\frac{d^2y(t)}{dt^2} + \left(1 + \alpha^2 q(\alpha t)\right) y(t) = 0. \tag{2.50}$$

In this equation the term $\alpha^2 q(\alpha t) = \alpha^2\hbar^2 p^{-3/2}(\xi)\, d^2p^{-1/2}(\xi)/d\xi^2 = \alpha^2 B(\xi)$ represents the perturbation. $B(\xi)$ is the badlands function B_2, obtained in Sec. 2.1.2. In the semi-classical representation $\alpha \ll 1$ and in the WKB-approximation $|B(\xi)| \ll 1$. In this case the term $|\alpha^2 q(\alpha t)| \ll 1$.

In perturbation theory Eq. (2.50) is represented by

$$\left(\widehat{H}_0 - \widehat{V}\right) y(t) = 1 \cdot y(t). \tag{2.51}$$

Here, $\widehat{H}_0 = -d^2/dt^2$ is the unperturbed Hamiltonian with eigenvalue $E = 1$ and $\widehat{V} = \alpha^2 q$ is the perturbation term. We want to calculate the transition amplitude from the state described by the incoming wave function in Eq. (2.49) to the state described by the outgoing one. Since both states have the same energy, we apply perturbation theory for the continuous spectrum [Landau and Lifschitz, 1985]. In our presentation of the perturbed Schrödinger equation (2.50) through the function $y(t)$ the initial state is described by $y(t) = \exp(it)$ and the final state by $y(t) = \exp(-it)$. The transition from the initial to the final state occurs through a multitude of states, each of which is described by a function of the type $y(t) = C_1 \exp(ikt) + C_2 \exp(-ikt)$. Here, k denotes the dimensionless wave number, corresponding to the state with energy k^2.

In the zero-order approximation the unperturbed equation for each state from the continuous spectrum has to be solved,

$$\widehat{H}_0 y_k^{(0)}(t) = k^2 y_k^{(0)}(t). \tag{2.52}$$

The solution of this equation is $y_k^{(0)}(t) = C_1 \exp(ikt) + C_2 \exp(-ikt)$, which corresponds to the expected function. For the initial state we have $k = 1$, $C_1 = 1$, $C_2 = 0$ and for the final state one finds $k = -1$, $C_1 = 0$ and $C_2 = 1$. The energies of both states $E^{(0)} = k^2 = 1$ are equal.

The amplitude of the transition from the state with $k = 1$ to the state with $k = -1$ is given by the perturbation expression [Pokrovskii et al., 1958]

$$R = \frac{1}{2i}\left[V_{-1,1} + \frac{1}{2\pi}\int \frac{V_{-1,k}V_{k,1}}{1-k^2}dk + \frac{1}{(2\pi)^2}\int\int \frac{V_{-1,k_1}V_{k_1,k_2}V_{k_2,1}}{(1-k_1^2)(1-k_2^2)}dk_1 dk_2 + \dots\right]. \tag{2.53}$$

Here, k_i corresponds to the i-th state with energy k_i^2 and V_{k_j,k_i} stands for the matrix element of the perturbation V. All terms in equation (2.53) are of the same order in α. The matrix element V_{k_j,k_i} is given as

$$V_{k_j,k_i} = -\langle y_{k_j}^{(0)} | \widehat{V} y_{k_i}^{(0)} \rangle = -\alpha^2 \int_{-\infty}^{\infty} e^{i(k_i - k_j)t} q(\alpha t) dt. \tag{2.54}$$

The minus sign in this expression takes into account the minus sign in front of V in Eq. (2.51).

We introduce the new variable $\tau = \alpha t = \int_{\xi_0}^{\xi} k(\xi) d\xi$. Then, expression (2.54) takes the form

$$V_{k_j,k_i} = -\alpha \int_{-\infty}^{\infty} e^{\frac{i}{\alpha}(k_i - k_j)\tau} q(\tau) d\tau. \tag{2.55}$$

To give a non-negligible contribution of V_{k_j,k_i} in Eq. (2.53), the function $q(\tau)$ must have singularities in the complex plane. It can be calculated, that the

roots and singularities of the function $k^2(\xi)$ lead to such singularities of q. However, it is necessary to note, that poles of $k^2(\xi)$ of order ≥ 2 do not result in singularities of q.

In [Pokrovskii et al., 1958] the leading term of the transition amplitude (2.53) is calculated as

$$R = -ie^{\frac{2i}{\alpha}\tau_0} = -ie^{\frac{2i}{\alpha}\int_{\xi_0}^{\xi_s} k(\xi)d\xi}. \tag{2.56}$$

Here, $\tau_0 = \int_{\xi_0}^{\xi_s} k(\xi)d\xi$ and ξ_s denote the root or the pole of the function $k^2(\xi)$, leading to the singularity of q. This transition amplitude is of course nothing else than the reflection amplitude which appears if the initial kinetic energy exceeds the potential barrier height.

There are two conditions for the validity of the expression (2.56):

- The first one is [Pokrovskii et al., 1958]

$$|V_{k_j,k_i}| \leq \alpha \int_{-\infty}^{+\infty} |q(\tau)|d\tau = M\alpha, \tag{2.57}$$

  where M is of order unity. However, if $|k_j - k_i| \leq \alpha$ then expression (2.55) for V_{k_j,k_i} is not correct anymore and expression (2.56) is not valid.

- Secondly, Eq. (2.56) is calculated for the assumption that τ_0 gives the leading contribution to the effect. The contribution of the complex conjugate of τ_0 must be negligible. This means that all singular poles of $q(\tau)$ must not be situated too close to each other. This can be written as

$$\Delta \stackrel{def}{=} |\tau_0 - \tau_0^*| \gg \alpha. \tag{2.58}$$

  Here, τ_0^* denotes the complex conjugate of τ.

2.3.2 High-energy asymptotic behavior of reflection from a homogeneous potential

It is very interesting that a barrier can be created not only by a repulsive potential, but by an attractive one, too. A barrier is defined by its property of preventing motion of a wave packet which leads to partial reflection. An attractive long-range potential between a slow neutral atom with mass m and a surface (or another atom) represents a barrier under certain conditions. Since the incident kinetic energy of the atom is always positive, only above-barrier reflection can appear from the atom-surface interaction potential.

The wave function of the atom is partially reflected in the vicinity of the virtual turning point, which is a root of the function $k^2(r)$.

In this section we calculate the asymptotic behavior of the above-barrier reflectivity for a neutral atom scattering from a surface, using the theory presented in the previous section. Moreover, we specify the range of energies of the incident atom, in which the formula for the reflectivity is valid. The reflection coefficient from a homogeneous potential ($\propto r^{-n}$) is calculated. Since generally the interaction potential is non-homogeneous, the formula can be used only in limited cases, as discussed in the next section.

The above-barrier quantum reflectivity is given as

$$R = -i \exp\left[\frac{2i}{\hbar}\int_{r_s}^{r_t} p(r)dr\right], \tag{2.59}$$

where $p(r) = \hbar k(r)$ denotes the local momentum of the atom, r_s is a real starting point of the atom motion lying far from the barrier and r_t represents a virtual turning point being a root of the function $p(r)$, $p(r_t) = 0$.

Firstly, we want to know where the virtual turning point lies inside the interaction potential. The long-range homogeneous attractive potential of the atom-surface (or atom-atom) interaction is given without the retardation effect as

$$V(r) = -\frac{C_n}{r^n} = -\frac{\hbar^2}{2m}\cdot\frac{\beta_n^{n-2}}{r^n}. \tag{2.60}$$

Here, n denotes the potential power and is equal to 3 for atom-surface interaction or to 6 for atom-atom interaction. The latter representation of the potential in terms of the parameter β_n is very useful for the further calculations. β_n has the dimensionality of a length.

The local momentum of the atom is defined as $p(r) = \sqrt{2m\,(E - V(r))}$. Taking into account the expression (2.60) we obtain

$$p(r) = \sqrt{2mE}\sqrt{1 + \frac{\hbar^2}{2mE}\cdot\frac{\beta_n^{n-2}}{r^n}}. \tag{2.61}$$

The function $p(r)$ in Eq. (2.61) has a root r_t if $1+(\hbar^2/(2mE))\cdot(\beta_n^{n-2}/r_t^n) = 0$. Then, this root, which is a virtual turning point, is given by

$$r_t^n = -\frac{\hbar^2}{2mE}\beta_n^{n-2}. \tag{2.62}$$

We recall the definition of the distance r_0, at which the magnitudes of the incident kinetic energy E and of the local potential energy $|V(r_0)|$ are equal, $E = |V(r_0)| = |\hbar^2\beta_n^{n-2}r_0^{-n}/(2m)|$ (see the Fig. 2.2),

$$r_0 = \left(\frac{\hbar^2}{2mE}\beta_n^{n-2}\right)^{\frac{1}{n}} = \left(\frac{\beta_n^{n-2}}{k_0^2}\right)^{\frac{1}{n}}. \tag{2.63}$$

By comparing this expression with Eq. (2.62) we can rewrite r_t in terms of r_0,

$$r_t = (-1)^{\frac{1}{n}} r_0. \tag{2.64}$$

What can we learn from the obtained equation (2.64)? Firstly, it is clear that not a single but n complex virtual turning points exist. Secondly, the module of r_t is equal to r_0. In general, the proportionality of r_t to $r_0(E)$ shows that the reflection occurs at different distances from the surface depending on the incident energy E. For vanishing E, r_0 increases and the wave is reflected far from the surface. On the other hand, if the energy E is relatively high, r_0 can move too close to the repulsive wall for above-barrier reflection to be possible.

From n complex roots of $p(r)$ we choose the one with the smallest positive imaginary part. This turning point lies in the first quadrant of the complex plane and can be written as $r_t = (\cos\frac{\pi}{n} + i\sin\frac{\pi}{n}) \cdot r_0$.

The integral in the exponent in the expression for the reflectivity (2.59)

$$I_n = \int_{r_s}^{r_t} p(r)dr = \int_{r_s}^{r_t} \sqrt{2m\left(E + \frac{\hbar^2}{2m} \cdot \frac{\beta_n^{n-2}}{r^n}\right)} dr \tag{2.65}$$

is calculated in App. B, Eq. (B.2),

$$I_n = \hbar k_0 r_0 (\cos\frac{\pi}{n} \cdot I_{1n} + i\sin\frac{\pi}{n} \cdot I_{2n}). \tag{2.66}$$

Here, real I_{1n} and complex I_{2n} are defined by

$$I_{1n} = \int_{+\infty}^{1} \sqrt{1 + \frac{1}{\xi_1^n \cos^n\frac{\pi}{n}}} d\xi_1, \tag{2.67}$$

$$I_{2n} = \int_{0}^{1} \sqrt{1 + \frac{1}{(\cos\frac{\pi}{n} + i\xi_2 \sin\frac{\pi}{n})^n}} d\xi_2. \tag{2.68}$$

Expression (2.59) is then found to be

$$R = -i\exp\left(2k_0 r_0 (\cos\frac{\pi}{n} \cdot I_{1n} - \sin\frac{\pi}{n} \cdot \Im I_{2n} + i\Re I_{2n})\right). \tag{2.69}$$

Since we are only interested in the real contribution, the final expression for the asymptotic quantum reflectivity is given by the module of R,

$$|R| = e^{-2k_0 r_0 \sin\frac{\pi}{n} \Re I_{2n}} \stackrel{def}{=} e^{-k_0 r_0 B_n}, \tag{2.70}$$

where $B_n = 2\sin\frac{\pi}{n} \cdot \Re\{\int_0^1 \sqrt{1 + (\cos\frac{\pi}{n} + i\xi_2 \sin\frac{\pi}{n})^{-n}} d\xi_2\}$. The values of the parameter B_n for different n are listed in Table 2.3.

n	3	4	5	6	7
B_n	2.24050	1.69443	1.35149	1.12025	0.954997

Table 2.3: The coefficient B_n for the different potential power n.

Thus, the asymptotic behavior of the reflection coefficient, $|R|^2$, which is equal to the reflection probability, is

$$\boxed{|R|^2 = e^{-2B_n k_0 r_0}.} \tag{2.71}$$

Since $r_0 = \beta_n^{1-\frac{2}{n}} k_0^{-2/n}$, the expression $k_0 r_0$ in the terms of the potential length parameter β_n is given as $k_0 r_0 = (k_0\beta_n)^{1-\frac{2}{n}}$, resulting in

$$\boxed{|R|^2 = e^{-2B_n (k_0\beta_n)^{1-\frac{2}{n}}}.} \tag{2.72}$$

The final form of the reflectivity $|R|$ was firstly obtained in [Friedrich et al., 2002]. There, the validity range for this formula is given as

$$\boxed{k_0\beta_n \gg 1,} \tag{2.73}$$

which implies the fact, that the incident energy E is relatively high. Moreover, it allows to separate well this high-energy asymptotic behavior from a different one, valid at very low energies, $k_0\beta_n \ll 1$. The latter approximation will be discussed in Section 2.3.4.

The more accurate validity range than the one given by Eq. (2.73) we can calculate, taking into consideration the accuracy condition for the above-barrier reflection theory. This condition includes the approximation, that all singularities of the badlands function must be well separated from each other. It has the following mathematical form

$$\frac{1}{\hbar}\int_{r_t^*}^{r_t} p(r) \gg k_0^{-1}. \tag{2.74}$$

From this expression one derives (see Eq. (B.8) in App. B)

$$k_0\beta_n \gg (\sin\frac{\pi}{n}\cdot|I_{3n}|)^{\frac{n}{2-n}} \stackrel{def}{=} G_n, \tag{2.75}$$

n	3	4	5	6	7
G_n	0.08891	0.34830	0.60531	0.84339	1.06659

Table 2.4: The validity range parameter G_n in dependence on the potential power n.

where I_{3n} is equal to

$$I_{3n} = \int_{-1}^{1} \sqrt{1 + \frac{1}{(\cos\frac{\pi}{n} + i\xi_2 \sin\frac{\pi}{n})^n}} d\xi_2. \tag{2.76}$$

We define the right hand side of the inequality (2.75) as a dimensionless constant G_n, which is given in Table 2.4 for different n. From the expression (2.75) it can be calculated that the asymptotic formula (2.72) is valid at large incident energies

$$\boxed{E \gg \frac{\hbar^2}{2m\beta_n^2} G_n^2 = \left(\frac{\hbar^2 G_n}{2m}\right)^2 \frac{1}{C_n^{\frac{2}{n-2}}}.} \tag{2.77}$$

2.3.3 High-energy asymptotic behavior of reflection from a non-homogeneous potential

In the previous section we have studied the high-energy behavior of the reflection coefficient Eq. (2.72) at quantum scattering from the homogeneous attractive potential Eq. (2.60). The validity range of this asymptote is given by Eq. (2.75) and depends on the shape and the magnitude of the potential. In reality, the long-range attractive potential is non-homogeneous due to the effect of retardation. This effect will be discussed in detail in Chapter 3. While playing no significant role in classical scattering, retardation is very important in quantum reflection. The retarded potential is well described by

$$V(r) = -\frac{C_n}{r^{n-1}(r+l)} = -\frac{\hbar^2}{2m} \cdot \frac{\beta_n^{n-2}}{r^{n-1}(r+l)} \tag{2.78}$$

with the asymptotic tails

$$V(r) = \begin{cases} -\frac{C_{n-1}}{r^{n-1}} = -\frac{\hbar^2}{2m} \cdot \frac{\beta_{n-1}^{n-3}}{r^{n-1}} & \text{at } a < r_0 \ll l, \\ -\frac{C_n}{r^n} = -\frac{\hbar^2}{2m} \cdot \frac{\beta_n^{n-2}}{r^n} & \text{at } r_0 \gg l. \end{cases} \tag{2.79}$$

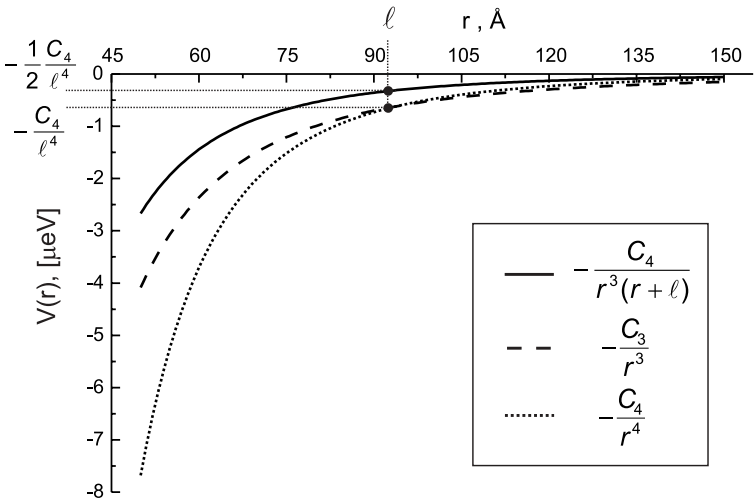

Figure 2.4: Solid line: Attractive atom-surface interaction potential including retardation for the ^{3}He-Au(111) system with $l = 93\,\text{Å}$ and $C_4 = 48\,\text{eVÅ}^4$. Dashed line: The non-retarded van der Waals potential approximates the interaction potential for $r \ll l$. Dotted line: The purely retarded Casimir potential, which the interaction potential tends to at $r \gg l$. At the distance l the value of the interaction potential amounts to half of the values of the asymptotic potential tails, which are equal at this distance.

The potential in Eq. (2.78) for the atom-atom or atom-surface interaction is called Casimir-van der Waals potential. The transition length l separates these two homogeneous parts and is defined as the distance from the surface, at which the values of both parts in Eq. (2.79) are equal, $-C_{n-1}/l^{n-1} = -C_n/l^n \stackrel{def}{=} -\hbar^2 K_0^2/(2m)$. One obtains

$$l = \frac{C_n}{C_{n-1}} = \frac{\beta_n^{n-2}}{\beta_{n-1}^{n-3}}. \tag{2.80}$$

The magnitude of the retarded non-homogeneous potential in Eq. (2.78) at the distance l is only half of the value of the asymptotic tails in Eq. (2.79) at this distance, as it is sketched in Fig. 2.4. The inequality $a < r_0$ in the first expression of Eq. (2.79) qualitatively illustrates the boundary for r_0. Close to the potential minimum position a the influence of the short-range forces can become significant. In this range the interaction potential becomes flatter than r^{-2} and no quantum reflection is expected.

The very important dimensionless parameter ρ is introduced by [Friedrich et al., 2002]

$$\boxed{\rho \stackrel{def}{=} K_0 l = \sqrt{\frac{2m}{\hbar^2} \cdot \frac{C_n}{C_{n-1}}} = \left(\frac{\beta_{n-1}}{\beta_n}\right)^{\frac{(n-2)(n-3)}{2}} = \left(\frac{\beta_{n-1}}{l}\right)^{\frac{n-3}{2}}.} \tag{2.81}$$

This parameter describes the interacting system in general because of its dependence on all parameters of the potential and the mass of the incident atom. We will see, that its value influences dramatically the reflection behavior not only in the high-energy limit, but also in the limit of very small energies.

Unfortunately, an analytic form for the reflection coefficient in the case of the potential Eq. (2.78) in analogy to Eq. (2.72) cannot be found. It is only possible to make some approximations. From the vicinity of the point r_0 the largest contribution to the reflected wave occurs. If r_0 lies much closer to the surface than the transition distance l, $a < r_0 \ll l$, the local potential in the vicinity of r_0 is very weakly retarded, $V(r) \approx -C_{n-1}/r^{n-1}$. Thus, the high-energy reflection coefficient can be described by formula (2.72),

$$\boxed{|R_{n-1}|^2 = e^{-2B_{n-1}(k_0\beta_{n-1})^{1-\frac{2}{n-1}}} \quad \text{at } a < r_0 \ll l.} \tag{2.82}$$

However, if $r_0 \gg l$ the purely retarded tail $V(r) = -C_n/r^n$ dominates in the vicinity of r_0 and the reflection coeffecient can be written as

$$\boxed{|R_n|^2 = e^{-2B_n(k_0\beta_n)^{1-\frac{2}{n}}} \quad \text{at } r_0 \gg l.} \tag{2.83}$$

Now we take into account, that r_0 is a point of equal incident kinetic and local potential energies, i.e. $r_0 = \beta_i(k_0\beta_i)^{-2/i}$. Here, $i = (n-1)$ or n depending on which tail of Eq. (2.79) is dominant. The validity ranges of the equations (2.82) and (2.83) are transformed to

$$a < r_0 \ll l \quad \rightarrow \quad \left(\frac{\beta_{n-1}}{a}\right)^{\frac{n-1}{2}} > k_0\beta_{n-1} \gg \rho^{\frac{n-1}{n-3}}, \tag{2.84}$$

$$r_0 \gg l \quad \rightarrow \quad k_0\beta_n \ll \rho^{\frac{n}{n-2}}, \tag{2.85}$$

respectively. Since the high-energy asymptote, given by the analytic form of Eq. (2.72) has its general validity range given by Ineq. (2.75), the inequality (2.85) has the complete form

$$G_n \ll k_0\beta_n \ll \rho^{\frac{n}{n-2}}. \tag{2.86}$$

In terms of the incident wave number (or the incident energy) the validity ranges for $|R_{n-1}|^2$ and $|R_n|^2$ are given by

$$|R_{n-1}|^2: \quad \sqrt{\frac{\beta_{n-1}^{n-3}}{a^{n-1}}} > k_0 \gg \frac{\rho^{\frac{n-1}{n-3}}}{\beta_{n-1}}, \tag{2.87}$$

$$|R_n|^2: \quad \frac{G_n}{\beta_n} \ll k_0 \ll \frac{\rho^{\frac{n}{n-2}}}{\beta_n}. \tag{2.88}$$

It is clear, that the energy ranges of both asymptotes have to be separated by the same value of k_0, i.e. $\rho^{(n-1)/(n-3)}/\beta_{n-1}$ has to be equal to $\rho^{n/(n-2)}/\beta_n$. Using formula (2.81) we obtain $\beta_{n-1} = \beta_n \cdot \rho^{2/(n-2)/(n-3)}$ and in fact $\rho^{(n-1)/(n-3)}/\beta_{n-1} = \rho^{n/(n-2)}/\beta_n$. The intersection point of both asymptotes at $k_0 = \rho^{(n-1)/(n-3)}/\beta_{n-1}$ moves in the direction of lower energies by decreasing the parameter ρ. Thus, at a very large value of ρ it is very difficult if not impossible to observe the asymptote $|R_{n-1}|^2$. If the value of ρ is not much larger than $G_n^{(n-2)/n}$, it is impossible to measure the asymptote $|R_n|^2$. In this case the probability to observe $|R_{n-1}|^2$ increases.

Since ρ is proportional to the square of the atom mass, the choice of the incident atom plays a decisive role in the behavior of the reflection coefficient far from threshold $E \to 0$ (in the high-energy limit). We will see in Chapter 4, that scattering of light ^{3}He atoms from a dielectric surface (weak retardation effect) opens up the possibility for measuring the asymptote $|R_{n-1}|^2$ ($n = 4$).

The value of the reflection coefficient in the intersection point of both asymptotes $|R_{n-1}|^2$ and $|R_n|^2$ is equal to $\exp(-2B_n\rho)$. It follows that as ρ grows larger the reflection coefficient becomes smaller and therefore more and more difficult to measure.

It is useful to plot the asymptotes Eq. (2.82) and Eq. (2.83) on a $\ln(-\ln)$-scale, since the reflection coefficient takes the form of a straight line with respect to $\ln k_0$,

$$\begin{aligned} &\ln(-\ln|R_{n-1}|^2) = \ln(2B_{n-1}\beta_{n-1}^{1-\frac{2}{n-1}}) + (1-\tfrac{2}{n-1})\ln k_0 \\ &\text{at } \tfrac{1}{2}\ln\left(\tfrac{\beta_{n-1}^{n-3}}{a^{n-1}}\right) > \ln k_0 \gg \ln\left(\tfrac{\rho^{\frac{n-1}{n-3}}}{\beta_{n-1}}\right), \end{aligned} \tag{2.89}$$

$$\begin{aligned} &\ln(-\ln|R_n|^2) = \ln(2B_n\beta_n^{1-\frac{2}{n}}) + (1-\tfrac{2}{n})\ln k_0 \\ &\text{at } \ln\left(\tfrac{G_n}{\beta_n}\right) \ll \ln k_0 \ll \ln\left(\tfrac{\rho^{\frac{n-1}{n-3}}}{\beta_{n-1}}\right). \end{aligned} \tag{2.90}$$

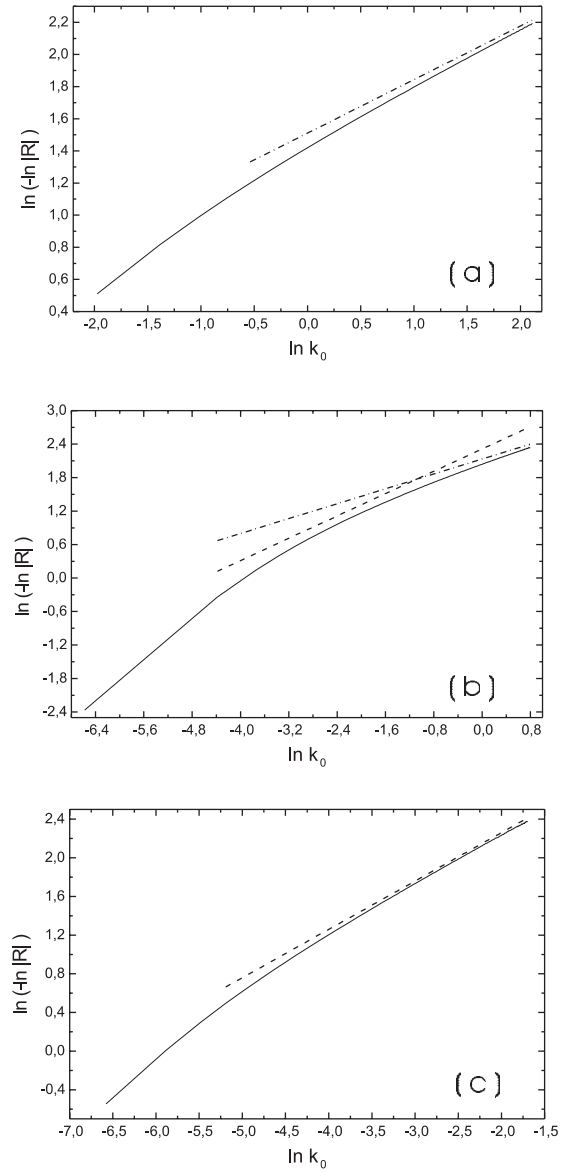

Figure 2.5: Reflectivity $|R|$ on the $\ln(-\ln)$-scale versus $\ln k_0$ at (a) $\rho = 0.59$, (b) $\rho = 3.0$ and (c) $\rho = 10.0$. The dot-dashed and dashed straight lines with slopes 1/3 and 1/2 represent the analytic reflectivities, the squares of which are given by Eq. (2.82) and Eq. (2.83), respectively. The solid curve shows the numerically simulated reflectivity from the Casimir-van der Waals potential. Increasing the incident atom energy E corresponds to increasing $\ln k_0$ and larger values of $\ln(-\ln|R|)$ correspond to smaller values of $|R|$.

The slopes of the straight lines, $(1-2/i)$ with $i=n$ or $(n-1)$, depend only on the power i of the potential. The intersection of these straight lines with the ordinate axis are equal to the first terms in the equations (2.89) and (2.90) and depend not only on the potential power, but also on the potential strength. By measuring the reflection coefficient in the high-energy limit it is possible to extract information about the attractive potential directly from these analytical expressions. From the slope of the straight line on a $\ln(-\ln)$-scale the potential power n is determined. By placing this n in the term of the intersection with the ordinate axis $\ln(2B_n\beta_n^{1-2/n})$, the potential length parameter β_n (and therewith the potential strength C_n) can be obtained.

Fig. 2.5 depicts three cases for the reflectivity, $|R|^2$, at different values of the parameter ρ. On the $\ln(-\ln)$-scale, it is possible to observe the asymptotes $|R_n|$ and $|R_{n-1}|$ in the form of straight lines. The potential power n is equal to 4, which is equivalent to scattering of an atom from a surface. The dot-dashed and dashed lines with the slopes 1/3 and 1/2 in the figure represent the $|R_3|$ and $|R_4|$ asymptote, respectively. The solid curve shows the non-analytical reflection coefficient from the non-homogeneous Casimir-van der Waals potential $V(r)=-(\hbar^2/(2m))\cdot(\beta_4^2 r^{-3}/(r+l))$, obtained using a numerical simulation, which will be described in the next section. The (a), (b) and (c) parts in the figure correspond to the values of $\rho=\sqrt{G_4}$=0.59, 3 and 10, respectively. One clearly sees that at small $\rho=0.59$ the reflectivity approaches the asymptote $|R_3|$ (Fig. 2.5 (a)) and the asymptote $|R_4|$ does not exist. At the large value $\rho=10$, the asymptote $|R_4|$ is well observable (Fig. 2.5 (c)) and $|R_3|$ is situated at much higher incident energies and is therefore omitted here. At $\rho=3$ the reflectivity approaches the $|R_3|$-asymptote, but the asymptote $|R_4|$ below the intersection point dominates. The picture shows also that the value of the reflectivity differs strongly depending on the magnitude of ρ. At the same incident energy, given by $\ln k_0=0$, $\ln(-\ln|R|)$ is approximately equal to 1.4, 2.0 and >2.4 (i.e $|R|\approx 1.7\ 10^{-2}$, $0.6\ 10^{-3}$ and $>1.6\ 10^{-5}$) at $\rho=0.59$, 3 and 10, respectively. It is necessary to note, that the larger value of the $\ln(-\ln|R|)$ corresponds to the smaller value of $|R|$.

2.3.4 Low-energy asymptote

For an atom, falling onto the surface of a solid it is possible to calculate analytically the behavior of the reflection coefficient at very low incident energies. The interaction potential between this atom and the surface is given by a non-homogeneous long-range attractive potential (see Eq. (2.78)). As we have seen in Section 2.2, the value of the reflectivity from the badland is well defined at very small matching distance r_m, which is situated inside the WKB-region. The wave function in this region at $r<r_m$ is given by

the semi-classical expression (2.42). By writing the reflectivity $R_{WKB}(r_m)$ through the phase ϕ_m, which the atom picks up when going through the badland up to the distance r_m,

$$R_{WKB} = \exp(-i\phi_m), \tag{2.91}$$

we obtain the amplitude-phase description of the expression (2.42)

$$\Psi_{WKB}(r) = \frac{A}{\sqrt{p(r)}} \cos\left(\frac{1}{\hbar}\int_{r_m}^{r} p(r)dr - \frac{\phi_m}{2}\right). \tag{2.92}$$

At very small incident energy the wave function in the same WKB-region can be represented as a linear combination of two independent solutions of the Schrödinger equation at zero incident energy $E = 0$, Ψ_0 and Ψ_1,

$$\Psi(r) = \Psi_0(r) + ik_0\Psi_1(r). \tag{2.93}$$

At $r \to -\infty$ this wave function has to take the form of an outgoing free wave function $e^{ik_0 r}$. Thus, the boundary conditions for Ψ_0 and Ψ_1 at $r \to -\infty$ are

$$\Psi_0(r \to -\infty) \propto \cos(k_0 r) \overset{k_0\to 0}{\propto} 1, \tag{2.94}$$

$$\Psi_1(r \to -\infty) \propto \sin(k_0 r) \overset{k_0\to 0}{\propto} k_0 r. \tag{2.95}$$

The zero-energy wave functions inside the WKB-region satisfies the expression (2.92), with $p(r) = p_0(r)$ denoting the local momentum at zero incident energy, $A = D_{0,1}$ and $\phi_m = \phi_{0,1}$. At $k_0 \to 0$ the absolute value of the wave function in Eq. (2.93) is expanded

$$\begin{aligned}
\Psi(r) &= \frac{D_0}{\sqrt{p_0(r)}}\left[\cos\left(x - \frac{\phi_2}{2}\right) + i\frac{D_1}{D_0}k_0 \cos\left(x - \frac{\phi_1}{2}\right)\right] \\
&\propto \cos\left(x - \frac{\phi_0}{2}\right)\left[1 + i\frac{D_1}{D_0}k_0 \cos\left(\frac{\phi_0 - \phi_1}{2}\right)\right] - \\
&\quad i\frac{D_1}{D_0}k_0 \sin\left(\frac{\phi_0 - \phi_1}{2}\right)\sin\left(x - \frac{\phi_0}{2}\right) \\
&\overset{k_0\to 0}{\approx} \cos\left(x - \frac{\phi_0}{2}\right) - ik_0 b \sin\left(x - \frac{\phi_0}{2}\right) \\
&\overset{k_0\to 0}{\approx} \cos\left(x - \frac{\phi_0}{2}\right)\cos(ik_0 b) - \sin\left(x - \frac{\phi_0}{2}\right)\sin(ik_0 b) \\
&= \cos\left(x - \frac{\phi_0 - 2ik_0 b}{2}\right),
\end{aligned} \tag{2.96}$$

where $x = \hbar^{-1} \int_{r_m}^{r} p_0(r)dr$ and

$$b \stackrel{def}{=} \frac{D_1}{D_0} \sin\left(\frac{\phi_0 - \phi_1}{2}\right) \tag{2.97}$$

is a length parameter [Eltschka et al., 2000].

By comparing this expression with Eq. (2.92) the reflectivity in Eq. (2.91) can be calculated. The phase ϕ_m is given by $\phi_m = \phi_0 - 2ik_0 b$ and the reflectivity is given by

$$R_{WKB} = \exp(-i\phi_0 - 2k_0 b). \tag{2.98}$$

The reflection coefficient $|R_{WKB}|^2$ is equal to

$$|R_{WKB}|^2 = \exp(-4k_0 b) \stackrel{k_0 \to 0}{\approx} 1 - 4k_0 b. \tag{2.99}$$

Fortunately, the amplitudes and phases of the zero-energy wave functions in the non-homogeneous potential (2.78) with the retarded potential power $n = 4$ (the atom-surface interaction) can be obtained exactly. In this case the Schrödinger equation for the wave function in the attractive atom-surface potential at zero incident energy

$$\Psi_0''(r) + \frac{\beta_3 l}{r^3(r+l)}\Psi_0(r) = 0 \tag{2.100}$$

can be rewritten in the form

$$r^n \Psi_0''(r) + c(ar+b)^{n-4}\Psi_0(r) = 0 \tag{2.101}$$

with $n = 3$, $c = \beta_3 l$, $a = 1$ and $b = l$. By transforming the coordinate r to $\xi = r/(r+l)$ and the wave function $\Psi_0(r)$ to $w = \Psi_0(r)/(r+l)$ this equation takes the form of the Bessel equation [Polyanin and Zaitsev, 1996]

$$w''(\xi) + \gamma\xi^{-3}w(\xi) = 0. \tag{2.102}$$

Here, $\gamma = cb^{-2} = \beta_3/l$. This equation has the well-known solution

$$w(\xi) = \sqrt{\xi}\left[const_1 \cdot J_{\frac{1}{n-2}}\left(\frac{2\sqrt{\gamma}}{n-2}\xi^{\frac{2-n}{2}}\right) + const_2 \cdot N_{\frac{1}{n-2}}\left(\frac{2\sqrt{\gamma}}{n-2}\xi^{\frac{2-n}{2}}\right)\right] \tag{2.103}$$

with $n = 3$. $J_\nu(z)$ and $N_\nu(z)$ are the ν-order Bessel and Neumann[1] functions (the Bessel functions of the first and second kind), respectively. Going back

[1] This function is usually called Neumann function $N_\nu(z)$ by physicists whereas in mathematical books it is denoted as $Y_\nu(z)$

to the coordinate r and the wave function Ψ_0, we obtain two independent zero-energy wave functions,

$$\Psi_{0,1}(r) = \sqrt{r(r+l)}\,[A_{0,1}J_1(z) + B_{0,1}N_1(z)]\,, \tag{2.104}$$

satisfying the boundary conditions Eq. (2.94) and Eq. (2.95). Here, $z = 2\sqrt{\beta_3/r + \beta_3/l}$ and the constants $A_{0,1}$ and $B_{0,1}$ are given by

$$\begin{aligned} A_0 &= -\frac{\pi}{l}N_1(2\rho), \\ B_0 &= -\frac{\pi}{l}J_1(2\rho), \\ A_1 &= \pi(\rho N_1'(2\rho) + \frac{1}{2}N_1(2\rho)), \\ B_1 &= -\pi(\rho N_1'(2\rho) + \frac{1}{2}N_1(2\rho)). \end{aligned} \tag{2.105}$$

The dimensionless parameter ρ is defined by Eq. (2.81). At the matching point $r_m \ll \beta_3$ the large-argument asymptotes for the Bessel functions

$$\begin{aligned} J_\nu(z) &\approx \sqrt{\frac{2}{\pi z}}\cos\left(z - \frac{1}{2}\nu\pi - \frac{1}{4}\pi\right), \\ N_\nu(z) &\approx \sqrt{\frac{2}{\pi z}}\sin\left(z - \frac{1}{2}\nu\pi - \frac{1}{4}\pi\right) \end{aligned} \tag{2.106}$$

can be applied. In this case the amplitudes and phases of the wave functions $\Psi_0(r)$ and $\Psi_1(r)$ are calculated to [Friedrich et al., 2002]

$$D_{0,1} = \sqrt{\hbar l}\sqrt{A_{0,1}^2 + B_{0,1}^2}, \tag{2.107}$$

$$\phi_{0,1} = \frac{3}{2}\pi - 4\rho + 2\arctan\frac{B_{0,1}}{A_{0,1}}. \tag{2.108}$$

By taking into account the expression (2.97) for the length paramater b we obtain

$$\begin{aligned} b &= \rho l \cdot \frac{J_1(2\rho)N_1'(2\rho) - N_1(2\rho)J_1'(2\rho)}{J_1^2(2\rho) + N_1^2(2\rho)} \\ &= \frac{l/\pi}{J_1^2(2\rho) + N_1^2(2\rho)}. \end{aligned} \tag{2.109}$$

Here we have simplified calculations using [Abramovitz and Stegun, 1984]

$$J_\nu(z)N_\nu'(z) - N_\nu(z)J_\nu'(z) = W\{J_\nu(z), N_\nu(z)\} = \frac{2}{\pi z}. \tag{2.110}$$

The Wronskian $W\{J_\nu(z), N_\nu(z)\}$ is defined as the determinant of the matrix $\begin{pmatrix} J_\nu(z) & N_\nu(z) \\ J'_\nu(z) & N'_\nu(z) \end{pmatrix}$.

At $\rho \to \infty$, the sum $J_1^2(2\rho) + Y_1^2(2\rho) \to (\pi\rho)^{-1}$ and the length parameter $b \to \beta_4$. At $\rho \to 0$, we have $J_1^2(2\rho) + Y_1^2(2\rho) \to (\pi\rho)^{-2}$ and $b \to \pi\beta_3$.

At very small r_m, the reflectivity $|R_{WKB}| = |R|$ (see Section 2.2) and the experimentally observed reflection coefficient has the form

$$\boxed{|R|^2 = e^{-4bk_0} \overset{k_0 \to 0}{\approx} 1 - 4k_0 b.} \tag{2.111}$$

The validity range of this formula is approximatelly given by

$$\boxed{k_0 b \ll 1.} \tag{2.112}$$

On a $\ln(-\ln)$-scale the low-energy asymptote, Eq. (2.111), is written as

$$\ln(-\ln|R|^2) = \ln(4b) + \ln k_0 \qquad \text{at } \ln k_0 \ll -\ln b. \tag{2.113}$$

The function $\ln(-\ln|R|^2)$ of $\ln k_0$ is a straight line with unity slope and its intersection with the ordinate axis is $\ln(4b)$. By measuring this asymptotic behavior of the reflection coefficient at very low incident energies only parameter b can be obtained. Since b depends on the parameter ρ no information about potential strengths C_3 and C_4 can be extracted, as long as ρ is unknown.

In the experiment by [Shimizu and Fujita, 2002], a set of surfaces was studied. The surfaces of the same material (silicon) differed from each other by different surface atom density. The strengths of the van der Waals potential C_3 and therefore the parameters ρ were different for these surfaces. From the set of experiments by measuring of the reflection coefficient for each surface the function $b(\rho)$ can be obtained. The analysis of the results is presented in Section 4.4.

2.4 Sticking process

In the 30-ties of the 20th century Lennard-Jones and Devonshire predicted, that the interaction of a cold atom with a surface of a liquid or a solid differs significantly from the classical system [Lennard-Jones and Devonshire, 1936].

In classical mechanics the atom comes close to the surface and at a distance of some Å interacts with surface atoms through short-range forces. The atom couples to the surface by exciting surface phonons (lattice oscillations). The excitation propagates in the direction of the given momentum from the impact region of the atom onto the surface further through the coupling between the atoms in the lattice. If the incident energy of the impinging atom is comparable to the energy transferred to the lattice the atom adsorbs to the surface, because it has not enough kinetic energy to leave the field of attraction.

The process of the adsorption of the atom is called sticking onto the surface. In the classical consideration the probability to stick onto the surface grows to the maximal value equal to unity as the incident kinetic energy of the atom approaches zero, $s \xrightarrow[E_i \to 0]{} 1$. Some time after sticking onto the surface the atom can desorb from the surface, obtaining the necessary energy from the surface lattice oscillations. However, this desorption process is inelastic with respect to the incidence of the atom onto the surface. From the quantum-mechanical point of view the adsorption of a cold atom to a surface has a completely different character. At low incident energy the atom's wave nature dominates over its classical nature of a particle. The atom is described rather by a de Broglie wavelength $\lambda_{dB} = h/(mv)$, which depends on the mass m and velocity v of the atom and has a pure quantum mechanical character (the proportionality to the Planck's constant h).

By lowering the energy of the incident wave a growing fraction is reflected from an attractive part of the potential. Consequently, the intensity reaching the region of short range forces close to the surface diminishes. It has been realized already 70 years ago that reflection at large distance from the surface would lead to the suppression of the sticking process [Lennard-Jones and Devonshire, 1936]. Is was proposed that the origin of the reflection is the break-down of the WKB-approximation [Böheim and Brenig, 1982]. However, no detailed explanation of the reflection mechanism was given. It was in fact experimentally observed that the sticking coefficient approaches zero when decreasing the incident energy of the atom down to zero, $s \xrightarrow[E_i \to 0]{} 0$ [Yu et al., 1993]. This effect could not be explained in terms of classical adsorption. Therefore the phenomenon of reflection at low incident energy was called quantum reflection.

2.4.1 Vanishing of the wave function amplitude near the surface

Many authors of theoretical works on quantum reflection supposed, that the proportionality of the wave function amplitude near the surface to the incident wave number k_i, $|\Psi(r)| \propto k_i$, is a necessary condition for the existence of quantum reflection ([Chung and George, 1988], [Böheim and Brenig, 1982], [Doak and Chizmeshya, 2001]). This linear decrease of the wave function amplitude at vanishing incident wave number leads to the "universal" sticking behavior, $s \propto \sqrt{E_i}$, which does not depend directly on the shape of the attractive interaction potential. The real phenomenon, quantum reflection from an attractive potential, however, occurs at incident energies, larger than those required by the latter condition. We will show, that the energies for the "universal" sticking behavior lie in the energy range of the low-energy asymptote. At these incident energies only a small part of the intensity reaches the surface through a "badland". The transmission coefficient in the case of the low-energy limit is proportional to the incident energy, and the transmitted wave function amplitude is, of course, a linear function of the incident wave number k_i.

Firstly it will be shown that the wave function amplitude is in fact proportional to k_i near the surface at very small incident atom energies $E_i \propto k_i^2$. These calculations are presented in detail in [Böheim and Brenig, 1982]. For simplicity, a hard wall non-retarded potential, Eq. (2.23), is used (see Fig. 2.2). By normalizing the coordinate r to the position of the potential minimum a, $r \to r/a$, the dimensionless Schrödinger equation for the incident wave can be written as

$$\Psi''_{k_0}(r) + \left(\frac{g^2}{r^3} + k_0^2\right)\Psi_{k_0}(r) = 0, \tag{2.114}$$

with the boundary condition $\Psi_{k_0}(1) = 0$. The dimensionless parameter $g = \sqrt{2ma^2V_0/\hbar^2}$ represents the coupling constant. The local wave number is equal to $k = \sqrt{k_0^2 + g^2/r^3}$ and correspondingly the local de Broglie wavelength is represented by $\lambda_{dB} = 2\pi/k = 2\pi(k_0^2 + g^2/r^3))^{-1/2}$.

At zero incident energy, $E_i = 0$, the solution of the Schrödinger equation for a general long range potential $\propto r^{-n}$

$$\Psi''_0(r) + \frac{g^2}{r^n}\Psi_0(r) = 0 \tag{2.115}$$

with the boundary condition $\Psi_0(1) = 0$ is given by

$$\Psi_0(r) = A\sqrt{r}\left[N_{\frac{1}{n-2}}\left(\frac{2g}{n-2}\cdot r^{\frac{2-n}{2}}\right) - \frac{N_{\frac{1}{n-2}}(\frac{2g}{n-2})}{J_{\frac{1}{n-2}}(\frac{2g}{n-2})}J_{\frac{1}{n-2}}\left(\frac{2g}{n-2}\cdot r^{\frac{2-n}{2}}\right)\right]. \tag{2.116}$$

Here, $N_{\frac{1}{n-2}}$ and $J_{1\frac{1}{n-2}}$ are the Neumann and Bessel functions of the $(n-2)^{-1}$ order, respectively, and A is some constant. At the potential power $n = 3$ the zero-energy solution is

$$\Psi_0(r) = A\sqrt{r}\left[N_1\left(\frac{2g}{\sqrt{r}}\right) - \frac{N_1(2g)}{J_1(2g)}J_1\left(\frac{2g}{\sqrt{r}}\right)\right]. \tag{2.117}$$

Next, two important approximations are made:
1) The coupling constant g is suggested to be large, such that $2g \gg 1$. In real systems the parameter g is of order of 10, so that this approximation is reasonably well satisfied. Thus, $N_1(2g)$ and $J_1(2g)$ are determined by the asymptotic expansions for large arguments

$$\begin{aligned} N_1(2g) &= \sqrt{\frac{2}{\pi 2g}}\sin\left(2g - \frac{3}{4}\pi\right), \\ J_1(2g) &= \sqrt{\frac{2}{\pi 2g}}\cos\left(2g - \frac{3}{4}\pi\right). \end{aligned} \tag{2.118}$$

2) The wave function is considered at large distances between an atom and a surface, where the Neumann and Bessel functions have asymptotic expansions for small arguments

$$\begin{aligned} N_1\left(\frac{2g}{\sqrt{r}}\right) &\approx \frac{1}{\pi}\left[\frac{2g}{\sqrt{r}}\ln(\gamma\frac{2g}{2\sqrt{r}}) - 2(\frac{2g}{\sqrt{r}})^{-1} - \frac{2g}{2\sqrt{r}}\right], \\ J_1\left(\frac{2g}{\sqrt{r}}\right) &\approx \frac{2g}{2\sqrt{r}}. \end{aligned} \tag{2.119}$$

Here, γ is determined through the Euler-Mascheroni constant $C = \ln\gamma \approx 0.5772$.

Using these two approximations we obtain the form of the zero-energy wave function $\Psi_0(r)$ at large distances from the surface

$$\Psi_0(r) \approx -Ag\left[\tan(2g - \frac{3}{4}\pi) + \frac{1}{\pi}\left(\ln(\frac{r}{(\gamma g)^2}) + \frac{r}{g^2} + 1\right)\right]. \tag{2.120}$$

In the square brackets the leading term at large distances is $r/(\pi g^2)$, so that we can write

$$\Psi_0(r) \approx -A\frac{r}{\pi g}. \tag{2.121}$$

In the case if $k_0 \gg g^2 r^{-3}$ the wave function $\Psi_{k_0}(r)$ at large distances and nonzero k_0 can be represented by

$$\Psi_{k_0}(r) \approx \sin(k_0 r + \delta(k_0)), \tag{2.122}$$

where $\delta(k_0)$ is some phase shift.

The distance r_0, where the incident kinetic energy and the absolute value of the local potential energy are equal, $E_i = |V(r_0)|$, separates two regions of distances, where $k_0^2 \ll g^2 r^{-3}$ and $k_0^2 \gg g^2 r^3$. The first of these regions lies closer to the surface than the second one. In order to construct one continuous function we match both wave functions Eq. (2.121) and Eq. (2.122) in the separation point r_0. From the matching condition, $\Psi_0'(r_0)/\Psi_0(r_0) = \Psi_{k_0}'(r_0)/\Psi_{k_0}(r_0)$, we see that $\Psi_0(r_0) \propto \Psi_{k_0} = \sin(k_0 r_0 + \delta(k_0))$, which is approximately equal to $k_0 r_0$ at very small k_0. By comparing this formula with Eq. (2.121) we obtain

$$A \propto \pi g k_0, \tag{2.123}$$

which gives a proportionality of the wave function amplitude $|\Psi_{k_0}(r)|$ to k_0 at the distances $r < r_0$. This means, that at very small incident energy the turning point, which is situated at the repulsive potential wall, smears out to a turning region up to the distance r_0.

The calculations given above are valid only if r_0 is situated far from the surface, so that the incident energy is very small. The required energy value is given in [Böheim and Brenig, 1982] by the value which leads to the WKB-approximation break-down (see Section 2.1.3). It is, however, impossible to extract from these calculations a quantitative description of the quantum reflection mechanism. One can only specify that reflection occurs at distances larger than r_0. Interestingly, the low-energy quantum reflection leads to a linear vanishing of the wave function amplitude at the distances between the surface and the badland (or r_0). Obviously, the theory of [Böheim and Brenig, 1982] is equivalent with the low-energy approximation in the theory of [Friedrich et al., 2002].

Sufficiency condition for the linearity of the wave function amplitude with respect to k_0 In [Doak and Chizmeshya, 2001] it was calculated numerically that at $k_0 \leq k_{QR}$, where

$$k_{QR} = \left(\frac{(2-n)^2}{4}\right)^{\frac{n}{2(n-2)}} \beta_n^{-1}, \tag{2.124}$$

the absolute value of the wave function amplitude vanishes linearly with k_0 below the distance $r_0 = (\beta_n^{n-2}/k_0^2)^{1/n}$. In Eq. (2.124) n is the power of

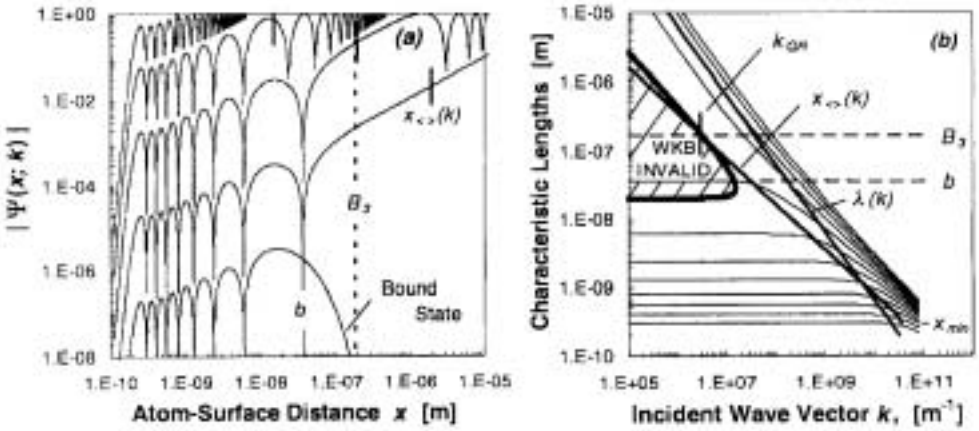

Figure 2.6: (a) The absolute value of the wave function versus the atom-surface distance x for five different values of the incident wave number $k = 10^{10}$, 10^8, 10^6, 10^4 and $10^2\,\mathrm{m}^{-1}$, from top to bottom. The vertical dashed line depicts the characteristic length $x = B_3$ given by Eq. (2.125) for the system ^{4}He-Cu(111). The short vertical bars denote the distances $x_{<>}(k)$ of equal potential and initial kinetic energies. At $x_{<>}(k) \geq B_3$ the regime of linear vanishing of $|\Psi|$ with k occurs below $x_{<>}(k)$. (b) All characteristic lengths k_{QR}, $x_{<>}(k)$ and the de Broglie wavelength $\lambda(k)$ are plotted as a function of the incident wave number k. The region of the WKB-approximation break-down is indicated by the thick solid line. Both (a) and (b) are extracted from [Doak and Chizmeshya, 2001].

the attractive interaction potential and $\beta_n = (2mC_n/\hbar^2)^{1/(n-2)}$ denotes the potential length parameter. The wave function amplitude vanishes with k_0, if r_0 is equal to or exceeds the characteristic length,

$$B_n = (4(2-n)^{-2})^{1/(n-2)}\beta_n. \tag{2.125}$$

In this case the sufficiency condition (2.124) is satisfied. Table 2.5 lists the maximal values for $k_0\beta_n$ for different potential powers n, for which the linear behavior of the wave function amplitude is fulfilled. For $n = 3$ and $n = 4$ these values are of order of G_n, given in Table 2.4. This confirms once again the fact, that the linearity of the wave function amplitude with respect to k_0 appears only in the low-energy asymptotic range.

Fig. 2.6 (a) from [Doak and Chizmeshya, 2001] shows the absolute value of the wave function $|\Psi(x,k)|$ versus the atom-surface distance x for different k_0 (denoted as k in the figure). The figure is given for the case of the non-retarded attractive potential in the system ^{4}He-Cu(111). The values of $k_0\beta_3$

n	3	4	5	6	7
$k_{QR}\beta_n$	0.09	1.00	1.97	2.83	3.61

Table 2.5: The maximal value of $k_0\beta_n$, $k_{QR}\beta_n$, at which the wave function amplitude is proportional to k_0, in dependence on the potential power n.

are equal to 512, 5, 5 10^{-2}, 5 10^{-4} and 5 10^{-6} from the top to the bottom curve, respectively. The short vertical bars on each curve indicate the distances r_0, at which the magnitudes of the incident kinetic and local potential energies are equal. In the figure r_0 is denoted as $x_{<>}(k)$. Fig. 2.6 (b) displays the characteristic lengths k_{QR}, r_0 and $\lambda(k_0) = 2\pi/k_0$. The range, in which the WKB-approximation (2.16) is not valid, is depicted by the thick solid line.

2.4.2 Sticking to the surface of liquid ^{4}He

The first theoretical and experimental works on quantum reflection focused on scattering of a light neutral atom (hydrogen, helium) from the surface of liquid ^{4}He. The interaction hydrogen-liquid helium is an intensely investigated system with only one well-defined bound state of the energy on the order of -1 K. The excitations of liquid helium are also well-known and experimentally observed.

The theory of specular reflection of an atom from the liquid helium surface including the coupling to surface ripplons was firstly described in [Zimmerman and Berlinsky, 1983] and reviewed in [Basdevant and Dalibard, 2000].

A liquid ^{4}He film on a solid substrate has a sharp density profile

$$\rho(\vec{r}, z) = \rho_0 \theta(-(z + \widehat{h}(\vec{r}))). \tag{2.126}$$

Here, z denotes the coordinate perpendicular to the surface, $\vec{r}$ is a two-dimensional coordinate vector in the plane $z = 0$, $\rho_0 = 0.145$ g/cm^3 denotes the ^{4}He bulk density and $\theta(-(z + \widehat{h}(\vec{r})))$ is the Heaviside step-function

$$\theta(-(z + \widehat{h}(\vec{r}))) = \begin{cases} 0 & \text{at } z + \widehat{h}(\vec{r}) \geq 0, \\ 1 & \text{at } z + \widehat{h}(\vec{r}) < 0. \end{cases} \tag{2.127}$$

The operator $\widehat{h}(\vec{r})$ determines the height profile of the surface. The system hydrogen - liquid ^{4}He is schematically depicted in Fig. 2.7.

Even at zero temperature there are elementary quantized excitations in the film, so-called ripplons. These excitations are described by the Hamilto-

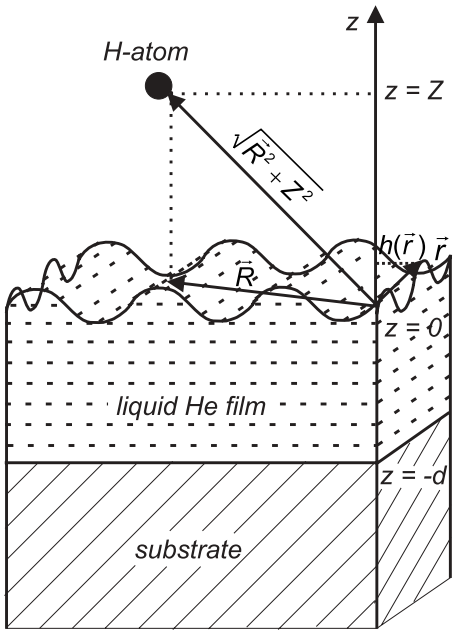

Figure 2.7: Schematic illustration of a hydrogen atom with coordinates $(\vec{R}, Z)$ inciding onto the surface of a liquid helium film of thickness d deposited on a substrate. The surface has a height profile $h(\vec{r})$.

nian

$$\widehat{H}_{ripp} = \sum_{q}^{q_{max}} \hbar\omega_q \widehat{r}^{+}_{\vec{q}} \widehat{r}_{\vec{q}}, \tag{2.128}$$

where $\widehat{r}^{+}_{\vec{q}}$ and $\widehat{r}_{\vec{q}}$ represent the ripplon creation and annihilation operators and ω_q is the frequency of the ripplon state $|q\rangle$ with the wave number $q = |\vec{q}|$. The surface height fluctuations can be expressed in terms of the ripplons through

$$\widehat{h}(\vec{r}) = \frac{1}{\sqrt{L_x L_y}} \sum_{q} h_q (\widehat{r}^{+}_{\vec{q}} e^{-i\vec{q}\vec{r}} + \widehat{r}_{\vec{q}} e^{i\vec{q}\vec{r}}) \qquad \text{with } h_q = \sqrt{\frac{\hbar q}{2\rho_0 \omega_q}}. \tag{2.129}$$

In this equation the proportionality to $(L_x L_y)^{-1/2}$ occurs because of the normalization of the wave function squared to the volume $L_x L_y L_z$ of some box.

The dispersion relation for the ripplons of the liquid helium film of a thickness d is given in [Berkhout and Walraven, 1992] by

$$\omega_q^2 = \left[\left(g + \frac{3C_3}{m_{He} d^4} \right) q + \frac{\gamma}{\rho_0} q^3 \right] \tanh(qd), \tag{2.130}$$

where $\gamma = 3.54 \cdot 10^{-4}$ Jm^{-2} is the ^{4}He surface tension, g is the gravitational acceleration constant, C_3 is of the order of 0.1 eVÅ^3 [Webster et al., 1980] and

denotes the strength of the van der Waals potential between liquid He-atoms and the subtrate and $m_{He} = 6.68 \cdot 10^{-27}$ kg is the mass of the ^{4}He-atom.

For a thick helium film ($d \gtrsim 1$ μm) the dispersion relation (2.130) takes the form

$$\omega_q^2 = gq + \frac{\gamma}{\rho_0} q^3. \tag{2.131}$$

A neutral hydrogen atom with the coordinates $(\vec{R}, Z > 0)$ propagates in the effective atom-surface potential

$$V(\vec{R}, Z) = n_{He} \int d^2\vec{r} \int_{-\infty}^{+\infty} dz U(\sqrt{(\vec{R} - \vec{r})^2 + (Z - z)^2})\theta(\widehat{h}(\vec{r}) - z), \tag{2.132}$$

where n_{He} denotes the ^{4}He density and U is the interaction potential between a H-atom and a ^{4}He-atom.

By placing the expression (2.129) for $\widehat{h}(\vec{r})$ into Eq. (2.132), expanding θ into a Taylor series, $\theta(\widehat{h}(\vec{r} - z)) \simeq \theta(-z) - \theta'(-z)\widehat{h}(\vec{r})$, and taking into account that $\theta'(-z) = \delta(-z)$ we obtain

$$V(\vec{R}, Z) \simeq V_0 Z - n_{He} \int d^2\vec{r} U(\sqrt{(\vec{R} - \vec{r})^2 + Z^2}) \sum_q h_q(\widehat{r}_q^+ e^{-i\vec{q}\vec{r}} + \widehat{r}_q e^{i\vec{q}\vec{r}}). \tag{2.133}$$

This expression can be rewritten as

$$V(\vec{R}, Z) \simeq V_0(Z) + \sum_q (h_q(\widehat{V}_{\vec{q}} e^{-i\vec{q}\vec{R}} + \widehat{V}_{-\vec{q}} e^{i\vec{q}\vec{R}}), \tag{2.134}$$

with

$$\begin{aligned} \widehat{V}_{\vec{q}} &= n_{He} \int d^2\vec{r'} \widehat{r}_q^+ e^{i\vec{q}\vec{r'}} U(\sqrt{\vec{r'}^2 + Z^2}), \\ \widehat{V}_{-\vec{q}} &= n_{He} \int d^2\vec{r'} \widehat{r}_q e^{-i\vec{q}\vec{r'}} U(\sqrt{\vec{r'}^2 + Z^2}), \end{aligned} \tag{2.135}$$

where $\vec{r'} = \vec{R} - \vec{r}$.
In equations (2.133) and (2.134) the first term

$$V_0(Z) = n_{He} \int d^2\vec{r} \int_{-\infty}^{+\infty} dz U(\sqrt{(\vec{R} - \vec{r})^2 + (Z - z)^2})\theta(-z) = -\frac{C_3}{Z^3} \tag{2.136}$$

represents the long-range attractive interaction potential between the atom and the flat surface. The second term is the interaction with surface atoms, located below or above $z = 0$ and describes the coupling to the ripplons.

In a closed system the energy during the scattering process must be conserved, $E_i = E_f$. The initial state kinetic energy E_i is a sum of the energies perpendicular and parallel to the surface

$$E_i = \frac{\hbar^2(k_\perp^2 + k_{||}^2)}{2m}, \tag{2.137}$$

where m denotes the mass of the H-atom. By the coupling to the surface at the distance of some Å the energy normal to the surface is transformed into the binding energy $E_B < 0$, thereby exciting resonantly a ripplon with frequency ω_q. The energy parallel to the surface changes only because of the modification of the parallel wave vector from $\vec{k}_{||}$ to $\vec{k}_{||} - \vec{q}$. Thus, the energy of the final state is given by

$$E_f = E_B + \frac{\hbar^2(\vec{k}_{||} - \vec{q})^2}{2m} + \hbar\omega_q. \tag{2.138}$$

Since $\hbar^2 q^2/(2m)$ is comparable to E_B we can set $\hbar^2(\vec{k}_\perp \vec{q})/m = \sqrt{2}\hbar k_\perp/\sqrt{m} \cdot \hbar q\sqrt{2m} \simeq \sqrt{2}\hbar k_\perp \sqrt{E_B}/\sqrt{m} = \sqrt{2\hbar^2 k_\perp^2 E_B/m}$. For the same reason the term in the dispersion relation (2.130), which contains the gravitational constant g, is negligible with respect to the other term, $gq \sim g\sqrt{2mE_B/\hbar^2} \simeq 10^{10}$ $\mathrm{s}^{-2} \ll \gamma q^3/\rho_0 \sim \gamma(2mE_B/\hbar^2)^{3/2}/\rho_0 \simeq 10^{22}$ s^{-2}. Thus, the dispersion relation Eq. (2.130) can be approximated by

$$\omega_q^2 = \frac{\gamma}{\rho_0} q^3. \tag{2.139}$$

We now assume that the incident energy perpendicular to the surface is negligible with respect to the bound state energy, $\hbar^2 k_\perp^2/(2m) \ll E_B$. By using this approximation and the dispersion relation (2.139) the equation for the energy conservation

$$\frac{\hbar^2(k_\perp^2 + k_{||}^2)}{2m} = E_B + \frac{\hbar^2(\vec{k}_{||} - \vec{q})^2}{2m} + \hbar\omega_q \tag{2.140}$$

takes the form

$$\frac{\hbar^2 q^2}{2m} + \hbar\sqrt{\frac{\gamma}{\rho_0}} q^{\frac{3}{2}} = |E_B|. \tag{2.141}$$

In the scattering process elastic reflection from the repulsive potential wall cannot be taken into account. If we want to consider this type of reflection we must add to the right-hand side of Eq. (2.140) the term $const\ \hbar^2 k_\perp^2/(2m)$ with $0 < const < 1$. This term stands for the constant energy part of the wave reflected from the repulsive wall. However, since we assumed $\hbar^2 k_\perp^2/(2m) \ll E_B$

the reflected energy *const* $\hbar^2 k_\perp^2/(2m)$ is much smaller than E_B and therefore must be neglected in the frame of this theory.

The transition probability for an atom from the initial state $|i\rangle$ to the final state $|f\rangle$ per unit time is given by [Davydov, 1976]

$$p_{i\to f} = \frac{2\pi}{\hbar}|\langle f|\widehat{V}|i\rangle|^2\delta(E_f - E_i). \tag{2.142}$$

In this expression, $\widehat{V}$ represents the perturbation operator, which couples state $|i\rangle$ to state $|f\rangle$. Since the final state has a finite energy width dE_f, the correct probability for a $i \to f$ transition results from the integration over the level density of final states $\rho(E_f)$. Thus we obtain the well-known Fermi's Golden Rule for the case $E_i = E_f$, which is of particular interest here,

$$P_{i\to f} = \int p_{i\to f}\rho(E_f)dE_f = \frac{2\pi}{\hbar}|\langle f|\widehat{V}|i\rangle|^2\rho(E_f) \qquad \text{at } E_f = E_i. \tag{2.143}$$

This transition probability with energies E_i and E_f given by Eq. (2.137) and (2.138) describes nothing else than the adsorption probability into the bound state, which is accompanied by one ripplon excitation. We can write the sticking coefficient by normalizing $P_{i\to f}$ to the incident flux $vL_z^{-1} = \hbar k_\perp L_z^{-1}/(2m)$,

$$s = \frac{P_{i\to f}}{vL_z^{-1}} = \frac{2\pi}{\hbar}|\langle f|\widehat{V}|i\rangle|^2\rho(E_f)\frac{2mL_z}{\hbar k_\perp}. \tag{2.144}$$

To calculate the level density of the final state $\rho(E_f)$ we consider a ring in the wave number space, which has the radius q and the thickness dq (see Fig. 2.8) [Cassels, 1982]. The volume of this ring is given by $a_q = 4\pi q^2 dq$. The number of eigenvalues of q_x in the interval dq_x is equal to $L_x/(2\pi)$ and the number of eigenvalues of q in the volume $dq = dq_x dq_y dq_z$ amounts to $L_x L_y L_z/(2\pi)^3$. Thus, the number of levels $|f\rangle$ in the volume a_q is equal to $dN = L_x L_y L_z a_q/(2\pi)^3$. Using the expression (2.138) for the energy of the final state we obtain

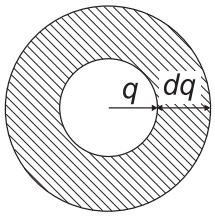

Figure 2.8: A ring of the radius q and the thickness dq in the wave number space.

$$dq = \left(\frac{\hbar^2}{m}q + \frac{3}{2}\hbar\sqrt{\frac{\gamma}{\rho_0}}q^{\frac{3}{2}}\right)^{-1} dE_f. \tag{2.145}$$

By placing this equation into the expression for dN we obtain the relation between dN and dE_f

$$dN = \frac{L_x L_y L_z}{(2\pi)^3}\cdot\frac{4\pi q^2}{\frac{\hbar^2}{m}q + \frac{3}{2}\hbar\sqrt{\frac{\gamma q}{\rho_0}}}dE_f. \tag{2.146}$$

Since ρ is defined as $\rho(E_f) = dN/dE_f$ it is clear that

$$\rho(E_f) = \frac{L_x L_y L_z}{2\pi^2\hbar} \cdot \frac{mq}{\hbar + \frac{3}{2}m\sqrt{\frac{\gamma}{\rho_0 q}}}. \tag{2.147}$$

As expected, the density $\rho(E_f)$ has the dimensionality of inverse energy, J^{-1}.

At the sticking process of a hydrogen atom onto the liquid ^{4}He-surface one ripplon is excited. Thus, only the ripplon creation operator plays a role, i.e. the perturbation $\widehat{V}$ is equal to $\widehat{V}_{\vec{q}}$.

In the following, we make the very important assumption that the incident wave function of the initial state $|i\rangle$ is proportional to the square root of the normal incident energy $\hbar k_\perp/\sqrt{2m}$. Thus, we obtain

$$\langle f|\widehat{V}_{\vec{q}}|i\rangle = \frac{\hbar k_\perp}{\sqrt{2mL_z}} M(\vec{q}), \tag{2.148}$$

where $M(\vec{q})$ is the proportionality coefficient. This assumption has already been discussed in Sec. 2.4.1. It is based on the fact that strong quantum reflection takes place far from the surface.

The proportionality of $\langle f|\widehat{V}_{\vec{q}}|i\rangle$ to $L_z^{-1/2}$ results from the normalization of the normal incident wave function squared to L_z^{-1} (free wave function) and of the final normal wave function squared to unity (localized wave function). Obviously, $\langle f|\widehat{V}_{\vec{q}}|i\rangle$ has the dimensionality of energy, J, and $M(\vec{q})$ has the unit $(\mathrm{Jm})^{1/2}$.

By placing Eq. (2.148) into Eq. (3.15) we obtain the proportionality of the sticking coefficient to the normal wave number $k_\perp$ and subsequently, to the square root of the normal incident energy $E_i \cos\theta_i$,

$$s = \frac{L_x L_y L_z}{\pi\hbar} \cdot \frac{2mq^{\frac{3}{2}}|M(\vec{q})|^2\sqrt{\rho_0\gamma}}{3m\gamma + 2\hbar\sqrt{\gamma\rho_0 q}} k_\perp \propto k_\perp = \sqrt{E_i \cos\theta_i}, \tag{2.149}$$

where θ_i denotes the incident angle between the atomic beam axis and the surface normal. The proportionality coefficient $s/k_\perp$ differs from the one obtained in [Basdevant and Dalibard, 2000]. In contrast to the latter one, $s/k_\perp$ in Eq. (2.149) has the expected dimensionality of a length, m. We therefore claim Eq. (2.149) to be correct.

Numerous experiments have been performed in order to confirm the predicted proportionality of the sticking coefficient to the square root of the incident normal energy at small values [Doyle et al., 1991, Yu et al., 1993, Berkhout and Walraven, 1992]. It was observed that only sticking to a thick liquid helium film or to a liquid helium bulk leads to this energy dependence. Fig. 2.9 (a) from [Doyle et al., 1991] shows that the theoretically predicted

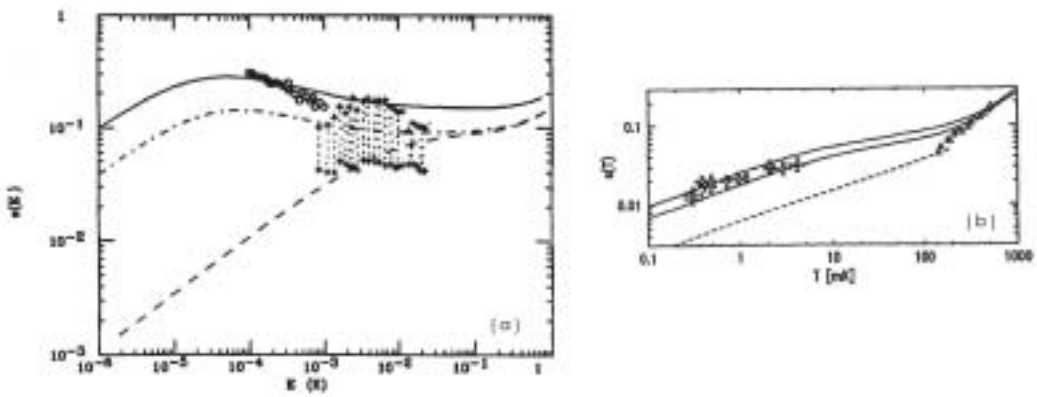

Figure 2.9: The dependence on the atom energy E (or the temperature $T = E/k_B$) of the sticking probability (a) onto a thin liquid-^{4}He film and (b) onto a thick liquid-^{4}He film. (a), circles and crosses with error bars: experimental data, obtained in [Doyle et al., 1991]; solid and the dot-dashed lines: different theoretical curves for the sticking onto a thin film; dashed line: theoretically predicted sticking on bulk helium. (b), circles with error bars: experimental "universal" sticking coefficient $s \propto \sqrt{T}$ from [Yu et al., 1993]; triangles: experimental data of [Berkhout et al., 1989] at energies comparable to the bound state energy ("non-universal" sticking); solid lines (the binding energies were taken to be 1.1 and 1.0 K for these two curves) and dashed line represent two different theoretical predictions.

dependence of s on the energy for a thin He film (solid and dot-dashed lines) differs from that for a bulk (dashed line). This results from the fact that the substrate below the He film attracts the atom and the effective atom-surface interaction potential becomes deeper than in the case of a liquid He bulk or a thick film [Carraro and Cole, 1998]. In the deeper potential, a second bound state appears leading to a larger sticking probability. The experimental data were obtained at MIT [Doyle et al., 1991] for hydrogen atoms sticking to a relatively thin (on the order of 50 Å) liquid helium film. The H-atoms were magnetically trapped and evaporatively cooled down to temperatures in the submillikelvin regime.

Fig. 2.9, (b) depicts the experimental results for H-atoms sticking onto a thick (> 150 Å) film [Yu et al., 1993]. The proportionality of the sticking coefficient to the square root of the atom temperature ($s = (0.30 \pm 0.03)\sqrt{T}$) is clearly observed in the range of the temperature $T = E_i/k_B$ between 0.1 and 10 mK (open circles). At higher atom temperatures the energy-dependence of the sticking coefficient does not display this universal form. In the experiment of Berkhout and Walraven [Berkhout and Walraven, 1992] the function

$s(T)$ is observed rather to be linear with T ($s(T) = 0.33\ T$) for atom temperature being between approximately 100 and 1000 mK (open triangles). Solid and dashed lines in this figure represent the different theoretical predictions. In this case, the sticking coefficient is strongly dependent on the shape of the long-range attractive atom-surface interaction potential, including retardation at large distances. The linear vanishing of the wave function amplitude with $k_\perp$ which is a sufficient condition for universal sticking behavior is only valid in the low-energy range.

The universality of the sticking coefficient in the system of a light atom scattering from a thick liquid helium film provides qualitative information about quantum reflection. At low incident energies the reflection from the repulsive wall contributes only negligibly to the reflection amplitude. This universal behavior is, however, a peculiar feature of the system light atom scattering from a thick liquid helium film. This is due to the existence of only one bound state. Thus, studying the behavior of the sticking coefficient is not a general method for the investigation of quantum reflection even in the low energy limit.

Moreover, at higher energies it is impossible to separate reflection from the repulsive wall from quantum reflection by measuring the sticking coefficient. This difficulty can be overcome by choosing an experimental configuration, in which the short-range coupling to the surface is absent. The experiments discussed in this work are carried out with such a system, i.e. ^{3}He scattering from an atomically rough surface (see chapter 4).

Chapter 3

Casimir effect

The measurement of quantum reflection of an atom from a surface as a method for sensitive probing of the attractive long-range potential can be used for observing the delicate Casimir effect. This chapter presents an introduction into this well-known effect and the Casimir-van der Waals potential is discussed in detail for the relevant case of atom-surface interaction.

In the first part, the van der Waals and Casimir interactions are described qualitatively and the general expression for the Casimir-van der Waals force is presented. In particular, the cases of an atom interacting with a dielectric and a metal surface are considered. In this work, the well-known description for the atom-surface system is extended in order to include the influence of finite temperature and imperfectly conducting surfaces. Besides, the influence of the microscopic surface disorder is studied and the possibility of detecting the atomic roughness of the surface by utilizing quantum reflection is pointed out. The derived corrections are required for the analysis of the experimental data which is presented in chapter 4.

3.1 Van der Waals and Casimir potentials

Van der Waals forces The force acting between two atoms or between an atom and a surface at distances of a few Angsröm or larger is the so-called van der Waals force. This force belongs to the dispersion forces which are named according to their relation to the dispersion of light in the UV and visible parts of the spectrum.

The dispersion forces have the following properties: They are
1) long-range forces;
2) of quantum-mechanical nature;
3) non-additive;

4) repulsive or attractive. For the atom-atom or atom-surface interaction in vacuum they are always attractive.

The van der Waals force is electromagnetic in origin and can be called polarization force or fluctuating dipole force. Its quantum-mechanical nature reveals itself for example in the interaction of two helium atoms whose classical electric dipole moments are equal to zero. From the quantum-mechanical point of view there exists a non-zero atomic dipole because of fluctuations of the electron distribution resulting in its temporary asymmetry with respect to the atom core. The time average of the temporary dipole moment, however, vanishes. When approaching another atom, the electric field of this temporary dipole induces a dipole in the neighboring atom. Both dipoles interact with each other during a finite time resulting in a non-zero time averaged van der Waals force. Formaly, the quantum-mechanical character of the force is expressed by its proportionality to Planck's constant $\hbar$.

The non-additive character of the polarization force means that the interaction potential of three bodies is not equal to the sum of all independent two-body interaction potentials. For instance, the atom-surface interaction is only qualitatively described through the pairwise summation of the interactions between the incident atom with all atoms of the crystal. This potential acting on the incident atom at the distance r from the surface is in first approximation given by

$$V(r) = -\frac{\pi C_6 \rho}{6r^3} \stackrel{def}{=} -\frac{C_3}{r^3}. \tag{3.1}$$

Here, ρ denotes the atom density in the crystal and

$$C_6 = -\frac{3}{2} \cdot \frac{\alpha_1 \alpha_2}{(2\pi\epsilon_0)^2} \cdot \frac{I_1 I_2}{I_1 + I_2} \tag{3.2}$$

is the strength coefficient of the interaction between the incident atom and one of the crystal atoms, as it was calculated by London in 1930 (see also [Israelachvili, 1985]). $\alpha_{1,2}$ and $I_{1,2} \propto \hbar$ represent the electric polarizabilities and the first ionization potentials of both atoms, respectively, and $\epsilon_0 = 8.854 \cdot 10^{-12}$ $\mathrm{C^2 J^{-1} m^{-1}}$ is the vacuum permittivity.

In the description of the atom-surface potential by summation over atom-atom potentials the influence of the interaction between the surface atoms and their influence on the dipole moment of the incident atom are not taken into account. Therefore the resulting interaction potential is only a rough estimate. The problem of non-additivity can be avoided by representing the surface as a continuous medium, as it is done in the Lifshitz theory [Lifshitz and Pitaevskii, 1980]. This theory describes the medium in terms of the dielectric constant or the refractive index. The atom falling onto the

surface is assumed as a positive core and an electron oscillating at distance u around the core. The core, which at large distance r from the surface is represented as a point charge $+e$, induces the image point charge $q = e(1-\epsilon)/(1+\epsilon)$ located at the same distance from the surface within the crystal [Lüth, 1993]. Here, ϵ denotes the crystal dielectric constant.

The Coulomb interaction between all pairs of real and image charges averages out to zero. The non-zero dipole-induced dipole interaction determines the atom-surface potential,

$$V(r) = -\frac{\epsilon - 1}{\epsilon + 1} \cdot \frac{d^2}{16\pi\epsilon_0} \cdot \frac{1}{r^3}, \tag{3.3}$$

where $d = eu$ denotes the temporary dipole moment of the incident atom. For a perfect conductive (metal) surface ($\epsilon \to \infty$) the coefficient $(\epsilon-1)/(\epsilon+1)$ is equal to unity.

More precisely, the potential strength C_3 at the interaction of an atom with a perfectly conductive surface is represented in [Marinescu et al., 1997] by

$$C_3 = \frac{1}{4\pi} \int_0^\infty \alpha_d(i\omega) d\omega, \tag{3.4}$$

where $\alpha_d(i\omega)$ is the complex frequency (ω)-dependent polarizability of the incident atom.

Effect of retardation The atom-surface interaction can be described by the expression $V(r) = C_3/r^3$ only if the atom is not located very far from the surface. If, however, the propagation time of the electric field signal from the atom to the surface and back becomes comparable with the period of the atom dipole fluctuation, the dipole induced by this electric field interacts with the dipole of the incident atom, which has already changed. Due to the phase shift of the interacting dipoles the interaction potential becomes weaker and therefore the potential falls off faster than $\propto r^{-3}$. This effect is called the retardation effect. Qualitatively, the atom-surface distance, at which the retardation plays a role, can be written as $r_{ret} = ct_{ret} \sim 137a_0 \approx 10\,\text{nm}$, where c represents the speed of light, $a_0 = 0.592\,\text{Å}$ denotes the Bohr radius and $t_{ret} = \hbar/E_{Ryd} \approx 10^{-17}\,\text{s}$ is the time-scale of the dipole fluctuation, which is represented through the excitation time of a hydrogen atom ($E_{Ryd} = 13.8$ eV- the Rydberg energy) [Bruder, 1997]. More precisely, the time t_{ret} is given through the atomic transition between the ground $|g\rangle$ and the first excited $|e\rangle$ states in the atom, $t_{ret} = \hbar/E_{|g\rangle\to|e\rangle}$. Thus, the distance $r_{ret} = \lambda_{|g\rangle\to|e\rangle}/(2\pi)$ differs according to the species of the incident atom. Here, $\lambda_{|g\rangle\to|e\rangle}$ denotes the corresponding wavelength of the atomic transition $|g\rangle \to |e\rangle$.

For the surface-surface interaction in vacuum the retardation effect is much smaller than for the atom-surface interaction, because of the larger r_{ret}. This distance is defined by the characteristic adsorption lengths of the interacting surfaces, which lye in the visible or infra-red range of the spectrum. The surface-surface interaction was directly measured for the first time with two quartz glass surfaces separated by the distance of 100-400 nm [Derjaguin and Abrikossova, 1954]. By placing the interacting surfaces in another medium the retardation effect can be increased, as it was observed in the experiment with two mica surfaces in aqueous electrolyte solutions at 5-10 nm distance from each other [Israelachvili and Adams, 1978].

The retardation effect in an atom-surface system was firstly quantitatively measured only recently [Sukenik et al., 1993]. In the latter experiment a cavity was formed by two coated plates, which sodium atoms were guided through. The Lamb shift of the sodium atoms in the cavity was measured using laser spectroscopy in dependence of the atomic beam deviation from the center of the cavity. The measured Lamb shift resulting from the interaction potential is not only a function of the distance between the atoms and the center of the cavity but also of the distance between the cavity plates (see Sec. 3.2). A simpler quantitative measurement including only one surface was performed in our group and will be presented in Chapter 4.

Casimir effect The retardation effect discussed in the previous section additionally lowers monotonously the potential energy as a function of the distance between the interacting bodies. It was firstly published in 1948 by H. Casimir and D. Polder, that at distances much larger than r_{ret} the interaction potential will be represented by the product of the non-retarded potential and a function proportional to r^{-1}

$$V(r \gg r_{ret}) = V(r \ll r_{ret}) \cdot \frac{const}{r}. \tag{3.5}$$

It is logical to expect that the constant of proportionality contains the speed of light c, which manifests the nature of this retarded potential. From the expression (3.5) it is clear, that the non-retarded form of the atom-atom potential $\propto r^{-6}$ is transformed into the retarded form $\propto r^{-7}$ and the non-retarded atom-surface potential $\propto r^{-3}$ becomes proportional to r^{-4} at large distances [Casimir and Polder, 1948],

$$V_{atom-atom}(r) = -\frac{23\hbar c\alpha_1\alpha_2}{4\pi r^7} \quad \text{at } r \gg \frac{\lambda_{i_{|g\rangle\to|e\rangle}}}{2\pi}, \tag{3.6}$$

$$V_{atom-surface}(r) = -\frac{3\hbar c\alpha}{8\pi r^4} \quad \text{at } r \gg \frac{\lambda_{|g\rangle\to|e\rangle}}{2\pi}. \tag{3.7}$$

Here, α_1 and α_2 denote the static polarizabilities of the two interacting atoms (α- in the case of the atom-surface system) and $\lambda_{i_{|g\rangle\to|e\rangle}}$, ($i = 1$ or 2) is the wavelength of the lowest energy $|g\rangle \to |e\rangle$ electric dipole transition in both interacting atoms. As expected, the interaction potential is proportional to c (the nature of a retarded potential) and to $\hbar$ (the quantum-mechanical nature). The expression (3.7) is written for the case of a neutral atom interacting with a perfectly conducting surface. For a dielectric surface with the dielectric constant ϵ the interaction potential has to be multiplied by a function of ϵ. This function is calculated in [Dzyaloshinskii et al., 1961] to be equal to

$$\begin{aligned}\phi_1(\epsilon) &= \frac{\epsilon-1}{\epsilon+1}\cdot\phi(\epsilon) = \frac{1}{3}+\epsilon+\frac{4-(\epsilon+1)\sqrt{\epsilon}}{2(\epsilon-1)} - \\ &\frac{\mathrm{Arcsh}(\sqrt{\epsilon-1})}{2(\epsilon-1)^{\frac{3}{2}}}[1+\epsilon+2\epsilon(\epsilon-1)^2] + \\ &\frac{\epsilon^2}{\sqrt{\epsilon+1}}\left(\mathrm{Arcsh}(\sqrt{\epsilon})-\mathrm{Arcsh}(\sqrt{\epsilon}^{-1})\right).\end{aligned} \tag{3.8}$$

In [Spruch and Tikochinsky, 1993] the correction function is given in a different form,

$$\phi_2 = \frac{\epsilon-1}{\epsilon+\frac{37}{23}}. \tag{3.9}$$

Both functions ϕ_1 and ϕ_2 and also the correction term for van der Waals interaction between an atom and a dielectric surface $(\epsilon-1)/(\epsilon+1)$ are plotted in Fig. 3.1.

The pure retarded potential is known as a Casimir or as a Casimir-Polder potential. Although the Casimir potential was firstly calculated as an asymptotic function for the retarded van der Waals potential at very large distances, a quite different presentation of this effect is possible. This modern description comes from quantum field theory. In this theory the vacuum is represented by a resonator. The electromagnetic field in this resonator can be described through eigenmodes. Each mode corresponds to a quantum-mechanical harmonic oscillator with the frequency ω. At zero temperature of the space, there nevertheless exist zero-temperature oscillations with energy $E_0 = \hbar\omega/2$. The vacuum is then characterized by these zero-point fluctuations. The presence of some bodies in the vacuum modifies the spectrum of these zero-point fluctuations, leading to an attractive force between the bodies. This attraction can be explained by the fact, that in the space between two bodies not all vacuum modes are sustained, depending on the boundary conditions imposed by the presence of the bodies. Between two parallel

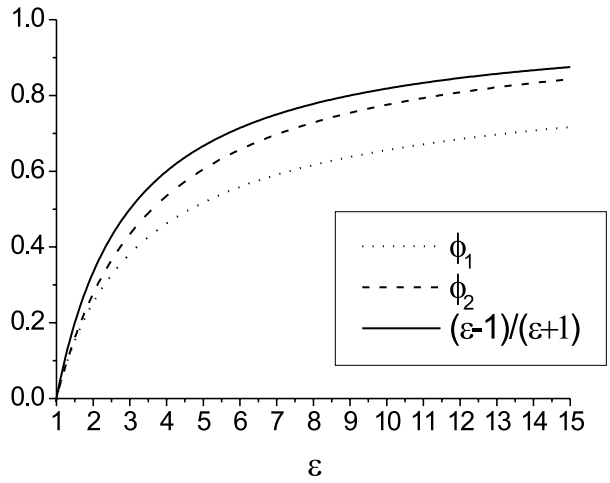

Figure 3.1: Three known functions of ϵ correcting the atom-dielectric surface interaction potential to the atom-conductive surface interaction potential.

metallic plates separated by the distance r, for example, only the modes of the wavelength λ proportional to $n \cdot r$, $n = 1, 2, 3, \ldots$ are present because of the requirement that the tangential electromagnetic field component on the metallic surface must vanish. The more densely populated spectrum outside the two bodies presses onto them, whereas the more "empty" space between them exerts a smaller pressure not compensating the pressure from outside. The force leading to the resulting attraction can be described through the difference between the zero-point energy outside the bodies and its value between them

$$F(r) = -\frac{dE(r)}{dr}. \tag{3.10}$$

At finite temperature T of the space the general expression for the force acting between two dielectric bodies at the distance r per unit area is calculated by [Dzyaloshinskii et al., 1961],

$$\begin{aligned} F(r) \;=\; & \frac{k_B T}{\pi c^3} \sum_{n=0}^{\infty\prime} \epsilon_3^{\frac{3}{2}} \xi_n^3 \int_1^\infty dp\, p^2 \Bigg(\Big(\frac{(s_1+p)(s_2+p)}{(s_1-p)(s_2-p)} e^{\frac{2p\xi_n}{c} r\sqrt{\epsilon_3}} - 1 \Big)^{-1} + \\ & \Big(\frac{(s_1+p\frac{\epsilon_1}{\epsilon_3})(s_2+p\frac{\epsilon_2}{\epsilon_3})}{(s_1-p\frac{\epsilon_1}{\epsilon_3})(s_2-p\frac{\epsilon_2}{\epsilon_3})} e^{\frac{2p\xi_n}{c} r\sqrt{\epsilon_3}} - 1 \Big)^{-1} \Bigg). \end{aligned} \tag{3.11}$$

Here, $s_i = \sqrt{\epsilon_i/\epsilon_3 - 1 + p^2}$ (i =1,2) represent the functions of the dynamic

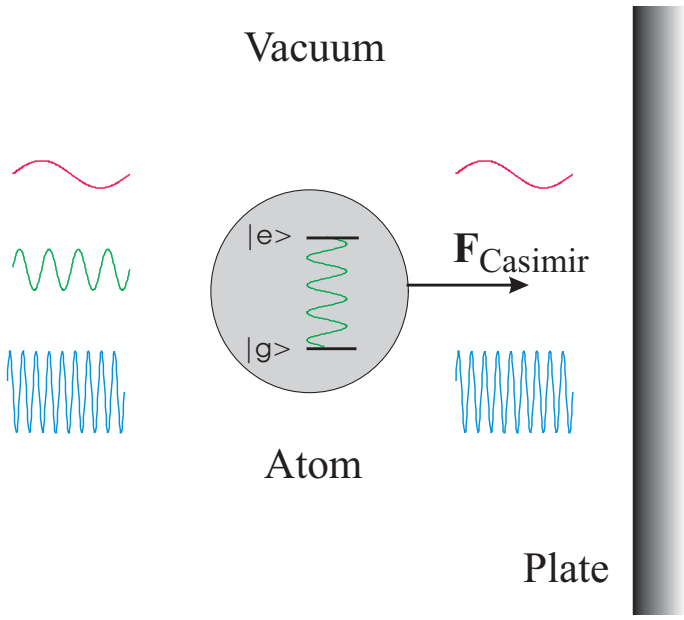

Figure 3.2: Schematical representation of an atom-plate system in vacuum. The more densely populated spectrum outside the system compared with the one inside results in a Casimir force which attracts the atom towards the plate.

dielectric constants of both interacting bodies, $\epsilon_1 = \epsilon_1(i\xi_n)$ and $\epsilon_2 = \epsilon_2(i\xi_n)$, depending on the imaginary frequency $\omega = i\xi_n$. k_B denotes the Boltzmann constant. $\xi_n = 2\pi n k_B T/\hbar$ is proportional to the integer number n. ϵ_3 is the dielectric constant of the medium separating both interacting bodies, p denotes the integration parameter and the prime on the summation sign is to show that the $(n = 0)$-term contributes only to one half to the sum. For $rk_BT/(c\hbar) \ll 1$ the sum can be replaced by the integral over $dn = d\xi\ \hbar/(2\pi k_B T)$.

For two perfectly conducting plates ($\epsilon_1,\ \epsilon_2 \to \infty$) separated by vacuum ($\epsilon_3 \to 1$) the force per unit area takes the form

$$\begin{aligned} F(r) &= \frac{k_BT}{\pi c^3} \cdot \frac{\hbar}{2\pi k_BT} \int_0^\infty d\xi_n \xi_n^3 \int_1^\infty \frac{2dpp^2}{e^{2p\xi_n r/c} - 1} = \\ & \frac{\hbar}{\pi^2 c^3} \int_1^\infty dpp^2 \int_0^\infty \frac{d\xi_n \xi_n^3}{e^{2p\xi_n r/c} - 1} = \\ & \frac{\hbar}{\pi^2 c^3} \int_1^\infty \frac{dpp^2 \pi^4}{15(2pr/c)^4} = \frac{\pi^2 \hbar c}{240 r^4}. \end{aligned} \tag{3.12}$$

At $d = 1\ \mu$m the force per unit area is equal to $0.13 \cdot 10^{-6}\,\mathrm{N/cm^2}$ which is a small but a measurable value.

The description of the Casimir force through the modification of the zero-point vacuum fluctuations allows to present the effect of this force not only as the asymptotic case of the van der Waals interaction but as an independent and many-sided quantum effect, known as the Casimir effect. This effect has been observed and plays an important role in as different fields as atomic physics, cosmology and gravitation theory [Mostepanenko and Trunov, 1997]. Moreover, the lateral Casimir effect was recently measured [Chen et al., 2002]. The dynamical Casimir effect is theoretically predicted to be observable as radiation emitted by a cavity moving in vacuum [Lambrecht et al., 1996]. The nature of the effect of sonoluminescence, which was initially unclear, can be explained by the dynamical Casimir effect [Eberlein, 1996].

3.2 Atom-wall interaction potential

Interaction between an atom and a surface At the interaction of a polarizable system (e.g. an atom) with a dielectric wall with dielectric constant ϵ through the vacuum, ϵ_1 and ϵ_2 can be rewritten by the dielectric constants of a rarified gas

$$\epsilon_1(\omega) = 1 + 4\pi N\alpha(\omega) \tag{3.13}$$

and by the one of the wall $\epsilon_2(\omega) = \epsilon(\omega)$, respectively. Here, the density of atoms, N, with the dynamic polarizability $\alpha(\omega)$, is suggested to be very small such that $\epsilon_1 \approx 1$. The sum in the brackets in Eq. (3.11) can be simplified to $\pi N\alpha(i\xi_n)p^{-2}\exp(-2\xi_n pr/c)H(p,\epsilon(i\xi_n))$, where

$$H(p,\epsilon) = \frac{s-p}{s+p} + (1-2p^2)\frac{s-\epsilon p}{s+\epsilon p}, \tag{3.14}$$

$$s = \sqrt{\epsilon - 1 + p^2}. \tag{3.15}$$

The interaction potential between a neutral atom and a dielectric wall (surface), including the retardation effect, is calculated by [Tikochinsky and Spruch, 1993],

$$V_{atom-dielectric}(r) = -\frac{\hbar}{2\pi c^3}\int_0^\infty d\xi_n \xi_n^3 \alpha(i\xi_n)\int_1^\infty dp e^{-2\xi_n pr/c} H(p,\epsilon(i\xi_n)). \tag{3.16}$$

The exponent in the integrand in expression (3.16) is required to be not too large so that $\xi_n \lesssim c/(2rp) \overset{p\geq 1}{\lesssim} c/(2r)$. At very large distances, $r \gg$

$\lambda_{|g\rangle\to|e\rangle}/(2\pi)$, the ratio $c/(2r)$ is much smaller than $\omega_{|g\rangle\to|e\rangle}$, where $\omega_{|g\rangle\to|e\rangle}$ is the corresponding frequency of the atomic dipole transition. At this condition ξ_n also becomes much smaller than $\omega_{|g\rangle\to|e\rangle}$ and the dynamic polarizability and the dielectric constant can be replaced by their static values $\alpha(i\xi_n) = \alpha(0) = \alpha$ and $\epsilon(i\xi_n) = \epsilon(0) = \epsilon$. By using

$$\int_0^\infty d\xi_n\ \xi_n^3 e^{-2\xi_n rp/c} = 6\left(\frac{c}{2rp}\right)^4 \tag{3.17}$$

the pure retarded potential becomes

$$\begin{aligned} V_{atom-dielectric}(r \gg \frac{\lambda_{|g\rangle\to|e\rangle}}{2\pi}) = -\frac{3\hbar c}{8\pi r^4}\alpha \int_1^\infty dp\ \frac{H(p,\epsilon)}{2p^4} = \\ -\frac{C_{4_{a-m}}}{r^4}\ \frac{\epsilon-1}{\epsilon+1}\ \phi(\epsilon) = -\frac{C_{4_{a-d}}}{r^4}. \end{aligned} \tag{3.18}$$

The strength coefficient of the atom-dielectric surface interaction, $C_{4_{a-d}}$, is related to the strength coefficient of the atom-metal surface ($\epsilon \to \infty$) interaction, $C_{4_{a-m}} = 3\hbar c\alpha/(8\pi)$, through

$$\boxed{C_{4_{a-d}} = C_{4_{a-m}}\frac{\epsilon-1}{\epsilon+1}\phi(\epsilon) = \frac{3\hbar c\alpha}{8\pi}\frac{\epsilon-1}{\epsilon+1}\phi(\epsilon).} \tag{3.19}$$

Here,

$$\phi(\epsilon) = \frac{\epsilon+1}{2(\epsilon-1)}\int_0^\infty dp\frac{H(p+1,\epsilon)}{(p+1)^4} \tag{3.20}$$

can be directly calculated to $\phi(\epsilon) = \phi_1(\epsilon+1)/(\epsilon-1)$. The function ϕ_1 is given by the expression (3.8). It is necessary to note, that the equation for the retarded potential Eq. (3.18) is presented in the same form in [Dzyaloshinskii et al., 1961], but it is obtained there using a different method.

Casimir-van der Waals potential In order to simplify the expression (3.16) the interaction potential as a function of the atom-surface distance r is represented by the Casimir-van der Waals potential

$$\boxed{V_{C-vdW}(r) = -\frac{C_4}{r^3(r+l)},} \tag{3.21}$$

where C_4 denotes the potential strength $C_{4_{a-d}}$ or $C_{4_{a-m}}$ and l is the transition length $l = \lambda_{|g\rangle\to|e\rangle}/(2\pi)$. At $r \gg l$ this potential approaches the Casimir potential Eq. (3.7) for the interaction with a conductive surface and the Casimir potential Eq. (3.18) for the interaction with a dielectric surface. At $r \ll l$ the Casimir-van der Waals potential approaches the non-retarded van der Waals potential $V(r) = C_3/r^3$ with the strength coefficient C_3 related to the strength coefficient C_4 by

$$C_3 = \frac{C_4}{l}. \tag{3.22}$$

The Casimir-van der Waals potential parameters C_4 and l can be experimentally obtained by measuring the quantum reflection coefficient versus the incident energy of the atomic beam scattering from a surface. The analysis of experimental data obtained for the system ^{3}He atoms-α-quartz surface and ^{3}He atoms-gold (111)-surface is presented in chapter 4.

An atom between two plates For an atom with the polarizability α situated between two parallel, perfectly conducting walls [Barton, 1987] the interaction potential looks more complicated (the formulas are presented in [Marinescu et al., 1997])

$$V_{metal-atom-metal}(z, L) = T_2(L) - T_1(z, L), \tag{3.23}$$

where

$$T_1(z, L) = \frac{1}{\pi L^3} \int_0^\infty dt \, \frac{t^2 \cosh(2zt/L)}{\sinh(t)} \int_0^{t/\alpha_{fs}L} d\xi \, \alpha(i\xi), \tag{3.24}$$

$$T_2(L) = \frac{\alpha_{fs}^2}{\pi L} \int_0^\infty d\xi \, \xi^2 \alpha(i\xi) \int_{\alpha_{fs}L\xi}^\infty dt \, \frac{e^{-t}}{\sinh(t)}. \tag{3.25}$$

Here, L denotes the distance between the plates, z is the deviation of the atom position from the center of the cavity formed by these two plates and $\alpha_{fs} = 7.29720 \; 10^{-3}$ represents the fine structure constant. The potential shows the asymptotic behavior of pure non-retarded van der Waals and pure retarded Casimir potentials when varying the value of the interval L from zero to large values. At small L the potential is non-retarded

$$V_{metal-atom-metal}(z, \text{small } L) = -\frac{4}{L^3} T(z/L) C_3 \tag{3.26}$$

with

$$C_3 = \frac{1}{4\pi} \int_0^\infty d\omega \, \alpha(i\omega), \tag{3.27}$$

$$T(z/L) = \int_0^\infty dt \, \frac{t^2 \cosh(2tz/L)}{\sinh(t)}. \tag{3.28}$$

At very large L the potential looks like a retarded Casimir potential

$$V_{metal-atom-metal}(z, \text{large } L) = \frac{\pi^3 \alpha}{\alpha_{fs} L^4} \left[\frac{1}{360} - \frac{3 - 2\cos^2(\pi/L)}{8\cos^4(\pi z/L)} \right]. \tag{3.29}$$

3.3 Corrections to the atom-surface interaction potential

Temperature dependence In the general expression for the interaction force between two dielectric bodies Eq. (3.11) the sum can be replaced by an integral over dn for $rkT/(c\hbar) \ll 1$ only in first approximation. More correctly, Euler's summation formula has to be applied [Dzyaloshinskii et al., 1961]

$$\sum_{n=0}^{\infty\prime} f(n) = \int_0^\infty f(n)dn + \frac{1}{12}\frac{df(n)}{dn}\Big|_{n=0} - \frac{1}{30 \cdot 4!}\frac{d^3 f(n)}{dn^3}\Big|_{n=0} + \dots \tag{3.30}$$

Here, $f(n)$ is some function of n. In the case of the interaction between an atom and a conductive surface ($\epsilon \to \infty$) the function $H(p, \epsilon)$ in expression (3.16) takes the value $2p^2$. With the accuracy of the third derivative with respect to n the atom-conductive surface potential can be written as

$$\begin{aligned} V_{atom-metal}(r) = -\frac{k_B T}{c^3} \Bigg(& \frac{\hbar}{2\pi k_B T} \int_0^\infty d\xi_n \, \xi_n^3 e^{-2p\xi_n r/c} \int_1^\infty dp \; 2p^2 + \\ & \frac{1}{2}\left(\frac{2\pi k_B T}{\hbar}\right)^3 \left(\frac{1}{12}\frac{df(n)}{dn}\Big|_{n=0} - \frac{1}{30 \cdot 4!}\frac{d^3 f(n)}{dn^3}\Big|_{n=0} \right) \Bigg), \end{aligned} \tag{3.31}$$

with

$$f(n) = 2n^3 \alpha(i\xi_n) \int_1^\infty dp \, p^2 e^{-2p\xi_n l/c}. \tag{3.32}$$

By calculating $(df(n)/dn)\big|_{n=0} = 0$ and $(d^3 f(n)/dn^3)\big|_{n=0} = -4\alpha$ we obtain the temperature correction of the interaction potential at small values of T

$$\boxed{V_{atom-metal}(r \gg \frac{\lambda_{|g\rangle \to |e\rangle}}{2\pi}) = -\frac{3\hbar c \alpha}{8\pi r^4}\left(1 - \frac{8}{135}\left(\frac{\pi r k_B T}{c\hbar}\right)^4\right).} \tag{3.33}$$

At the atom-surface distance $r = 1\ \mu$m the temperature is relatively small, $T \ll 3000\,$K, i.e. at smaller distances the zero-temperature correction is valid. At room temperature $T \simeq 300\,$K and at $r = 10\,$nm the correction term

$0.059(\pi r k_B T/(c\hbar))^4$ is of the order of 10^{-11} and at the distance $r = 1$ μm it is of the order of 10^{-3}. The deviation of the potential from its zero-temperature approximation reaches 10% at room temperature for an atom-surface distance $r \approx 3$ μm. The experiments discussed in chapter 4 are performed at room temperature. At the distances of the order of 10 nm where quantum reflection occurs the correction term is negligible.

At large values of the temperature the $(n = 0)$-term of the sum in Eq. (3.11) plays the dominant role. Thus, at $T \gg \hbar c/(k_B r)$ the interaction potential between an atom and a metallic surface adopts a different form

$$V_{atom-metal}(r \gg \frac{\lambda_{|g\rangle\to|e\rangle}}{2\pi}) = -\frac{\hbar}{2\pi c^3}\,\frac{\alpha}{2}\,\frac{2\pi k_B T}{\hbar}\,\xi_n^3 \int_1^\infty dp\; 2p^2 e^{-2p\xi_n r/c}. \quad (3.34)$$

The integral in this equation is equal to $4(2\xi_n r/c)^{-3}$. Finally we obtain the expression for the interaction potential at large temperatures

$$\boxed{V_{atom-metal}(r \gg \frac{\lambda_{|g\rangle\to|e\rangle}}{2\pi}) = -\frac{k_B T\alpha}{2r^3}.} \quad (3.35)$$

In order to observe this potential form at the atom-surface distance of 10 μm the temperature has to be much larger than room temperature.

Atom-imperfectly conducting plate [1]

As it is discussed in the previous section, at large atom-surface distances $r \gg \lambda_{|g\rangle\to|e\rangle}/(2\pi)$ the frequency ξ_n greatly exceeds the frequency corresponding to the atom dipole transition. If $\lambda_{|g\rangle\to|e\rangle}/(2\pi)$ has a value of 10 nm (He-atom), the corresponding frequency is $3 \cdot 10^{16}$ Hz. Thus, the frequency ξ_n lies in infra-red or visible parts of the spectrum. The dynamic dielectric constant of the surface is represented in these parts of the spectrum as

$$\epsilon(\omega) \simeq 1 - \frac{\omega_p^2}{\omega^2} = 1 + \frac{\omega_p^2}{\xi_n^2}, \quad (3.36)$$

where $\omega = i\xi_n$, $\omega_p = \sqrt{4\pi N_e e^2/m_e}$ denotes the plasma frequency. N_e is the density of surface free electrons with charge e and mass m_e. Since the surface represents an imperfect conducter, it is clear, that the deviation of the dielectric constant from ∞ is small, i.e. $\xi_n/\omega_p \ll 1$. By placing the expression

[1] The calculations of the correction for imperfection of the conducting surface in the case of interaction between two conductive plates are presented in [Milonni, 1994]

for the surface dielectric constant, Eq. (3.36), into expression (3.14) for the function $H(p, \epsilon(i\xi_n))$ we obtain an approximation of this function

$$H(p, \epsilon(i\xi_n)) \simeq 2p^2 - 2(3p - p^{-1})\frac{\xi_n}{\omega_p}. \tag{3.37}$$

This approximation is expected because $H = 2p^2$ is the value of the function H for a perfectly conducting surface and the correction term is of the order of the small value ξ_n/ω_p.

The interaction potential between a neutral atom and an imperfectly conducting surface can be expressed by

$$\begin{aligned} &V_{\substack{atom-metall \\ (\epsilon\approx\infty)}}(r) = V_{\substack{atom-metall \\ (\epsilon=\infty)}}(r) + \\ &\frac{\hbar}{\pi c^3 \omega_p}\int_0^\infty d\xi_n\, \xi_n^4 \alpha(i\xi_n) e^{-2\xi_n rp/c} \int_1^\infty dp\, (3p - p^{-1}) \overset{r \gg \frac{\lambda_{|g\rangle\to|e\rangle}}{2\pi}}{=} \\ &-\frac{3\hbar c\alpha}{8\pi r^4}\left(1 - \frac{8c}{5\omega_p r}\right). \end{aligned} \tag{3.38}$$

For a gold (Au) surface the free electron density is given by $N_e = 5.90\ 10^{22}\,\mathrm{cm}^{-3}$ [Ashcroft and Mermin, 2001], the corresponding plasma frequency is equal to $\omega_p = 1.37\ 10^{16}\,\mathrm{Hz}$ and the correction term has the form $8c/(5\omega_p r) = 3.5\ 10^{-8}/r$, where r has to be expressed in meter. At the distance $r = 100\,\mathrm{nm}$ the value of the correction term is 0.35 and the value of the interaction potential at this distance is only 75% of the value of the potential in the case of the perfectly conducting surface. From these calculations we conclude that it is very important to check the validity of the expression for the pure retarded Casimir potential for a certain atom-surface distance.

It is more interesting to calculate the correction of the non-ideal conductivity at small distances, $r \ll \lambda_{|g\rangle\to|e\rangle}/(2\pi)$. In this case we obtain the attractive interaction potential by assuming $\xi_n r/c \ll 1$ in the form

$$V_{\substack{atom-metall \\ (\epsilon\approx\infty)}}(r \ll \frac{\lambda_{|g\rangle\to|e\rangle}}{2\pi}) = -\frac{\hbar}{4\pi r^3}\int_0^\infty d\xi_n\, \alpha(i\xi_n) + \frac{3\hbar}{4\pi\omega_p c r^2}\int_0^\infty d\xi_n\, \xi_n^2 \alpha(i\xi_n). \tag{3.39}$$

Two inequalities, $r \ll \lambda_{|g\rangle\to|e\rangle}/(2\pi)$ and $\xi_n r/c \ll 1$, allow to assume that ξ_n is of order of the frequency of the first electric dipole transition, $i\xi_n \sim \omega_{|g\rangle\to|e\rangle}$. Thus, Eq. (3.39) can be approximated by the expression

$$\boxed{V_{\substack{atom-metall \\ (\epsilon\approx\infty)}}(r \ll \frac{\lambda_{|g\rangle\to|e\rangle}}{2\pi}) = -\frac{C_3}{r^3}\left(1 + \frac{3cr}{\omega_p}\left(\frac{\lambda_{|g\rangle\to|e\rangle}}{2\pi}\right)^{-2}\right).} \tag{3.40}$$

The value for the van der Waals attractive potential strength C_3 is calculated to be

$$\boxed{C_3 = \frac{\hbar}{4\pi} \int_0^\infty d\xi_n \, \alpha(i\xi_n).} \tag{3.41}$$

With an accuracy of $\hbar$ this expression coincides with Eq. (3.4), in which ω plays the role of ξ_n. Due to the quantum-mechanical character of the van der Waals force the strength coefficient has to be proportional to Planck's constant $\hbar$. Therefore expression (3.41) is correct.

Besides the contribution of short-range interactions, the correction given by Eq. (3.40) leads to different values of the potential depth in the interaction of an atom with different conductive surfaces. This correction is taken into account in the analysis of the ^{3}He-gold surface interaction in chapter 4.

Determination of the van der Waals potential strength A one-dimensional total interaction potential between an atom and a surface is often represented in the form of the Lennard-Jones potential (LJ(n,m)),

$$V(r) = V_0 \cdot \frac{m}{n-m} \cdot \left[\left(\frac{a}{r}\right)^n - \frac{n}{m} \left(\frac{a}{r}\right)^m \right]. \tag{3.42}$$

Here, n and m denote the power of the repulsive and attractive parts of the potential, respectively, and $V_0 = V(a)$ is the value of the potential minimum, which is situated at the distance a from the surface. The first term in Eq. (3.42) denotes the short-range repulsive part of the potential. This repulsive force appears at small distances because of the overlap of the electrons of the incident atom with the electrons of the surface atoms. The second term in Eq. (3.42) is the long-range attractive part of the interaction potential, which is discussed above in detail. By rewriting Eq. (3.42) in the form

$$V(r) = \frac{C_n}{r^n} - \frac{C_m}{r^m}, \tag{3.43}$$

where C_n and C_m are the strength coefficients of the repulsive and attractive potential parts, respectively, one can see that the effect of retardation is not taken into account. By correcting this, the attractive term takes the form $C_{m+1} r^{-m}/(r+l)$. Then the LJ(n,m)-potential is given by the more complicated form

$$V(r) = V_0 \cdot \frac{f_m}{f_n - f_m} \cdot \left[\left(\frac{a}{r}\right)^n - \frac{f_n}{f_m} \cdot \frac{(1+\frac{a}{l})}{(1+\frac{r}{l})} \cdot \left(\frac{a}{r}\right)^m \right]. \tag{3.44}$$

For simplicity, we write $f_n = n(1 + a/l)$ and $f_m = m + a(m + 1)/l$. By assuming that the retardation effect plays a role only very far from the surface, Eq. (3.44) approaches Eq. (3.42). The representation of the interaction potential by Eq. (3.42) is not false, because in classical scattering problems only the potential form near the surface is important. However, equation (3.44) is more exact without any approximations. From Eq. (3.44) does not follow that the strength coefficients C_n and C_m depend on the transition length l, but that the value V_0 of the potential depth depends on l. The attractive part of the potential can be written either through the potential strength C_{m+1} or through the value of the potential minimum V_0,

$$V_{attr}(r) = -\frac{C_{m+1}}{(r+l)r^m} = -V_0 \cdot \frac{f_n}{f_n - f_m} \cdot \frac{(1+\frac{a}{l})}{(1+\frac{r}{l})} \cdot \left(\frac{a}{r}\right)^m . \tag{3.45}$$

By taking into consideration that the van der Waals interaction between a neutral atom and the surface of a solid has the power $m = 3$, the van der Waals potential strength $C_3 = C_4/l$ can be calculated from Eq. (3.45),

$$\boxed{C_3 = V_0 a^3 \left(1 + \frac{a}{l}\right) \frac{n}{n - 3 - \frac{1}{1+l/a}}.} \tag{3.46}$$

This formula will be used for the analysis of the ^{3}He-α-quartz and the ^{3}He-gold systems in chapter 4 for comparing the potential parameters with literature values.

3.4 Surface roughness and disorder

3.4.1 Stepped surface with large terraces

In this section instead of a flat (or atomically rough) surface we consider a microscopically disordered surface. The surface consists of many steps of different height perpendicular to the surface, separated by large terraces which are only atomically rough (see Fig. 3.3). The height of the steps is distributed according to a Gaussian function. By setting the most probable z-coordinate of all terraces as $z = 0$,

$$n(\Delta_n) = \frac{1}{\sqrt{2\pi}\sigma} \exp\left(-\frac{\Delta_n^2}{2\sigma^2}\right) \tag{3.47}$$

terraces have the coordinate $z = \pm\Delta_n$, where σ, the Gaussian width, is the root mean square of the z-distribution of the terraces.

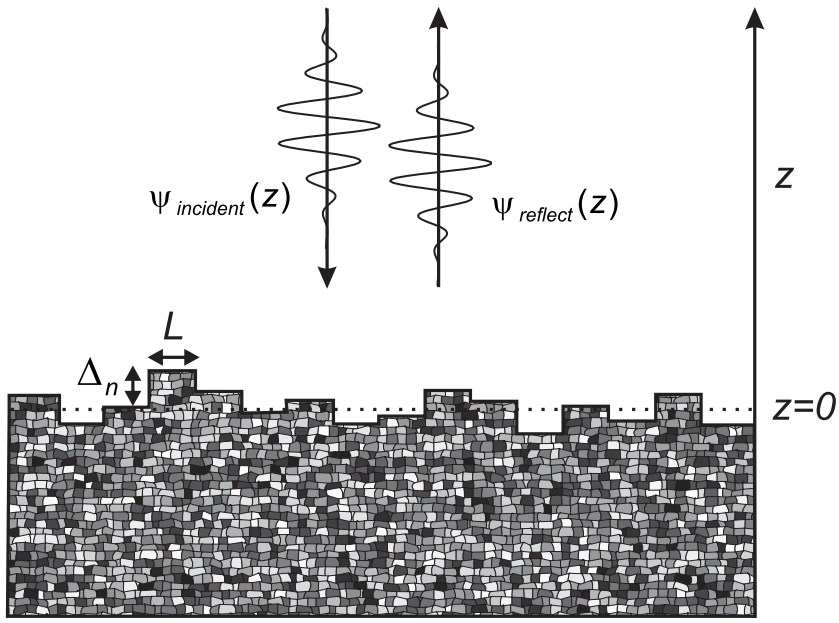

Figure 3.3: Schematic illustration of a crystal with disordered surface. The stepped surface with Gaussian distribution of the step heights of the width Δ_n centered at $\Delta_n = 0$. The steps are separated by terraces with large length L. The incident and reflected waves are assumed to be dependent only on the coordinate z perpendicular to the suface.

Dephasing of the wave packet Firstly we consider only the motion of the impinging wave perpendicular to the surface. The fact that the wave incides onto the surface under the angle θ_i with respect to the surface normal is taken into account by the value of the de Broglie wavelength perpendicular to the surface, $\lambda_{dB_\perp} = \lambda_{dB}/\cos\theta_i$. We assume that $\lambda_{dB_\perp}$ is comparable or smaller than the maximal height of the surface steps. In this case we must take into account that the wave is reflected incoherently from all terraces. To calculate the reflection coefficient of coherent scattering we must represent the reflected wave function from the stepped surface as a sum of the reflected wave functions from all terraces with different phases. At de Broglie wavelengths parallel to the surface $\lambda_{dB_{||}} \approx \lambda_{dB}$ much smaller than the average terrace length L in beam direction, the wave-terrace interaction is approximately equal to the wave-smooth surface interaction. The wave function of the wave reflected from the terrace with the coordinate $-\Delta_n$ and detected far from the surface has the form

$$\Psi_{refl_n}(z, k_0, t) = \exp\left(ik_0(z + 2\Delta_n) - i\frac{\hbar k_0^2}{2m}t\right). \tag{3.48}$$

The wave function of the wave reflected from the stepped surface is given by

$$\Psi_{refl}(z, k_0, t) = \sum_n n(\Delta_n)\Psi_{refl_n}(z, k_0, t). \tag{3.49}$$

The incident wave (or the atomic beam) illuminates a large number of terraces. Thus, the sum over n can be replaced by the integral over Δ_n from the minimum z-coordinate, $-\Delta_{n_{max}}$, to the maximum one, $\Delta_{n_{max}}$. If $n(\Delta_{n_{max}}) \ll n(0)$, the integral can be written as the integral from $-\infty$ to $+\infty$. The wave function of the wave packet detected far from the surface is equal to

$$\Psi_{refl}(z, t) = \int_{k_{0_{min}}}^{k_{0_{max}}} dk_0\ c(k_0) \int_{-\infty}^{\infty} d\Delta_n\ n(\Delta_n)\Psi_{refl_n}(z, k_0, t), \tag{3.50}$$

where $c(k_0)$ is the initial wave number distribution of the atomic beam. Taking into account that $\int_{-\infty}^{\infty} d\Delta_n\ \exp(2ik_0\Delta_n - \Delta_n^2/(2\sigma^2)) = \sqrt{2\pi}\ \sigma$ we obtain

$$\Psi_{refl}(z, t) = \int_{k_{0_{min}}}^{k_{0_{max}}} dk_0\ c(k_0) \exp\left(ik_0 z - i\frac{\hbar k_0^2}{2m}t - 2\sigma^2 k_0^2\right). \tag{3.51}$$

The term $\exp(-2\sigma^2\langle k_0\rangle^2) = \exp(-2\sigma^2(2\pi)^2/\langle\lambda_{dB_\perp}\rangle^2)$ describes the effect of dephasing of the wave function reflected from the stepped surface with large terraces with respect to the wave reflected from a smooth surface.

The reflection coefficient of the wave paket from the stepped surface at the average wave number $\langle k_0\rangle$, $|R_{stepped}(\langle k_0\rangle)|^2$, is calculated to be

$$|R_{stepped}(\langle k_0\rangle)|^2 = |R_{smooth}(\langle k_0\rangle)|^2 \exp(-4\sigma^2\langle k_0\rangle^2), \tag{3.52}$$

where $|R_{smooth}(\langle k_0\rangle)|^2$ denotes the reflection coefficient from the smooth surface, which has the coordinate $z = 0$. At $\langle\lambda_{dB_\perp}\rangle$ much larger than σ the exponent, $\exp(-4\sigma^2\langle k_0\rangle^2)$, approaches unity and the incident wave "does not see" the surface disorder. The reflection coefficient is given by the one from the smooth surface. At $\langle\lambda_{dB_\perp}\rangle$ comparable or smaller than σ the effect of the dephasing becomes more significant which leads to the reduction of the reflected beam intensity.

Losses from steps At scattering from a stepped surface not only the dephasing of the wave function leads to a drop of the reflection coefficient. At large incident angles the interaction of the incident wave with the steps becomes non-negligible. This effect depends on the incident angle of the atomic beam and on the geometric dimensions of the terraces and

steps. Qualitatively, the part of the wave, which meets a step with a height $h > L\tan(90^\circ - \theta_i)$ from the side will be lost for the specular beam.

Since the atomic beam illuminates a large number of surface terraces and steps, the probability that a step has the height h, $n(h)$, is equal to $n(\Delta_n)$ (Eq. (3.47)). In terms of the angle $\theta = \arctan(h/L)$ the probability for the wave inciding under the angle $\theta_i = 90^\circ - \theta$ to meet the step with the height h is given by

$$n(\theta) = \frac{1}{\sqrt{2\pi}\sigma} \exp\left(-\frac{\tan^2\theta}{2(\sigma/L)^2}\right). \tag{3.53}$$

Qualitatively speaking, all steps having the height $h = L\tan\theta$ with the probability $n(\theta < 90^\circ - \theta_i)$ do not contribute to the loss of the wave function. Their number, $f(\theta_i)$, is given by

$$f(\theta_i) = \frac{\int_0^{90^\circ-\theta_i} d\theta \ \exp\left(-\frac{\tan^2\theta}{2(\sigma/L)^2}\right)}{\int_0^{90^\circ} d\theta \ \exp\left(-\frac{\tan^2\theta}{2(\sigma/L)^2}\right)}. \tag{3.54}$$

At grazing incidence of the atomic beam one can approximate $\theta \approx \tan\theta$ and therefore

$$f(\theta_i) \approx \frac{1}{\sqrt{2\pi}(\sigma/L)} \int_0^{90^\circ-\theta_i} d\theta \ \exp\left(-\frac{\tan^2\theta}{2(\sigma/L)^2}\right). \tag{3.55}$$

The final form for the reflection coefficient from a stepped surface is given by

$$\boxed{|R_{stepped}(\langle k_0\rangle)|^2 = |R_{smooth}(\langle k_0\rangle)|^2 \exp(-4\sigma^2\langle k_0\rangle^2)\ f(\theta_i).} \tag{3.56}$$

The factor $f(\theta_i)$ becomes more significant at increasing incident angle θ_i and leads to a reduction of the reflected beam intensity at grazing beam incidence, playing no role at relatively small incident angles.

It is important to note that the measured reflection coefficient from a surface, which is described above, satisfies Eq. (3.56) only if the transfer width exceeds the average terrace length significantly. Only in this case the Gaussian distribution of the step heights can be used in the calculations. The correction (3.56) is used for the data analysis of the ^{3}He-α-quartz system in chapter 4 (see Fig. 4.14).

3.4.2 Surface roughness

One of the most interesting applications of measuring the attractive long-range atom-surface potential by means of quantum reflection is studying the surface roughness. As discussed in the previous section the information about a microscopic surface disorder can be extracted from the behavior of the reflection coefficient. Not only the microscopic disorder but also atomic surface rougness can change the value of the interaction potential and therefore the value of the measured quantum reflection coefficient. The influence of the atomic surface roughness on the interaction potential between macroscopic bodies is investigated for a few systems. For instance, this influence on the interaction between a rough surface and a dielectric sphere is precisely measured by [Mohideen and Roy, 1998]. The experimental data are in very good agreement with the theoretically predicted values [Klimchitskaya et al., 1999] for the function describing the roughness, obtained from a separate AFM measurement. Reflection of an atom from the evanescent wave mirror in the case of a rough prism surface is investigated in [Henkel et al., 1997].

In [Maradudin and Mazur, 1980, Mazur and Maradudin, 1981] the correction of the van der Waals potential between two planes separated by the distance l is calculated in the cases when one of the interacting surfaces or both surfaces are atomically rough. The resulting van der Waals force per unit area between a flat and an atomically rough surface is obtained to be

$$F(l) = -\frac{C_3}{l^3} - \frac{\delta^2}{a^2}\left[\frac{C_4}{l^4} + \frac{C_5}{l^5} + \dots\right] + O\left(\frac{\delta^4}{a^4}\right). \tag{3.57}$$

Here, a denotes the transverse correlation length, i.e. the mean distance between consecutive peaks on the rough surface. The length parameter δ represents the root-mean-square deviation of the surface from flatness. The parameters C_3, C_4 and C_5 denote the van der Waals force coefficients of a flat surface and similar coefficients dependent on the dynamic dielectric surface constants. In the case that the interacting surfaces are identical with dynamical dielectric constants satisfying Eq. (3.36) the corrected van der Waals force per unit area is given by

$$F(l) = -\hbar\omega_p\left[\frac{0.7810\ 10^{-2}}{l^3} + \frac{\delta^2}{a^2}\left(\frac{0.05597\,a}{l^4} + \frac{0.03245\,a^2}{l^5} + O(l^{-6})\right) + O\left(\frac{\delta^4}{a^4}\right)\right]. \tag{3.58}$$

The typical value of δ/a is of the order of 0.1. Thus, at the separation of the surfaces by the distance $l = a$ the correction of the van der Waals force due to the surface roughness is expected to be of the order of 10%. At larger separations the correction decreases significantly.

As far as we know only one theoretical work [Bezerra et al., 2000] is devoted to the correction of the interaction potential between a neutral atom and a surface. This correction is calculated for the Casimir potential and is valid only for atom-surface distances much larger than the dipole transition length of the atom. The Casimir potential corrected to the surface roughness is obtained with the accuracy up to fourth order of the roughness amplitude for the case that the surface roughness is a periodic function. Here, we give this expression only up to the second correcting term

$$V(x_A, y_A, r) = V(r)\left(1 + h_1(x_A, y_A, r)\frac{A}{r} + h_2(x_A, y_A, r)\frac{A^2}{r^2}\right), \qquad (3.59)$$

where $V(r)$ represents the Casimir potential between the atom and the flat surface, x_A and y_A are the coordinates of the incident atom in the plane of the flat surface, r denotes the atom-surface distance and A represents the surface roughness amplitude. The expansion coefficients $h_1(x_A, y_A, r)$ and $h_2(x_A, y_A, r)$ are some complex functions dependent on the Fourier-coefficients of the periodic surface roughness function (see [Bezerra et al., 2000]). For large-scale roughness when the transverse correlation length is much larger than the atom-surface distance the correction is obtained to be proportional to the roughness amplitude A. For small-scale roughness ($a \ll r$) only the correction term with squared amplitude plays a role, which coincides with the results of [Maradudin and Mazur, 1980]. It is calculated in [Bezerra et al., 2000] that at large-scale roughness the correcting term can give a contribution of order of ten percent to the Casimir potential, while the short-scale roughness gives a contribution of the order of some percent of the net interaction energy.

It is clear that at smaller atom-surface distances the influence of the surface roughness on the interaction potential is much larger than on the Casimir potential. The deviation of the measured attractive potential from the predicted one for a flat surface opens the possibility to investigate not only the scale of the atomic roughness but also the parameters of the surface roughness function. It is necessary, however, to calculate the correction term in the case of the Casimir-van der Waals potential, or at least, in the case of the van der Waals potential, which is valid at much smaller atom-surface distances, where the surface roughness correction is predominant.

Chapter 4

Experimental observation of quantum reflection and Casimir effect

A number of experiments have been performed with the goal of observing the purely non-classical phenomenon of quantum reflection. In the experiments reported on in [Doyle et al., 1991, Yu et al., 1993, Berkhout et al., 1989], quantum reflection was observed indirectly by studying the behavior of the sticking coefficient at low energies of the incident atom (see chapter 2). Direct measurements of quantum reflection were performed by [Nayak et al., 1983, Shimizu, 2001]. However, the data in [Nayak et al., 1983] are not unambiguously interpreted. The experiment of [Shimizu, 2001] represents the first direct observation of quantum reflection. These experimental data are well-described by the recently developed theory of quantum reflection by Friedrich and Côté [Friedrich et al., 2002, Côté et al., 1997] (see Sec. 4.4).

In this chapter we present an experiment for directly observing quantum reflection exclusively from the attractive interaction potential (Sec. 4.1). In contrast to the experiment of [Shimizu, 2001] performed close to the low-energy limit, our experiment includes the energy range up to the high-energy asymptote [Druzhinina and DeKieviet, 2002]. The data are analyzed taking into account all relevant experimental details (Sec. 4.2). In the frame of the theory by Friedrich *et al.* our experimental data are fully explained (Sec. 4.3). Moreover, quantum reflection measurements are utilized for quantitatively characterizing the Casimir effect in the system atom-surface for the first time (Sec. 4.3) [Druzhinina et al., 2003].

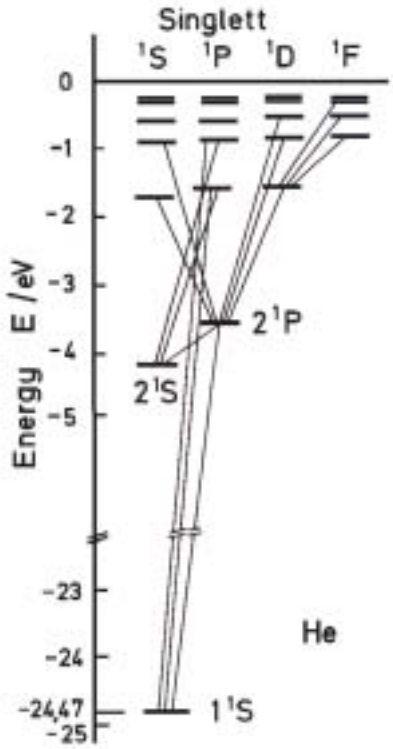

Figure 4.1: The electronic structure of the helium atom in the singlet state, adapted from [Haken and Wolf, 1993].

4.1 Experimental setup

The experimental data on quantum reflection discussed in this chapter are obtained using the ^{3}He atomic beam spectrometer [DeKieviet et al., 1995]. Since this work focuses on the theoretical interpretation of the experimental data, the experimental setup is described only schematically in this section. For more detailed information about the apparatus and the spin echo method the reader is referred to [Schmidt, 1996, Hafner, 1999]. However, some parts of the setup that are particularly important for the experiments on quantum reflection are discussed in more detail in the next section.

4.1.1 The ^{3}He-atom

The scattering of a ^{3}He atomic beam is a powerful instrument for studying the surface of a solid. Because of the Pauli-principle, the ^{3}He-atom is reflected

from the surface at some Å above the top layer of surface atoms. Thus, in contrast to neutron, electron or X-ray-beams the helium atomic beam does not penetrate into the surface. The de Broglie wavelength of the beam is on the order of some Å, which is comparable with the lattice constant of a solid body. Therefore, coherent elastic (or quasi-elastic) scattering of a ^{3}He atomic beam is a well suited method for studying the surface structure. By using the spin echo method dynamical processes on the surface can be investigated on the nano- and even pico-second time-scale with an energy resolution in the neV-range. The ^{3}He-atom is chosen because of its extreme surface sensitivity and also because it has a nuclear spin $I = 1/2$. Due to the strong shielding of the nuclear spin by the closed electron shell the nuclear spin direction remains unchanged during the interaction with the surface. This is a necessary condition for the applicability of the spin echo method for surface analysis.

^{3}He atomic beam scattering has additional advantages concerning the measurement of quantum reflection:

- ^{3}He is one of the lightest atoms. Since $\rho \propto \sqrt{m}$ (see Eq. (2.81)) a light atom is more likely to be quantum reflected than a heavy one. Therefore, the effect of quantum reflection of ^{3}He-atoms can be measured even at relatively high incident kinetic energies perpendicular to the surface.

- Due to the small static polarizability of a ^{3}He-atom in its ground state, α, the attractive atom-surface interaction potential is particularly weak, $C_4 \propto \alpha$. Due to the ($|R|^2 \propto \exp(-\sqrt{\beta_4}) = \exp(-C_4^{1/4})$)-scaling at low energies (see Eq. (2.83)) the effect of quantum reflection is more pronounced than it is for instance for a metastable Ne-atom.

- The ^{3}He atomic beam is extremely sensitive to the surface disorder. In the case of high surface roughness on the atomic scale or in the case of surface contamination the atomic beam is reflected diffusively, not contributing to the specular peak. This property of the atomic beam is used for suppressing the reflection from the repulsive potential wall in order to measure pure quantum reflection from the attractive part of the potential.

Here, we give some important values for the ^{3}He-atom.

Magnetic moment The magnetic moment of the ^{3}He-atom, μ, is given by

$$\mu = g\mu_n, \tag{4.1}$$

m [kg]	μ [neV/T]	α [Å^3]	$\lambda_{\lvert g\rangle\to\lvert e\rangle}/(2\pi)$ [Å]
$5.00824\,10^{-27}$	-67	0.207	93

Table 4.1: The relevant properties of the ^{3}He-atom: atomic mass m, magnetic moment μ, static polarizability α and the normalized wavelength of the lowest-energy electric dipole transition $\lambda_{|g\rangle\to|e\rangle}/(2\pi)$.

where the g-factor for ^{3}He-atoms is equal to -2.127624 and the nuclear magneton μ_n is given by $\mu_n = \mu_B m_e/m_p = e\hbar/(2m_e)\cdot m_e/m_p$ with $m_e = 9.10956\ 10^{-31}$ kg, $m_p = 1.6726\ 10^{-27}$ kg and $\mu_B = 9.2741\ 10^{-24}\,\mathrm{JT}^{-1}$ denote electron mass, proton mass and the Bohr magneton, respectively. Thus, the magnetic moment of ^{3}He-atom is equal to $\mu = -67\,\mathrm{neV/T}$.

Static polarizability The static polarizability of a ^{3}He-atom can be calculated from the measured value of the dielectric susceptibility χ of a ^{3}He gas. This gas is assumed to be ideal with the atomic density N and the pressure $P_0 = Nk_BT$. The polarization, P, is related to the refractive index, n, by

$$n^2 = 1 + \frac{P}{\epsilon_0 E}, \tag{4.2}$$

where E is the electric field and $\epsilon_0 = 8.85\ 10^{-12}\,\mathrm{C^2m^{-1}}$ is the vacuum permittivity. The refractive index is given by the ratio of the speed of light c and the phase velocity of radiation v_p [Jones, 2000],

$$n = \frac{c}{v_p} = \frac{(\epsilon_0\mu_0)^{-\frac{1}{2}}}{(\epsilon\mu_0)^{-\frac{1}{2}}} = \sqrt{\frac{\epsilon}{\epsilon_0}}. \tag{4.3}$$

Here, ϵ is the permittivity of the atomic gas. The dielectric susceptibility χ is defined through the permittivity as $\epsilon = \epsilon_0(1+\chi)$. Taking into account that the polarization P is connected to the atomic polarizability α by $P = N\alpha E$, we obtain from all these formulas

$$\alpha = \frac{\epsilon_0\chi}{N} = \epsilon_0\frac{k_BT}{P_0}\chi. \tag{4.4}$$

Using the value of $\chi = 6.49\ 10^{-5}$, given in [Tab, 1980] for the atmospheric pressure $P_0 = 101\,\mathrm{kPa}$ and the room temperature $T = 293\,\mathrm{K}$, we obtain the value for the static polarizability of a ^{3}He-atom $\alpha = 2.3\ 10^{-41}\,\mathrm{Fm^2}$. In order to give this value in terms of Å^3 we have to multiply it by the factor $1/(4\pi\epsilon_0) = 8.99\ 10^9\,(\mathrm{Fm})^{-1}$. Thus, we obtain $\alpha = 0.207\,\text{Å}^3$. The value of $\alpha = 0.20\,\text{Å}^3$ is given in [Israelachvili, 1985] for a He-atom.

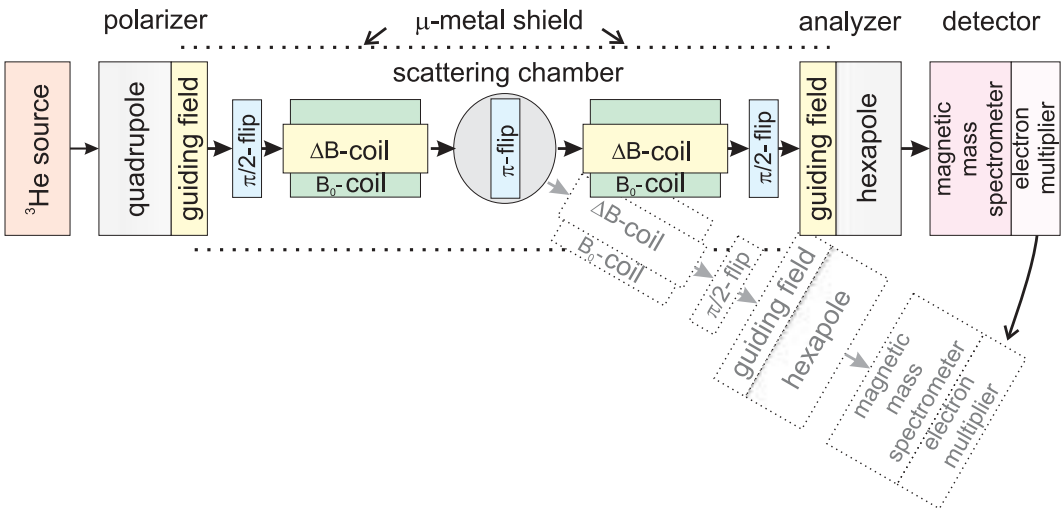

Figure 4.2: Schematic overview of the ^{3}He atomic spectrometer, adapted from [Teichert, 1999].

Wavelength of the lowest-energy electric dipole transition The lowest-energy electric dipole transition in the He-atom is the 1^1S$\rightarrow$ 2^1P-transition in the singlet system (see the level-scheme in Fig. 4.1 from [Haken and Wolf, 1993]. The energy of this transition is listed in the Atomic Energy Levels Data Base of [NIST, 1999], $\Delta E = 171135\,\mathrm{cm}^{-1}$=21.218 eV. The corresponding wavelength is given by $\lambda_{|g\rangle\rightarrow|e\rangle} = 58.43\,\mathrm{nm}$, from which we calculate the normalized wavelength $\lambda_{|g\rangle\rightarrow|e\rangle}/(2\pi) = 93\,\text{Å}$.

Table 4.1 summarizes the relevant atomic properties of the ^{3}He-atom.

4.1.2 Preparation of the atomic beam

Beam source ^{3}He gas is transferred through a capillary from a storage tank to a nozzle. The capillary is conducted through a ^{4}He bath cryostat, where the gas is cooled down to 4.2 K. By extracting the vapor from the ^{4}He bath, the temperature of the ^{3}He gas can be decreased down to 1.3 K. The cooled gas expands with supersonic velocity through the nozzle with the diameter of 500 μm into the vacuum undergoing a pressure difference from 10 mbar to 10^{-5} mbar (at a flux of 40 sccm=1.8 10^{19} atoms per second). The atomic beam is formed by two appertures: A skimmer and a collimator with diameters 1.5 mm and 2.0 mm, which are situated at the distances of 20 mm and 85 mm from the nozzle, respectively. Behind these appertures only 10^{-5} of the initial number of atoms leaving the nozzle remain in the beam.

Wavelength distribution The beam, cooled down to 4.2 K has an average de Broglie wavelength of 5.7 Å and a full width at half maximum (FWHM) of the wavelength distribution of about 20%. The average de Broglie wavelength and the width of the distribution (FWHM) for a 1.3 K atomic beam are 9.0 Å and 15%, respectively.

Attenuation of the beam Since the detector has a saturation rate of 2 MHz, it is necessary to attenuate down to this rate the beam intensity, which is to be detected. In order to do this so-called flags can be inserted into the beam. The first flag transmits about 10% of the helium beam intensity, and the second one about 2%. In addition, a chopper can be inserted into the beam behind the flags. The beam is chopped by this rotating chopper wheel into small bunches. This opens the possibility to perform time of flight spectroscopy. Since the chopper has a transmission factor of 1/32, it also attenuates the beam intensity. When both flags and the chopper are in the beam only 2.2 10^{-4} of the beam intensity in front of the flags reaches the detector.

4.1.3 Polarizer

Beam polarization The ^{3}He atomic beam is polarized by means of a quadrupole electro-magnet with a maximal magnetic field of 1.2 T. As in the Stern-Gerlach experiment one spin component with respect to the beam axis is focused, the other one is defocused. The atoms of the latter spin component are blocked. The separation of both spin components is more effective for a slow atomic beam. In order to globalize the locally separated spin component the spins are coupled adiabatically in a permanent magnet, the so-called guiding field. The direction of this field, which is perpendicular to the beam axis, defines the direction of the polarization of the beam.

Wavelength distribution at the surface The wavelength distribution of the atomic beam when reaching the probed surface depends not only on the initial wavelength distribution behind the source. The focusing properties of the polarizer influence the wavelength distribution at the surface significantly. By means of filter bands, which are fixed in the polarizer and analyzer, the wavelength distribution can be optimized. After the adjustment of the polarizer the average de Broglie wavelength takes a value between 5 and 9 Å for an initial 4.2 K-atomic beam and the FWHM of the wavelength distribution lies between 15 and 40%.

4.1.4 Spin echo coils

The ^{3}He atoms polarized perpendicularly to the beam axis propagate into the first spin echo coil of the length of 520 mm. This coil creates a magnetic field parallel to the beam axis. The change in orientation of the magnetic field from perpendicular (guiding field) to parallel to the beam axis (spin echo coil) causes the atomic spins to flip by $\pi/2$. In order to realize the spin flip the transition from one magnetic field to the other must be non-adiabatic. The second spin echo coil is situated behind the first one and is constructed completely identically. Only the direction of the magnetic field in this coil is opposite to the direction of the magnetic field of the first one. This corresponds to a π-flip in the region between these coils. More details on the spin echo coils can be found in [Schmidt, 1996].

4.1.5 Preparation and scattering chambers

The non-magnetic UHV scattering chamber is situated between the two spin echo coils. The preparation chamber is built on top of it. The target is mounted on the cooling finger of a liquid-helium cryostat which has two functions: To cool the target and to manipulate the target position [Reetz-Lamour, 2001]. In the preparation chamber the surface is prepared and subsequently lowered down into the scattering chamber for the following experiment. The special construction of the scattering chamber and its connections with the tubes containing the spin echo coils allow to rotate this chamber by an angle of up to 45°. The detector arm of the apparatus can be rotated around the scattering chamber by up to 90° with respect to the beam axis without vacuum losses. Thus, scattering angles between 90° and 180° can be scanned continuously.

4.1.6 Analyzer

The analyzer situated behind the second spin echo coil consists of a guiding field and a hexapole magnet with a magnetic field of 0.6-0.8 T. Between the second spin echo coil and the guiding field occurs a second $\pi/2$-flip. After that one of two spin components (in dependence on the polarity of the guiding field) is adiabatically transferred into the hexapole magnet, where this separated component is focused into the detector. The apertures on the front and back side of the analyzer have an inner diameter of 6 and 3 mm, respectively.

4.1.7 Detector

The detector consists of a mass spectrometer and an electron multiplier. The atoms with separated spin component, which are focused by the analyzer into the detector, are ionized by collisions with an electron beam superimposed onto the atomic beam. In the last sector magnet the accelerated ions are deflected into the electron multiplier according to the ratio e/m. The pulse rate in the detector reflects the rate of incident ^{3}He atoms. The number of atoms with spin up (in the direction of the initial polarization), $N_\uparrow$, and the one with spin down (in the opposite direction), $N_\downarrow$, are measured separatelly by switching the polarity of the guiding field of the analyzer. The polarization of the atomic beam is given by

$$P = \frac{N_\uparrow - N_\downarrow}{N_\uparrow + N_\downarrow}. \tag{4.5}$$

4.1.8 Angular resolution of the ^{3}He spectrometer

The full width at half maximum of the direct beam profile determines the angular resolution of the ^{3}He spectrometer to $\Delta\Theta_f = 3.5\,\mathrm{mrad}$. This value is defined by the beam divergence from the exit aperture of the polarizer to the enterance aperture of the analyzer. The transfer width ω depends on the instrumental resolution $\Delta\Theta_f$, $\omega = \lambda_{dB}/(\Delta\Theta_f \cos\theta_f)$ [Comsa, 1979], where λ_{dB} denotes the average de Broglie wavelength and θ_f is the angle of the reflected beam with respect to the surface normal. The transfer width corresponds to a linear scale in the plane of the surface on which information about the surface percularities are directly measured. Therefore, this value is also named the coherence length. A small angular resolution and thus the large value of the coherence length are some of the advantages of the ^{3}He spectrometer.

4.2 Data analysis

4.2.1 Wavelength distribution from spin rotation or spin echo curve

In this work we only give a short introduction into the spin echo principle. For the measurement of quantum reflection this method is useful only for the direct and exact determination of the distribution of the de Broglie wavelengths in our polychromatic atomic beam. We restrict ourselves to the

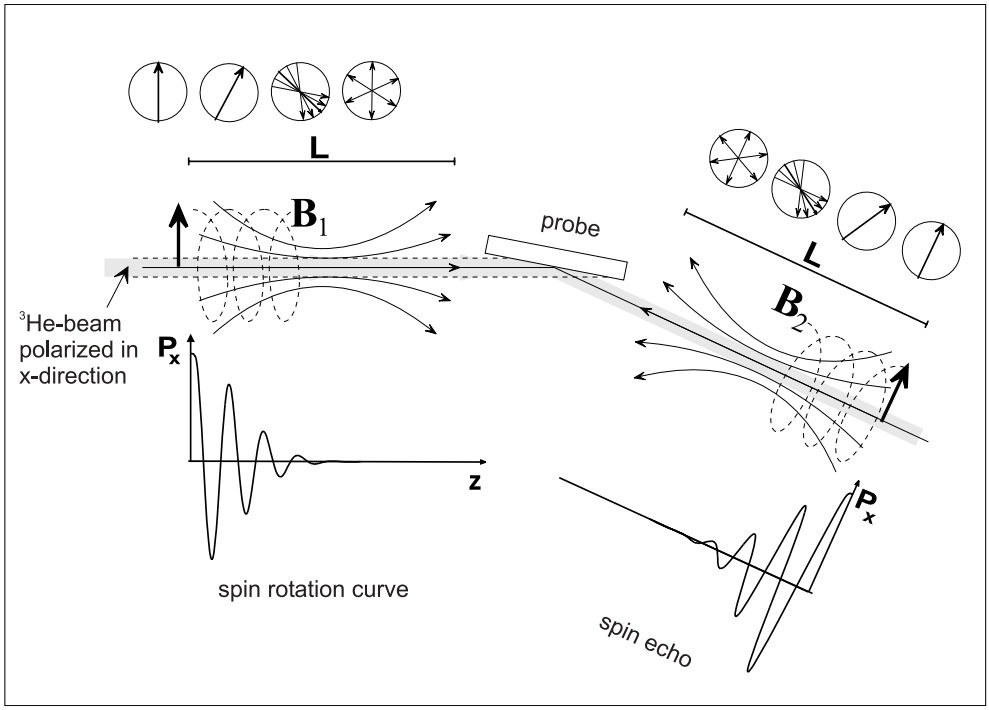

Figure 4.3: Semi-classical representation of the spin echo method, adapted from [Schmidt, 1996].

semi-classical representation of the spin echo method. More detailed and profound descriptions are found in [Schmidt, 1996, Hafner, 1999].

A ^{3}He-atom, which is polarized perpendicularly to the beam axis, propagates with the velocity v into the magnetic field of the first spin echo coil oriented parallel to the beam axis. The spin with magnetic moment μ precesses around the z-axis of the magnetic field $B(z)$ with the Larmor frequency $\omega_L = 2\mu B(z)/\hbar = \gamma B(z)$, where $\gamma = -2\pi \cdot 32.334$ MHz T^{-1} denotes the gyromagnetic ratio for ^{3}He atoms. Behind the magnetic field the spin has picked up an additional precession phase $\phi = \int_0^L dz\ \gamma B(z)/v = \gamma \bar{B} L/v$, where $\bar{B}$ is the magnetic field averaged over the length L of the coil. The projection of the spin onto the initial spin direction gives the value of the polarization after the first spin echo coil

$$P = \Re(e^{i\phi}) = \cos\phi = \cos\left(\gamma \frac{\bar{B}L}{v}\right). \tag{4.6}$$

The polarization of the polychromatic atomic beam after the first spin echo

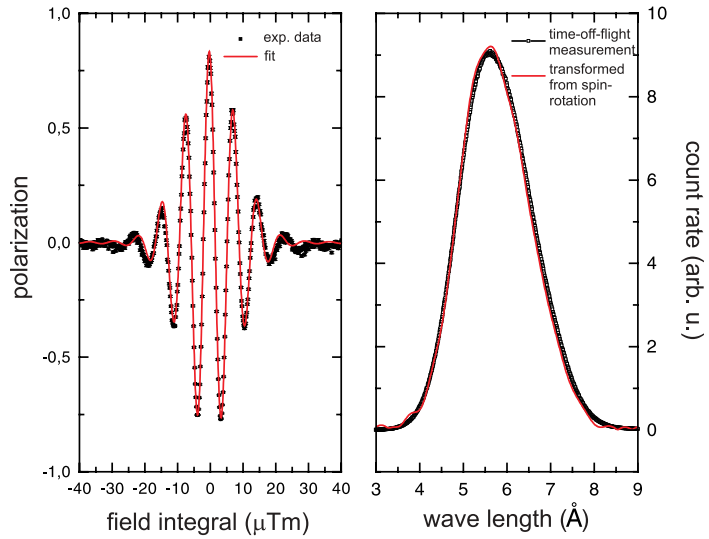

Figure 4.4: Left: Experimental spin rotation curve (dots) and fit curve (solid line). Right: Wavelength distribution obtained from the spin rotation curve by Fourier transformation (solid line) and time of flight measurement (open symbols), adapted from [Lang, 1998].

coil is given through the de Broglie wavelength distribution $n(\lambda_{dB})$ as

$$P = \int_0^\infty d\lambda_{dB}\; n(\lambda_{dB}) \cos\left(\gamma \frac{mL}{h} \lambda_{dB} \bar{B}\right). \tag{4.7}$$

From Eq. (4.7) one can see that the polarization is the cosine-Fourier transformed function of the de Broglie wavelength distribution $n(\lambda_{dB})$. The envelope of the measured polarization is related to $n(\lambda_{dB})$ through the Fourier-transformation. The functional dependence of the polarization after the first spin echo coil on the magnetic field integral $\bar{B}L$ is the so-called spin rotation curve, which is depicted on the left-hand side of Fig. 4.4. The corresponding wavelength distribution is plotted on the rigth-hand side of Fig. 4.4.

In the second spin echo coil identical to the first one but with opposite orientation of the magnetic field the spins precess back. Behind this coil the polarization takes the value of the initial polarization before the first spin echo coil. The function of the polarization on the detuning of the magnetic field integral of one of each coils represents the so-called spin echo group. Thus, one can obtain the wavelength distribution as a Fourier-transformed function of the spin echo group behind each of the two spin echo coils separately, i.e. before or after the scattering process. In the case of elastic scattering, the spin echo groups are indentical and symmetric with respect to the zero detuning of the magnetic field integral.

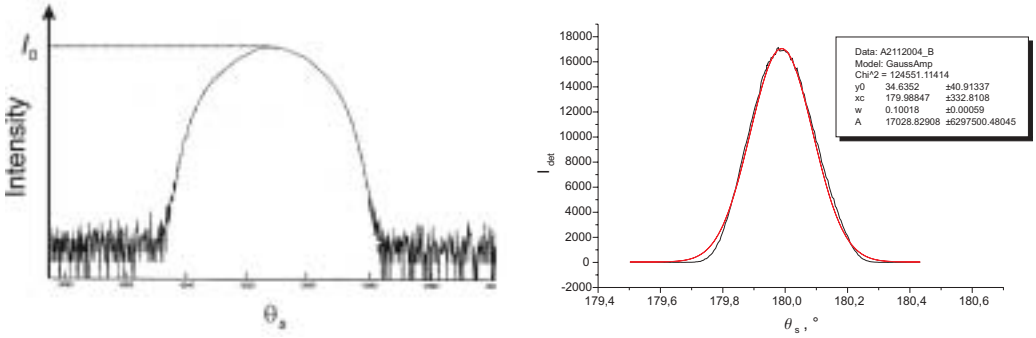

(a) (b)

Figure 4.5: Beam profile measurement: Intensity of the direct beam as a function of the detector position. (a) The intensity in logarithmic scale is plotted versus the detector position in isel-steps. The maximum I_0 determines the value of the scattering angle $\theta_s = 180°$. (b) The same data is plotted in linear scale versus the scattering angle θ_s in degrees.

If, however, the atom is inelastically scattered from the surface, which is situated between the two spin echo coils, its kinetic energy is altered. It propagates in the second spin echo coil for a different time than in the first one and acquires a different precession phase. The latter phase no longer compensates the phase, which it is accumulated in the first coil. In the case of the inelastic scattering the spin echo curve is asymmetric with respect to the zero-detuning of the magnetic field integral.

Advantages of the determination of the wavelength distribution from the spin echo curve for the quantum reflection measurement

- The spin echo curves can be obtained by the detuning of the magnetic field integral of one of each spin echo coils. Thus, we obtain the de Broglie wavelength distribution directly before or after the scattering process. From time of flight measurements the wavelength distribution behind the nozzle is obtained. By going through the polarizer it can however be changed. This changed distribution can be obtained only by Fourier-transformation of a spin rotation or a spin echo curve.

- The asymmetry of the spin echo curve with respect to the zero magnetic field integral indicates the inelastic scattering process. Quantum reflection being absolutely elastic must lead to a symmetric spin echo group.

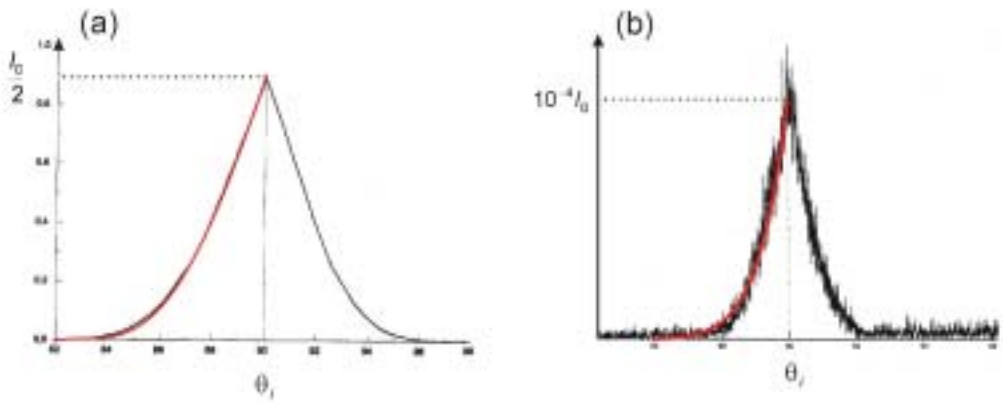

Figure 4.6: Measurement of the direct beam intensity as a function of the incident angle θ_i by rotating the target. The curve is symmetric with respect to $\theta_i = 90°$ which proves correct positioning of the target with respect to the rotation axis. The left parts of the curves are fitted with functions discussed in the text (solid lines). (a) Experimental data obtained with an α-quartz crystal. The scattering plane at $\theta_i = 90°$ coincides with the beam axis. (b) Experimental data obtained with a gold crystal. The target is inserted into the beam across the beam axis.

- The width of the spin echo group is related to the width of the wavelength distribution. In the quantum reflection process the wavelength distribution must be conserved after the scattering. The measurement of the wavelength distribution before and after the scattering process therefore gives the possibility to check it.

4.2.2 Determination of the total scattering angle

The first step in the experiments discussed in this work is the determination of the reference angle between the incident beam axis and the axis of the detector arm. The reference angle is chosen to be 180° such that it can be adjusted by scanning the angle in the presence of a direct beam without a target. The reference angle is determined by the angle at which maximum beam intensity is detected. In the following, all specifications of the angle referring to the detector position, θ_s, will be given with respect to the reference angle. Fig. 4.5 (a) depicts the detected intensity profile of the direct beam in logarithmic scale as a function of θ_s given in isel-steps. The position of the maximum intensity I_0 determines the reference angle. The same data are plotted on a linear scale versus the corresponding scattering angle in degrees

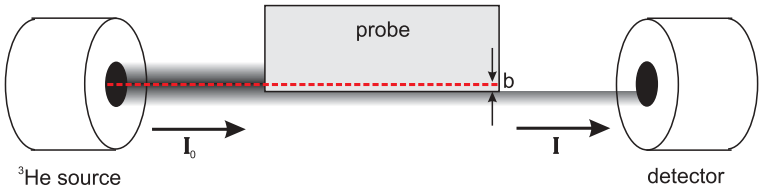

Figure 4.7: Inserting the target into the beam. The surface plane is separated from the beam axis by the distance b. I_0 and I denote the incident and detected beam intensities.

in Fig. 4.5 (b). The point, around which the detector arm is rotated, lies under the cryostat axis with a possible deviation of the order of 0.5 mm. The symmetry axis of the probed surface coincides with the cryostat axis. Thus, for a fixed angle θ_s the angle of the probed surface θ_i can be tilted around the symmetry axis in order to detect a Bragg reflex. The angle θ_i at which the Bragg reflex has maximum intensity represents the incident angle. The fixed angle θ_s represents the scattering angle $\theta_s = \theta_i + \theta_f$. The incident angle θ_i is measured between the incident beam axis and the normal to the probed surface.

4.2.3 Placing the target into the beam

After determining the scattering angle the detector is fixed under $\theta_s = 180°$ and the target is placed into the beam. The scattering plane is adjusted parallel to the incident beam axis. The incident angle θ_i is automatically scanned from 90° to 0° and from 90° to 180° using a gear mechanism. Fig. 4.6 displays the detected intensity of the direct beam while rotating the probed surface by an angle θ_i. In Fig. 4.6 (a) and (b) an α-quartz target and a gold surface were used, respectively. The position of maximum intensity determines the reference angle $\theta_i = 90°$. Perfect adjustment of the symmetry axis of the probed surface with respect to the rotating axis of the detector arm becomes manifest by a symmetric intensity curve with respect to $\theta_i = 90°$. We will concider the two possible initial positions of the surface plane:
1) The incident beam axis falls into the surface plane, and
2) the incident beam axis lies in a plane parallel to the surface plane.

In the first case the target is inserted into the direct beam such that half of the initial beam intensity, I_0, is detected (see Fig. 4.6 (a)). The scattering point, to which the position of the detector is optimized, lies in this case in the middle of the target surface and simultaneously on the incident beam axis. We now fix some scattering angle θ_s and look for a specular peak by varying the incident angle θ_i. The value $2\theta_i$, at which the maximum of the

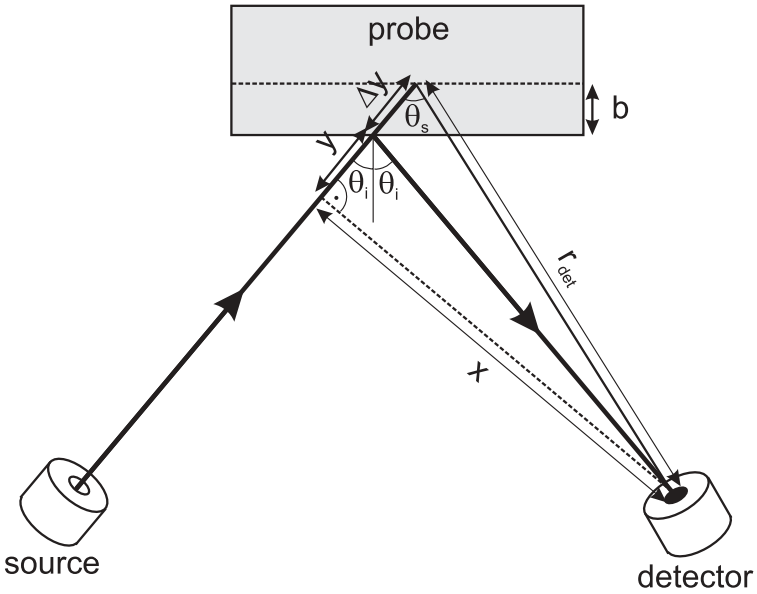

Figure 4.8: Schematic representation of the elastic scattering in the case of a shifted surface plane by the distance b with respect to the scattering point to which the detector position is aligned. The real scattering angle $2\theta_i$ exceeds the adjusted scattering angle θ_s.

specular reflected intensity is detected, will be in fact equal to the scattering angle θ_s, which was held fixed.

In the second case, when the beam axis falls into a plane parallel to the surface plane, the scattering point does not lie in the surface plane. There is some distance b between the scattering point and the surface (see Fig. 4.7). Only part of the direct beam intensity reaches the detector. If the surface plane is situated below the beam axis, the value of this intensity is smaller than $I_0/2$ (see Fig. 4.6 (b)). We now fix some scattering angle θ_s and look for a specularly reflected peak by rotating the target. The maximum intensity of this peak occurs, however, not at the incident angle $\theta_i = \theta_s/2$, but at $\theta_i > \theta_s/2$. This confirms the fact that the scattering point, to which the detector is optimized, does not lie in the surface plane, from which the beam is reflected. By measuring the values of the scattering and incident angles, the distance b can be obtained from a geometrical picture [Rowntree, 1990]. We denote the distance between the scattering point and the detector as r_{det}, the minimal distance from the detector up to the incident beam axis as x, the distance between the intersection point of the incident beam axis with x and the one of the incident beam axis with the surface as y and the distance between the intersection point of the incident beam axis with the surface

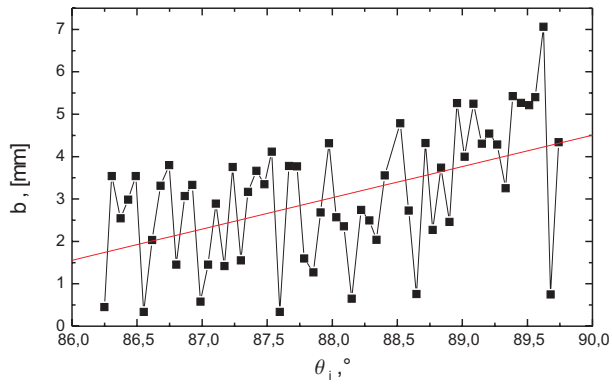

Figure 4.9: Distance b in mm as a function of θ_i calculated from the experimental data according Eq. (4.8) (full squares). Since the measurement is performed at grazing incidence the applied equation yields inaccurate results. This becomes manifest from the rising distance b with increasing θ_i. The solid line represents a linear fit of the data in order to illustrate this trend.

and the scattering point as Δy (see Fig. 4.8). Since $y = x/\tan(2\theta_i) = r_{det}\sin\theta_s/\tan(2\theta_i)$ and $\Delta y = b/\cos\theta_i$ we obtain the distance b from the equation $y + \Delta y = r_{det}\cos\theta_s$,

$$b = r_{det}\cos\theta_i\left(\cos\theta_s - \frac{\sin\theta_s}{\tan(2\theta_i)}\right). \tag{4.8}$$

The distance b between the scattering point and the surface can be obtained in such a way only if the incident angle is not too large. In the latter case the incident beam axis will hit the side of the target without intersecting the surface. The reflected intensity results from a part of the incident beam, which reaches the surface at this incident angle. The specular peak therefore has an asymmetric shape. Since the reflected beam goes through an aperture situated at the exit of the scattering chamber, the beam profile is partially symmetrized.

The detected maximum of the symmetrized reflex, however, does not correspond to the maximum of the incident beam. Therefore, the incident angle, at which this maximum value occurs, does not correspond to the real incident angle of the beam. The determination of the distance b from the difference between the fixed scattering angle and $2\theta_i$ by equation (4.8) is not correct anymore.

In the experiment with the gold surface the target was inserted into the beam, such that at $\theta_i = 90°$ only 10^{-4} of the direct incident beam intensity

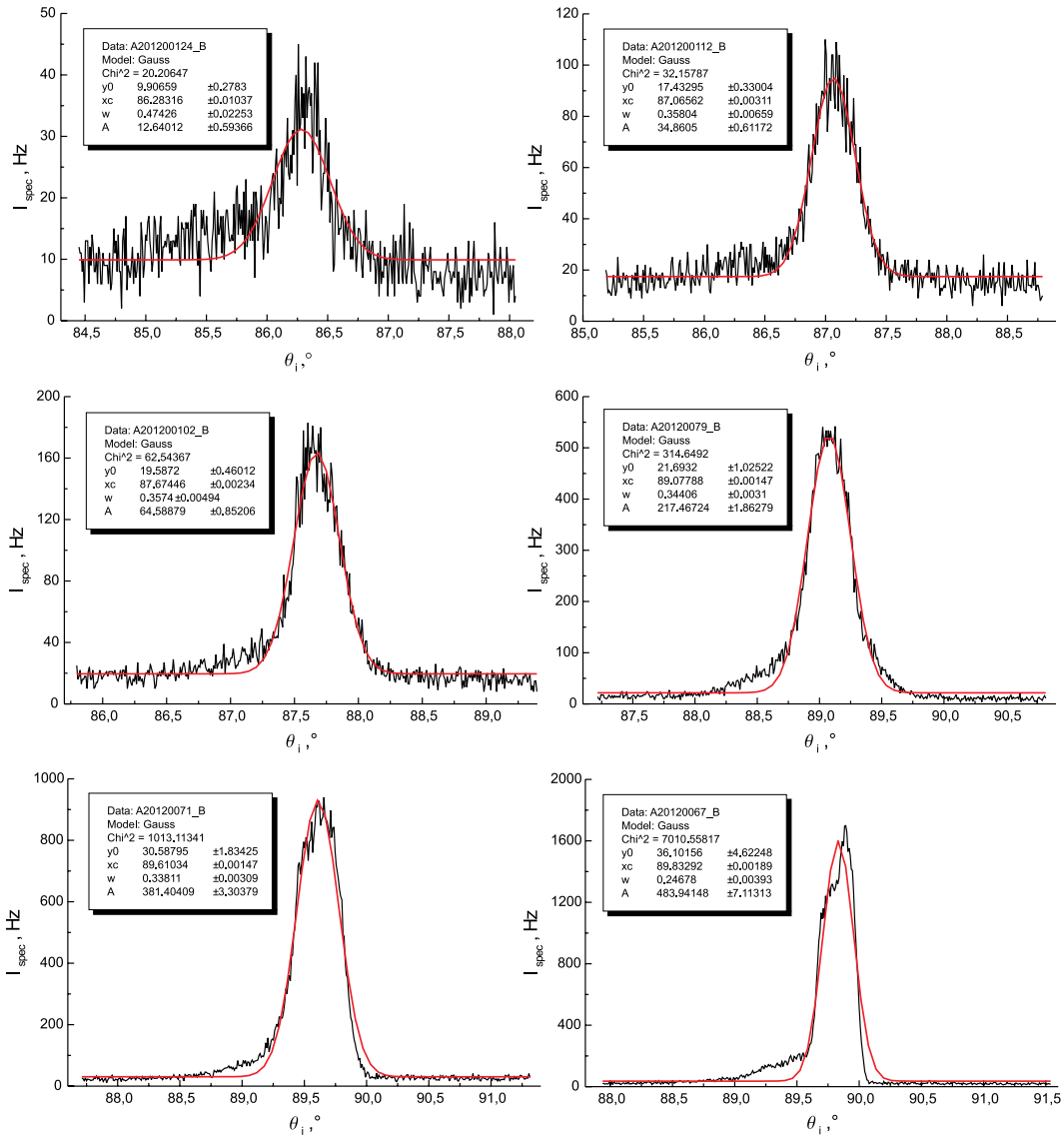

Figure 4.10: Selected profiles of the measured specular reflexes at grazing beam incidence for increasing θ_i (from top left to bottom right graph). The asymmetry of the profiles becomes visible at larger θ_i. Due to quantum reflection the maximum intensity rises for increasing θ_i. For simplicity, the data are fitted with a Gaussian function. However, the position of the intensity maximum is still to be corrected in order to give the true incident angle of the beam θ_i.

was detected. At grazing incidence in the range of incident angles between 86° and 89.8° the incident beam axis intersects the side of the target. The profiles of the specularly reflected beams at very large θ_i have a well visible asymmetrical shape, as it is depicted in Fig. 4.10. For simplicity, they are fitted by a Gaussian function. Fig. 4.9 displays the value of the distance b obtained from Eq. (4.8) as a function of θ_i. The incident angles θ_i are determined from the positions of the maxima of the Gaussian functions. One can see that the value of b increases with θ_i at grazing incidence. The solid line represents the result of a linear fit in order to illustrate this trend. The rising deviation of b from a constant value confirms the fact that θ_i cannot be determined correctly from Gaussian fits. The correct relation between θ_i and θ_s can be found from independent measurement of the value b, as discussed in the following section.

4.2.4 Reflection coefficient at grazing beam incidence

At increasing incident angle θ_i between the beam axis and the surface normal the projection of the surface onto the plane perpendicular to the beam axis decreases. This means that at large θ_i part of the beam does not reach the surface. By placing the target into the beam such that half of the incident beam intensity reaches the detector at $\theta_i = 90°$ the beam is truncated symmetrically with respect to the incident beam axis. One of two equal parts of the beam which do not reach the surface, $I_{losses}(\theta_i)$, is measured by rotating the target in the direct beam. The results of such measurements are depicted in Fig. 4.6.

The reflection coefficient $|R|^2$ from a surface S is equal to

$$|R|^2 = \frac{d\Phi_1/dS}{d\Phi_0/dS}, \tag{4.9}$$

where Φ_0 and Φ_1 denote the flux incident to the surface and the flux reflected from the surface, respectively. Since the detected intensity is the flux through the surface perpendicular to the beam axis, S_0, the reflection coefficient as a function of θ_i has the form

$$|R|^2(\theta_i) = \frac{(d\Phi_1/dS_0)\cos\theta_i}{(d\Phi_0/dS_0)\cos\theta_i} = \frac{I_{specul}(\theta_i)}{I_0 - 2I_{losses}(\theta_i)}. \tag{4.10}$$

Here, I_{specul} represents the detected intensity of the specularly reflected beam and I_0 is the intensity detected without inserting the target into the beam. In the experiment with the surface of an α-quartz crystal the function $I_{losses}(\theta_i)$

is represented in Fig. 4.6 (a) and fitted by the fourth-order polynomial function $P(\cos\theta_i) = (a+b\cos\theta_i+c\cos^2\theta_i+d\cos^3\theta_i+e\cos^4\theta_i)\ I_0/2$. The resulting fit parameters are $a = 1$, $b = -16.6$, $c = 0$, $d = 1144.7$, and $e = -4756.6$.

In the case that the surface and the scattering point are separated by some distance b the losses from both sides of the incident beam axis at grazing incidence are not equal. The incident beam profile perpendicular to the beam axis is well described by a Gaussian function, $(\omega\sqrt{\pi})^{-1}\exp(-x^2/\omega^2)$ with rms-width ω. The beam axis is situated at the coordinate $x = 0$. The fraction of the incident beam intensity reaching the surface at the incident angle θ_i is equal to $I_0\cos\theta_i(\omega\sqrt{\pi})^{-1}\int_{-L\cos\theta_i/2-b}^{L\cos\theta_i/2+b} dx\ \exp(-x^2/\omega^2) = I_0\cos\theta_i(\omega\sqrt{\pi})^{-1}\int_{-L\cos\theta_i/2}^{L\cos\theta_i/2} dx\ \exp(-(x-b)^2/\omega^2)$. Here, L denotes the diameter of the surface. The detected intensity I_{specul} is equal to the reflected flux through the surface S_1 to which the detector position is optimized. From equations $S_1/S = \cos\theta_f = \cos(\theta_s - \theta_i)$ and Eq. (4.8) it follows that $(\theta_s - \theta_i) = \theta_i - \arcsin(2b\sin\theta_i/r_{det})$. We obtain the reflection coefficient

$$|R|^2(\theta_i) = \frac{I_{specul}\cos\left(\theta_i - \arcsin(\frac{2b\sin\theta_i}{r_{det}})\right)}{I_0\frac{1}{\omega\sqrt{\pi}}\int_{-\frac{L\cos\theta_i}{2}}^{\frac{L\cos\theta_i}{2}} dx\ \exp\left(-\frac{(x-b)^2}{\omega^2}\right)\ \cos\theta_i} = |R_{uncorr}|^2\frac{\cos\left(\theta_i - \arcsin(\frac{2b\sin\theta_i}{r_{det}})\right)}{\cos\theta_i}\left[\frac{1}{\omega\sqrt{\pi}}\int_{-\frac{L\cos\theta_i}{2}}^{\frac{L\cos\theta_i}{2}} dx\ \exp\left(-\frac{(x-b)^2}{\omega^2}\right)\right]^{-1}, \tag{4.11}$$

where $|R_{uncorr}|^2$ denotes the reflection coefficient before correcting for the intensity losses and the deviation of the surface center from the scattering point.

Determination of the lengths b and ω The unknown parameters in the expression for the reflection coefficient Eq. (4.2.4), b and ω, can be obtained from the measurements plotted in Fig. 4.6 (a) and Fig. 4.6 (b) for quartz and gold surfaces, respectively. In the latter measurement the probed surface was shifted by the distance b with respect to the incident beam axis.

The curve in Fig. 4.6 (b) for the gold surface was fitted by the function $(\omega\sqrt{\pi})^{-1}\int_{-\infty}^{-L\cos\theta_i/2} dx\ \exp(-(x-b)^2/\omega^2)$ using the programm *Mathematica*. The resulting fit parameters are $b = 0.93\,\mathrm{mm}$ and $\omega = 0.57\,\mathrm{mm}$.

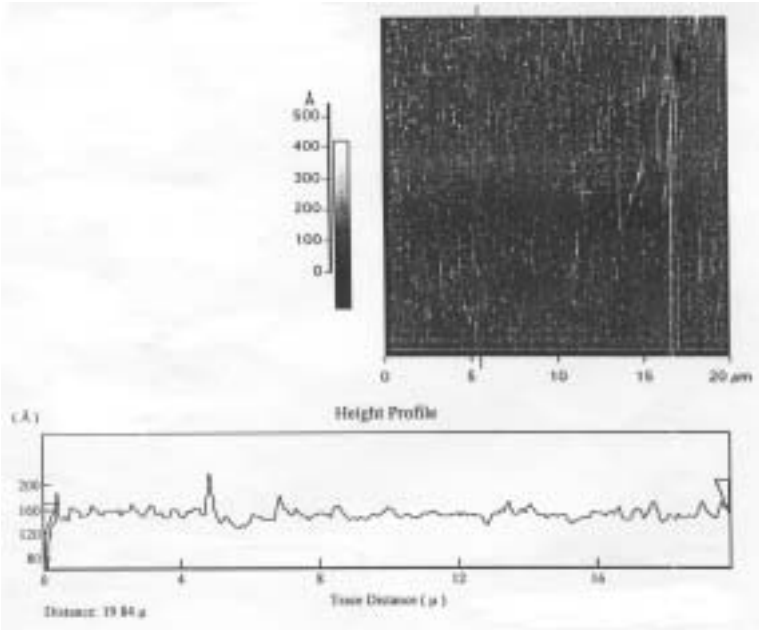

Figure 4.11: AFM-scan of the α-quartz surface. Top picture: Top view of a 20×20 μm^2-region of the surface. The left gray-scale displays the local surface height. Bottom graph: Height profile of the same region in horizontal direction.

4.3 Results

^{3}He-α-quartz measurement Our first quantum reflection experiment was performed by Christian Schmidt on an α-quartz crystal (SiO_2) with a thickness of 1 mm and a polished surface of the diameter of 25 mm. Before chemical etching of the surface of the sample, an atomic force microscopy (AFM) measurement is performed in order to check the quality of the surface. This measurement indicates that the surface is stepped with terraces between the steps of a length in the scanning direction of the order of 0.1 μm (see Fig. 4.11). The rms surface roughness, which is the rms-width of the distribution of the step heights, is determined to be 12 Å [DeKieviet et al., 1997]. The further etching could reduce this roughness, but not significantly. For our data analysis we have used a rms-width of (10 ± 2) Å. At small incident angles no low-energy electron diffraction (LEED) image and no specular reflection are obtained. From such a strongly disordered surface the beam is reflected completely diffusively. The target position is optimized to detect half of the direct beam intensity, i.e. $b = 0$ (see section 4.2.3).

A 4.2 K cold ^{3}He atomic beam with the corresponding average de Broglie

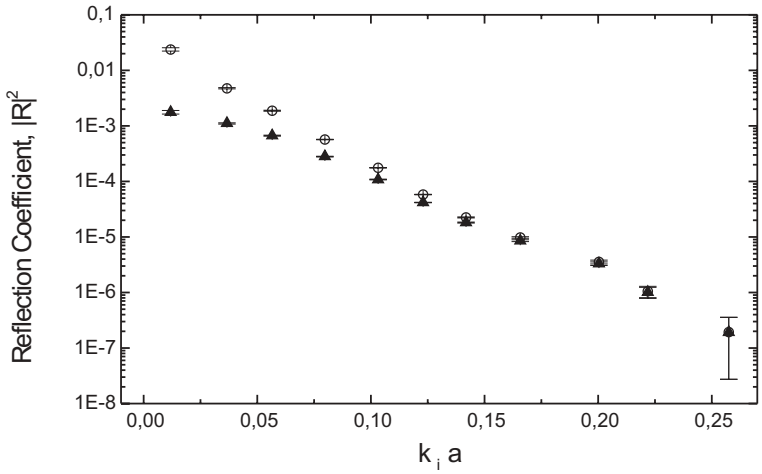

Figure 4.12: Measured reflection coefficient from the α-quartz surface at grazing incidence with respect to the dimensionless average wave number (full triangles). The open circles depict the corrected reflection coefficient to the case that the entire beam intensity reaches the surface.

wavelength of 5 Å is formed as described in Sec. 4.1.2. In the range of incident angles between 84° and 89.73° specular reflection is measured. Since the intensity of the reflected beam is much lower than the intensity of the incident beam it was not necessary to strongly attenuate the incident beam. The rate of incident atoms per second through a surface perpendicular to the beam axis, intensity I_0, is fixed to 1.8 10^8 Hz [1].

The measured reflection coefficient is equal to the ratio of the measured specular reflected beam intensity to the incident one. It is depicted by the full triangles in Fig. 4.12 as a function of the dimensionless average incident wave number normal to the surface, $k_i a = k_0 \cos\theta_i a$. Here, $k_0 = 0.93$ Å^{-1} and $a =$ 2.65 Å denote the incident wave number and the position of the ^{3}He-atom-α-quartz-surface potential minimum [Kunc and Shemansky, 1985]. The data are corrected to the incident beam intensity losses at grazing incidence as it is detailed in Sec. 4.2.4. These corrected data are represented in Fig. 4.12 by open circles and denote the values of the reflection coefficient in the case when the entire incident beam intensity would reach the surface.

For every incident angle, at which the specular reflex is measured, the spin rotation curve is recorded in order to know the exact wavelength distribution

[1]During the adjustment of the target in the direct beam the incident intensity I_0 is attenuated to the value of 1.8 MHz due to the saturation rate of the detector of the order of 2 MHz (see Fig. 4.6 (a))

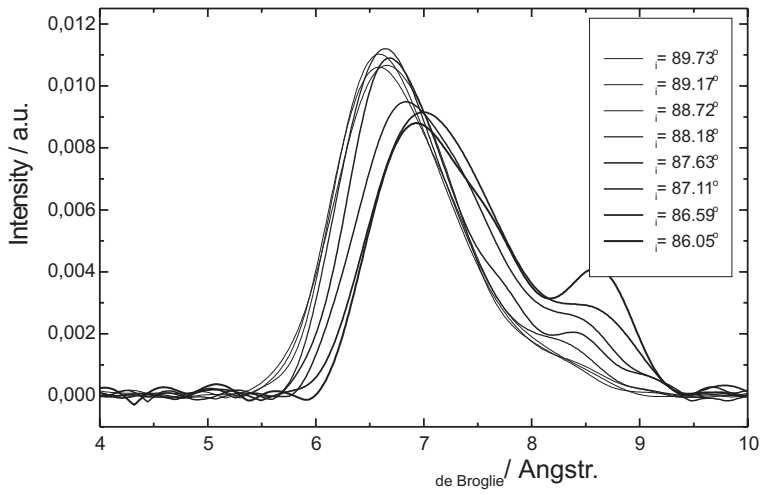

Figure 4.13: Wavelength distributions before the scattering process at different incident angles obtained from Fourier-transformation of the measured spin rotation curves.

before the scattering process. This measurement is performed by detuning the magnetic field integral of the first spin echo coil, which is situated in front of the target. The de Broglie wavelength distributions, which are obtained by Fourier-transformation of the spin rotation curves, are plotted in Fig. 4.13. The shift of the average de Broglie wavelength in the direction of larger values and the appearance of a second maximum of the curves result from a combination of filter peculiarities of the polarizer and the analyzer. At $\theta_i = 89.73°$ the average de Broglie wavelength is measured to be 6.5 Å. The corresponding incident beam energy $E_0 = \hbar^2(2\pi)^2\lambda_{dB}^{-2}/(2m)$ then amounts to 0.63 meV. In the course of data analysis the shift of the average incident energy from this value for different θ_i is taken into account.

For the interaction of a ^{3}He-atom with the dielectric α-quartz surface the potential strength C_4 is obtained by multiplying the C_4-coefficient of the interaction with a perfectly conducting surface with a function of the surface dielectric constant $\epsilon = 4.5$ [Tab, 1980] (see Eq. (3.19)). Since the function $(\epsilon-1)/(\epsilon+1)\phi(\epsilon)$ is equal to 0.492, C_4 takes the value $C_4 = 3.93\ 10^{-58}$ Jm^4 = 23.6 eVÅ^4. The attractive Casimir-van der Waals potential between the ^{3}He-atom and an α-quartz surface as a function of the atom-surface distance r in units Å, is given in eV by

$$V(r) = -\frac{23.6}{r^3(r+93)}. \tag{4.12}$$

The numerical simulation for quantum reflection from this potential is

represented by a solid line in Fig. 4.14. The method for this simulation is already discussed in chapter 2, section 2.2. Since the quantum reflection is simulated for scattering from a smooth surface, the further correction of our data obtained from a strong disordered surface is necessary. The correction factors for the reflection coefficient from a stepped surface with Gaussian distributed step heights are calculated in chapter 3, section 3.4.1. The transfer width in the interval of the incident angles, in which quantum reflection is measured, has the values between 2 μm and 40 μm and is much larger than the average terrace length $L \simeq 0.1$ μm. Thus, these factors can be used to transform the data obtained from our disordered surface to the data for a smooth surface in order to compare them with the simulated curve. The resulting values of the reflection coefficient at scattering from a smooth surface are depicted in Fig. 4.14 by full circles. They are in excellent agreement with the expected, numerically calculated values. Open circles in the same figure correspond to the open circles in Fig. 4.12.

The figure in the right top corner of Fig. 4.14 shows the reflection coefficient on a $\ln(-\ln)$-scale in order to observe the high- and low-energy asymptotes as straight lines with respect to $\ln(k_i a)$. As one can see, our data lye in the energy-region between the low-energy asymptote, Eq. (2.111), and the high-energy asymptote, Eq. (2.72), coming very close to the latter asymptote. Since the ρ-parameter for the system ^{3}He-atom-α-quartz-surface is small, $\rho = (1.9 \pm 0.2)$, the high-energy asymptote is determined only by the non-retarded van der Waals potential and is given by Eq. (2.82). In Fig. 4.14 this asymptote is represented by a solid straight line with the slope 1/3. It is the first theoretically explained measurement of the quantum reflection very close to the high-energy limit, which can be analytically described in the frame of the q uasi-classical approximation (see Sec. 2.3).

In order to compare the calculated potential strength $C_3 = 253.8$ meV Å^3, which is confirmed by our measurement with the accuracy of 11%, we use the formula (3.46) and the parameters $V_0 = 9.6$ meV, $a = 2.65$ Å and $n = 13.5$ from [Kunc and Shemansky, 1985]. The given literature values lead to the parameter $C_3 = 236.4$ meV Å^3, which corresponds to the calculated value with the accuracy of 7%.

At the incident angles θ_i lying between 84° and 89.73° the incident normal energy $E_i = E_0 \cos^2 \theta_i$ is between 6.9 μeV and 14 neV. The distance r_0 is determined from the equation $r_0^3(r_0 + l) = C_4/E_i$ and lies between 30 Å and 183 Å. Since quantum reflection occurs from the vicinity of r_0 we probe the interaction potential approximately at the distances between 30 and 200 Å. The temperature correction at such distances is predicted to be negligible (see Sec. 3.2).

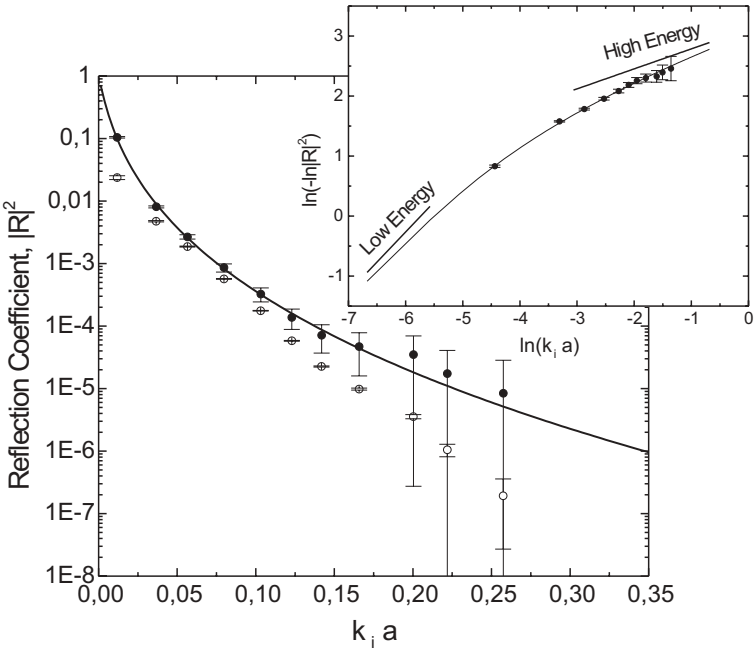

Figure 4.14: Reflection coefficient as a function of the dimensionless incident wave number $k_i a$ ($\propto \cos\theta_i$). Open circles: Experimental data from the stepped surface. Full circles: Corrected data, representing QR from the smooth surface. Solid line: Computer simulation using the potential given by Eq. (3.21) parametrized with $C_4 = 23.6\,\mathrm{eV\AA}^4$ and $l = 9.3\,\mathrm{nm}$. Inset: Replot of the same data on a $\ln(-\ln)$-scale versus $\ln(k_i a)$. The straight line of slope=1/3 shows the asymptote Eq. (2.111) with $\beta_3 = 347\,\mathrm{\AA}$; the straight line at small $\ln(k_i a)$, with slope=1 and ordinate axis intercept $\approx \ln(2.4\beta_3/a)$ for $\rho \approx 1.9$ [Friedrich et al., 2002], is the low-energy asymptote Eq. (2.111).

^{3}He-gold (Au(111)) measurement In the scattering experiment with ^{3}He and a gold surface, performed by Thilo Stöferle, the atomic beam is cooled down to a temperature of 1.3 K. This ^{3}He atomic beam has a wavelength distribution with a relative width of about 20 % at an average de Broglie wavelength of 9 Å. The corresponding average kinetic energy of the beam amounts to 0.337 meV. The target is placed into the beam with the surface plane being at the distance b from the beam axis (see Fig. 4.7). The (111)-surface of an Au crystal of a diameter of 2 cm was atomically rough so that no LEED and no ^{3}He specular peak were observed at small incident angles θ_i. At the incident beam intensity of 5 MHz quantum reflection was measured in the interval of the incident angle θ_i between 86.283° and 89.833°. The measured reflection coefficient as a function of the incident nor-

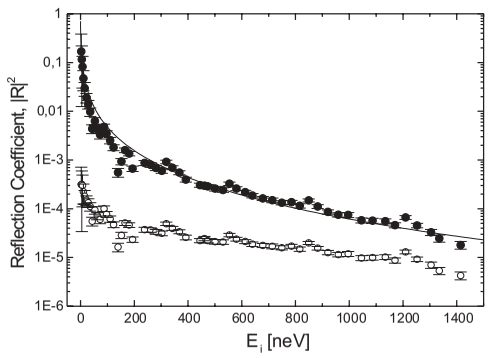

Figure 4.15: Measured reflection coefficient from Au(111) at grazing incidence versus the energy of the incident atoms perpendicular to the surface (open circles). Reflection coefficient corrected to the case that the entire incident beam intensity reaches the surface (full circles). The solid line depicts the result of the numerical simulation.

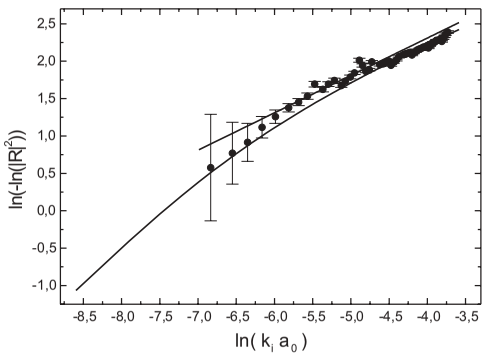

Figure 4.16: Same corrected data as in Fig. 4.15 in a $\ln(-\ln)$-scale versus the ln of the dimensionless wave number (full circles). The solid line corresponds to the numerical simulation in Fig. 4.15. The solid straight line with slope 1/2 represents the high-energy asymptote which is determined by the pure retarded Casimir potential.

mal kinetic energy E_i is represented by open circles in Fig. 4.15. At grazing incidence only a fraction of the beam intensity reaches the surface. We take this into account by correcting the reflection coefficient as it is described in detail in Sec. 4.2.4. All numerical parameters are presented in section 4.2.4 as well. The reflection coefficient from a smooth surface in the case that the entire beam intensity reaches the surface is depicted as a function of the incident energy by full circles in Fig. 4.15.

The potential strength C_4 for the Casimir-van der Waals attractive interaction between a neutral ^{3}He atom and a perfectly conducting surface, given by equation $C_4 = 3\hbar c\alpha/(8\pi)$, takes the value $C_4 = 7.783\ 10^{-58}\,\mathrm{Jm}^4 = 48\,\mathrm{eV\AA}^4$. Taking into account the transition length $l = 93\,\mathrm{\AA}$ the attractive potential between the perfectly conducting surface and the ^{3}He atom as a function of the distance r in Å is given in eV by

$$V(r) = -\frac{48}{r^3(r+93)}. \tag{4.13}$$

In the interval of θ_i from 86.283° to 89.833°, in which our experiment is performed, the normal incident beam kinetic energy lies between 1.1 μeV and 2.4 neV. The corresponding distance r_0 falls between 64 and 356 Å, re-

spectively. We probe the interaction potential approximately in this interval. At such large distances it is assumed that the atomic roughness does not influence the attractive potential, however it destroys specular reflection from the repulsive potential wall. Numerical simulation of the quantum reflection coefficient from a flat conductive surface is carried out in analogy to the one in the previous experiment and is depicted by a solid line in Fig. 4.15. In this simulation the parameter l is held fix at 93 Å and C_4 is varied in order to fit the experimental data. We obtain the value $C_4 = (45 \pm 6)$ eVÅ^4, which is in perfect agreement with the calculated value of 48 eVÅ^4. Fig. 4.16 shows the experimental data and the numerical simulation on a $\ln(-\ln)$-scale versus the ln of the average incident wave number k_i normalized to the Bohr radius $a_0 = 0.529177$ Å. The solid straight line with the slope of 1/2 represents the hight-energy asymptote Eq. (2.83), which is determined by the pure retarded Casimir potential $-C_4/r^4$. For the parameter $\rho = 2.9$ we calculate the validity range of this asymptote from Eq. (2.88) to be $-7.3 \ll \ln(k_i a_0) \ll -4.1$. In the latter range this asymptote is the dominating one. Since, however, the parameter ρ is relatively small, the range in which this asymptote dominates is comparatively small. At much higher energies $\ln(k_i a_0) \gg -4.1$ the behavior of the reflection coefficient is determined by the non-retarded potential.

We calculate the van der Waals potential strength $C_3 = C_4/l = 516$ meVÅ^3 and obtain the value of $C_3 = (484 \pm 65)$ meVÅ^3 from fitting our data. We can compare the van der Waals potential in the vicinity of the position of the potential minimum with a literature value. Since however at $r \ll l$ the imperfection of the surface conductivity changes the value of C_3 we must take this effect into account. By using the literature values for the interaction potential $V_0 = 8$ meV, $a = 3.98$ Å and $n = 12$ [Vidali et al., 1991] we obtain the value of the potential strength from the formula (3.46) $C_3 = 703$ meVÅ^3. Taking into account the correction of C_3 given by Eq. (3.40) at the position of the potential minimum the strength coefficient at this distance amounts to C_3(corrected in a)= (629 ± 85) meVÅ^3, which is in agreement with the value of 703 meVÅ^3 obtained by using the literature potential parameters.

4.3.1 Reflection from a truncated potential

In [Böheim and Brenig, 1982] the quantum reflection process is described by the reflection coefficient from a truncated potential. This potential has the form of the real interaction potential at atom-surface distances exceeding the position of the potential minimum a and a constant value of the potential minimum $-V_0$ at smaller distances. The potential is plotted in Fig. 4.17. The motivation for such a description of the reflection process is that quantum

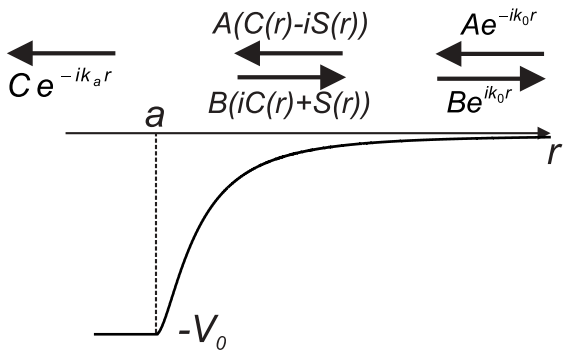

Figure 4.17: Schematic illustration of the truncated interaction potential. The real total interaction potential is truncated at the position of the potential minimum a and continued by the constant value of the potential minimum $-V_0$ for distances smaller than a. The arrows to the right of the distance a indicate the incident and reflected wave functions very far away and close to the surface. The arrow to the left of the distance a represents the wave function of the transmitted wave.

reflection occurs already from the attractive part of the potential. In the truncated potential the repulsive wall is absent. In this case one can assume that the part of the wave reaching the potential minimum (or the repulsive wall in the real potential) propagates further with constant velocity. This corresponds to the complete adsorption to the surface in the case of a real interaction potential. The entire reflection from the truncated potential then results from the attractive part of the potential.

The formula for the reflection coefficient given in [Böheim and Brenig, 1982] is calculated in the following way. The wave function near the surface propagating towards the surface can be represented by a linear combination of two functions of the coordinate, $\Psi(r) = A(C(r) - iS(r))$. At very large distance r these functions behave as $\cos(k_0 r)$ and $\sin(k_0 r)$, respectively, so that at $r \to \infty$, $\Psi(r)$ approaches the wave function of the free wave propagating towards the surface, $A\exp(-ik_0 r)$. Here, A denotes the initial wave amplitude. The reflected part of the wave function is represented by $\Psi^*(r) = iB\Psi(r) = B(iC(r) + S(r))$. The transmitted wave propagating further in the constant part of the potential is described by the wave function of a free wave, $\Psi_0(r) = C\exp(ik_a r)$, where $k_a = \sqrt{k_0^2 + 2mV_0/\hbar^2}$. The constants B and C denote the amplitude of the corresponding wave functions. By matching the sum $\Psi(r) + \Psi^*(r)$ to $\Psi_0(r)$ at the position of the potential minimum a,

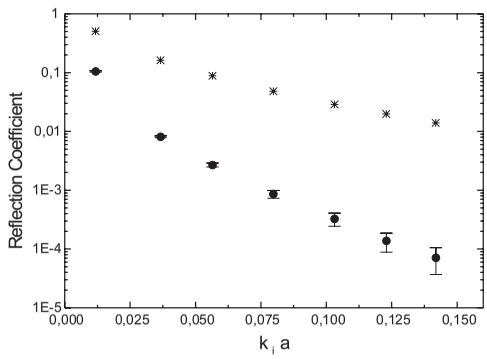

Figure 4.18: Simulated reflection coefficient from the truncated potential versus the dimensionless wave number (stars). Experimental data corrected to the case of a smooth surface (full circles).

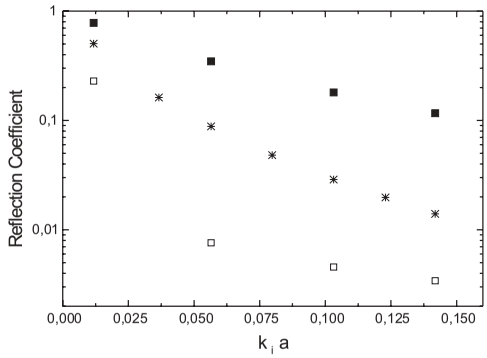

Figure 4.19: Same simulated data points as in Fig. 4.18 (stars). The full and open squares correspond to the simulated reflection coefficients from the potentials with factor 10 smaller and factor 10 larger potential strengths, respectively.

$(\Psi'(a) + \Psi^{*\prime}(a))/(\Psi(a) + \Psi^*(a)) = \Psi_0'(a)/\Psi_0(a)$, we obtain the reflection coefficient

$$R = \frac{B}{A} = 1 - \frac{4kk_0}{(C'(a) - k_0 S(a))^2 + (S'(a) + k_0 C(a))^2}. \tag{4.14}$$

Here, the prime denotes the derivative with respect to r. In this calculation the Wronskian $W\{C(r), S(r)\}$ is fixed to be equal to k.

We simulate the scattering process of ^{3}He-atom from the truncated potential with the attractive part of the ^{3}He-atom-α-quartz-surface in order to compare the simulated reflection coefficient with our experimental data. For simplicity, the retardation effect is ommited. The values of the reflection coefficient resulting from the numerical simulation are represented by stars in Fig. 4.18. In the same figure, the experimental data corrected to the expected values of the reflection coefficient from a smooth surface are depicted by solid circles. One observes a strong deviation between the simulated and experimental values especially for higher energies.

This deviation can be explained in simple terms. The reflection coefficient given by Eq. (4.14) describes the process of the reflection from the step, which is formed by the truncated potential. The reason for this process is the shifting of the phase of the wave function near the surface to the phase of the wave function of the free wave penetrating "deep into the surface". In contrast to this process quantum reflection occurs far from the surface

and is independent of this phase shift. In spite of the similar behavior of the reflection probability from the step as a function of the energy of the incident wave, the reflection coefficient has a larger value than the quantum reflection coefficient. It includes the values of the quantum reflection coefficient and the reflection coefficient resulting from the phase shift at the edge of the potential step. At lower energies the deviation between the values of the reflection coefficient from the truncated potential and the quantum reflection coefficient vanishes, because the largest part of the incident wave is firstly quantum reflected far from the surface, thereby suppressing reflection near the surface.

Fig. 4.19 shows the dependence of the reflection coefficient from the truncated potential on the dimensionless wave number of the incident wave for three different values of the potential strength. The stars, full boxes and open boxes correspond to the real value, to the factor 10 smaller value and to the factor 10 larger value of the real potential strength, respectively. For smaller values of the potential strength the reflection coefficient increases, which coincides with predictions for quantum reflection. However, the quantitative description of quantum reflection by the reflection from the truncated potential is not possible as is discussed above.

Simulation of the reflection from the truncated potential The first version of a program for simulating the reflection coefficient from a potential with boundary conditions, for instance from the truncated potential, was written by Ulrich Schmidt in *Mathematica* [Schmidt, 2002]. The important feature of this program is the possibility to observe the dynamical development of wave packets from infinity towards the surface and the other way around. A wave packet describes a non-monochromatic beam and has a wave function given by the integral over all monochromatic wave functions with corresponding probabilities.

The program works in the following steps:

- The interaction potential is subdivided into many linear intervals. This modelled potential approaches the real potential shape when the interval lengths are very small.

- Boundary conditions must be defined. Firstly, very far from the surface the potential is assumed to be zero. Secondly, the condition for the potential near the surface has to be determined. In the case of the truncated potential this condition is described by the constant value of the potential at the coordinates smaller than the position of the potential minimum.

- The wave function is given in an analytic form in every coordinate interval. In the intervals, in which the potential has a constant value, i.e. very far from the surface and "deep inside the surface", the wave functions have the exponential form for a freely propagating wave. In an interval, in which the potential is linear with the coordinate, the wave function is given by linear combination of Airy-functions, Ai and Bi. The argument of these functions depends on the coordinate, wave number and the potential value in the interval.

- The propagation time can be chosen for instance such that at $t = 0$ the wave reaches the position of the potential minimum. At very large negative times the wave function is still very far away from the surface and at very large positive times the wave function of the reflected wave is already far away from the surface.

- The dynamic development of the wave function from $t \simeq -\infty$ to $t \simeq +\infty$ is realized by matching the wave functions of neighbouring intervals.

- A wave packet is approximated by the sum of a large finite number of weighted wave functions with different wave numbers. For every value the development of the corresponding wave function is determined. This results in the development of the total wave paket.

- The intensity of the wave packet is calculated by integrating the absolute value of the wave function squared over the coordinate. The simulated value of the reflection coefficient is given by the ratio of the reflected intensity to the incident one far from the surface.

Unfortunately, the simulation of the quantum reflection coefficient using this program is hardly possible. The reason is the necessity to give the boundary condition for the potential at $t = 0$. All such conditions lead to a phase shift of the wave function, resulting in additional reflection. Since quantum reflection occurs solely at small values of the incident atom energy the wave packet is correspondingly very broad. Thus, it is impossible to spatially separate quantum reflection from the additional reflection.

4.4 Analysis of the experiments by Shimizu *et al.*

In this section we present the analysis of the experimental data published by [Shimizu, 2001, Shimizu and Fujita, 2002]. In one out of two experiments

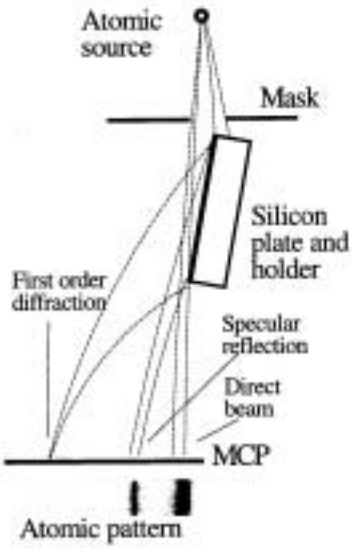

Figure 4.20: Schematic illustration of the experimental setup for measuring quantum reflection, from [Shimizu and Fujita, 2002].

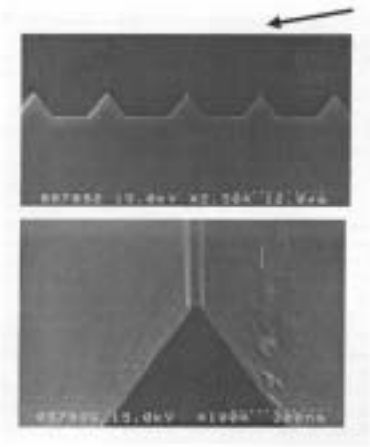

Figure 4.21: Scanning microscope photograph of the silicon grating surface. Top: Cross-sectional view. Bottom: Expanded view of the ridge. From [Shimizu and Fujita, 2002].

quantum reflection of metastable neon atoms from a silicon (1,0,0) surface (and also from a BK7 glass surface) is measured at very low incident energies. In the second experiment, which is performed with the same experimental setup, the surfaces of four silicon samples are specially prepared, as it will be discussed below.

The experimental setup is schematically shown in Fig. 4.20 from [Shimizu and Fujita, 2002]. Neon atoms in the state $1s_5$ are trapped and cooled in a magneto-optical trap (MOT). They are optically pumped into the metastable state $1s_3$ and are released from the trap, falling under the gravitational force with the average velocity $\langle v_0 \rangle$ of 3 m/s. The atoms reach the silicon surface and are specularly reflected. The atom energy perpendicular to the surface is varied by changing the angle between the surface and the incident atomic beam. The value of this angle is measured by a reflex of an additional He-Ne laser, which is directed onto the surface from aside. The reflected beam forms a line-shaped image on a microchanel plate detector (MCP). The internal energy of roughly 10 eV of the metastable neon is large enough to produce a signal in the MCP detector.

In the first experiment quantum reflection from a smooth surface is studied as a function of the incident atom velocity normal to the surface. In

sample	p [μm]	d [μm]	d/p	β_3 [μm]	β_4 [μm]	ρ	$\ln(\langle v_i \rangle$ [mm/s])$\ll$
non-ridged surface	1	1	1	6.0	0.60	10	1.7
1	100	11	0.11	0.66	0.20	3.31	2.8
2	100	1	0.01	0.06	0.06	1	4.0
3	10	$4\,10^{-2}$	0.004	0.024	0.038	0.63	4.4
4	30	$4\,10^{-2}$	0.0013	0.008	0.022	0.37	5.0

Table 4.2: List of the relevant parameters for five experiments by [Shimizu, 2001, Shimizu and Fujita, 2002] with different surface shapes: periodicity of the ridges p, width of the top of the ridges d, ratio d/p, length paramters for van der Waals and Casimir potentials β_3 and β_4, parameter ρ, and validity range of the low-energy asymptote in terms of the logarithm of the normal atom velocity.

the second experiment periodic ridges with flat top are prepared on the surfaces of four silicon samples (see Fig. 4.21 from [Shimizu and Fujita, 2002]). The details of the experiments and the surface preparation are presented in [Shimizu, 2001, Shimizu and Fujita, 2002].

The periodicity of the ridges, p, and the width of the top, d, are different for each sample. These values for all samples are listed in Tab. 4.2. The motivation for studying such surfaces is the following. In all formulas (see Eq. (2.82), Eq. (2.83) and Eq. (2.111)) the quantum reflection coefficient is a function of the product $(k_i b)$, where b is proportional to β_3 or β_4. This means that the reflection coefficient increases not only with decreasing energy of the atom perpendicular to the surface (or k_i), but also with decreasing potential strength $\beta_3 \propto C_3$ (or $\beta_4 \propto \sqrt{C_4}$). In the first order of accuracy the potential strength C_3 (or C_4) is proportional to the density of surface atoms. For a ridged surface the potential strength is reduced by approximately the factor d/p, $C_3 \to (d/p)\, C_3$, if we assume that the reflection occurs above the first surface layer, i.e. above the plane of the top of the ridges. In this case the potential length β_3 is also reduced by the same factor d/p, the length parameter of the Casimir potential β_4 and the parameter ρ by the factor $\sqrt{d/p}$, $\beta_3 \to (d/p)\, \beta_3$, $\beta_4 \to \sqrt{d/p}\, \beta_4$ and $\rho \to \sqrt{d/p}\, \rho$. The experiments are performed in the same region of normal velocities of the incident atoms between approximately 1 and 33 mm/s. For the samples with different ratio d/p one expects that the reflection coefficient increases with smaller d/p. Fig. 4.22 shows the measured behavior of the reflection coefficient (in the figure denoted as reflectivity). One can see that for smaller ratio d/p the reflection coefficient is larger at the same atom velocity.

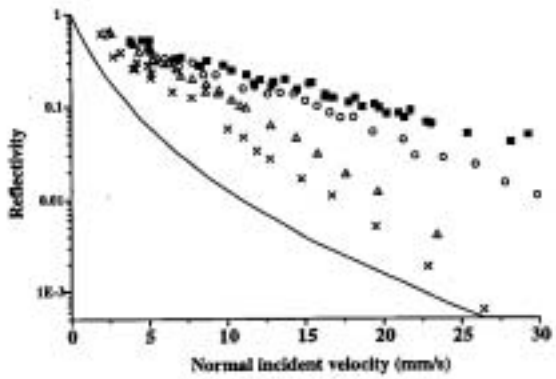

Figure 4.22: Measured reflection coefficient versus the normal incident velocity: smooth surface (solid line) and ridged surfaces with d/p = 0.11, 0.01, 0.004, and 0.0013, (crosses, open triangles, open circles, and full squares, respectively), from [Shimizu and Fujita, 2002]

.

For the static polarizability of the metastable neon atom α = 2.8 $10^{-39}\,\mathrm{Fm}^2$ [Shimizu, 2001] the potential strength of interaction between this atom and a perfectly conducting surface is given by C_4 = 9.475 $10^{-56}\,\mathrm{Jm}^4$. The transition length l is of the order of $0.1\,\mu$m. The Si-crystal has the dielectric constant $\epsilon = 12$ [Ashcroft and Mermin, 2001], so that the potential strength must be corrected by the factor $\phi_1(\epsilon) = 0.68$. The resulting attractive Casimir- van der Waals potential is given in J by

$$V(r) = -\frac{6.5\ 10^{-32}}{r^3(r+0.1)}, \tag{4.15}$$

where the distance r is expressed in μm.

The upper left graph of Fig. 4.23 represents the measured reflection coefficient from a smooth silicon surface versus the average normal atom velocity $\langle v_i \rangle = \langle v_0 \rangle \cos\theta_i$. The solid curve in this figure corresponds to the numerical simulation of the reflection coefficient from the Casimir-van der Waals potential (Eq. (3.21)) with parameters $C_4 = 6 \cdot 10^{-56}\,\mathrm{Jm}^4$ and $l = 0.06\ \mu$m, which are of order of the values given above. A similar analysis in the case of a flat surface is presented in [Friedrich et al., 2002]. Below this figure the analogous figures for four ridged surfaces are presented. The corresponding ratios d/p are listed in Tab. 4.2. The solid line in each figure represents the simulation of the reflection coefficient from the Casimir-van der Waals potential with parameters $C_4 = (d/p)\ 6 \cdot 10^{-56}\,\mathrm{Jm}^4$ and the same value of $l = 0.06\ \mu$m as for a flat surface. In order to coincide with the simulation

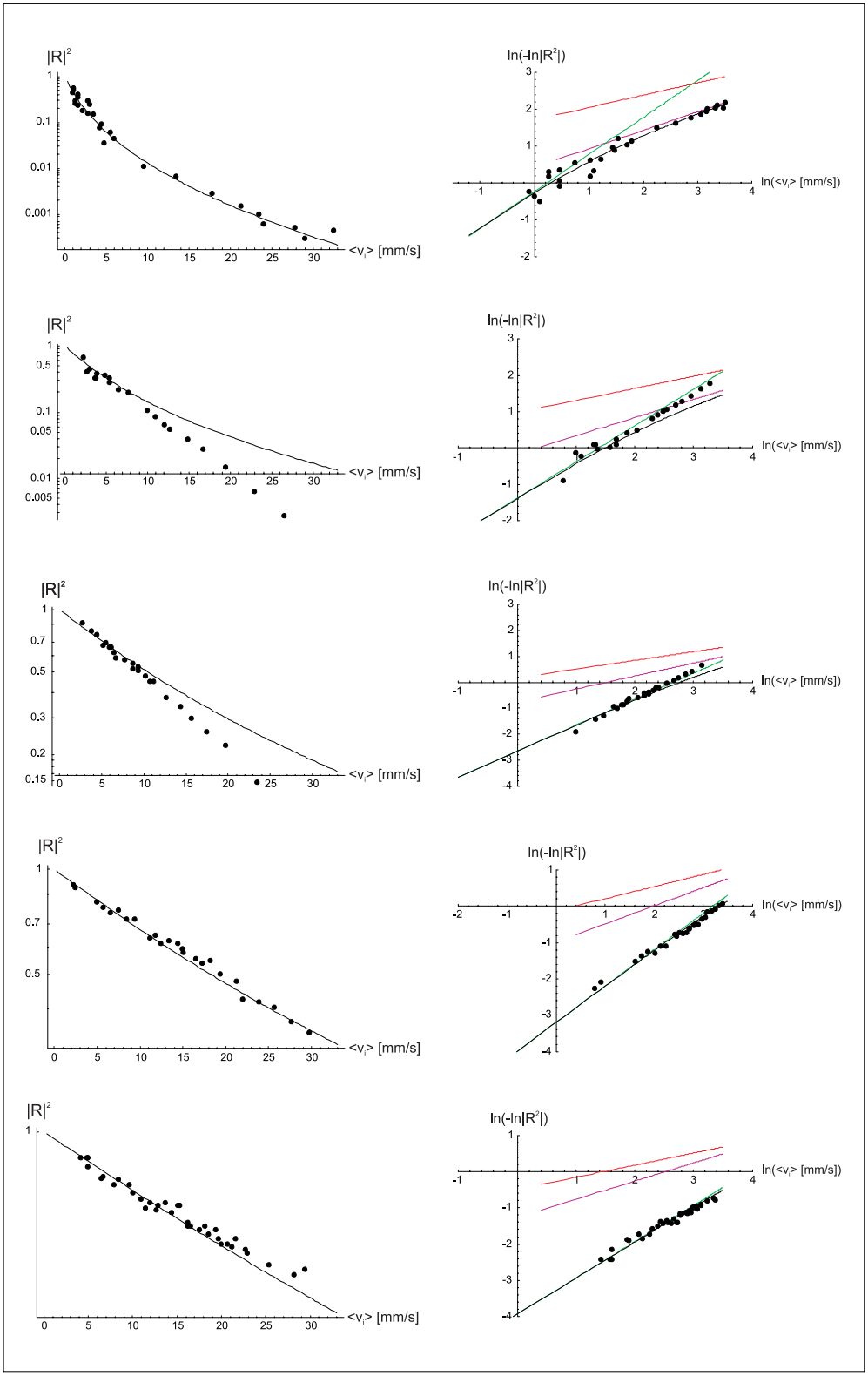

Figure 4.23: Left column, from top to bottom: Reflection coefficient versus the average normal incident velocity for five different surface shapes corresponding to the parameters listed in Table 4.2. Right column: Same coefficient on a $\ln(-\ln)$-scale versus the logarithm of the average normal incident velocity. The full circles represent the experimental data, and the solid line depicts the result of the simulation for the corresponding surface parameters. The experimental data from the ridged surfaces are corrected in order to match the simulated curves at low energies (see text). The two top straight lines in the graphs of the right column depict the high-energy asymptotes. The straight solid line with unity slope intersecting them represents the low-enery asymptote. At very small potential strength, e.g. the bottom right graph the simulated curve coincides with the low-enery asymptote in the scanned velocity range.

curve the experimental values are corrected. It was necessary to raise the reflection coefficient to the power $(d/p)^n$, where n=0.10, 0.23, 0.26 and 0.29 for each surface, respectively. Nevertheless the experimental data for the first and the second samples do not follow the simulation curve exactly even after this correction. The deviation of the experimental data from the simulated values shows that the representation of the interaction potential of the surface, excluding the influence of the sides of the ridges, is over simplified. The attraction of the incident atoms by the sides of the ridges leads to a dropping reflection coefficient.

In spite of the necessary correction the experimental data show the trend to approach the low-energy asymptote for decreasing potential strength. This can be seen from the development of the graphs on the right column of Fig. 4.23 from top to bottom. In each plot two upper straight solid lines represent the high-energy asymptotes and the straight line intersecting them is the low-energy asymptote. Since the ρ-parameter decreases for the ridged samples from top to bottom (see table 4.2), the validity range of the latter asymptote extends to larger velocities. These validity ranges are also listed in Tab. 4.2. By such measurements (provided the drop of the reflection is well investigated) the potential parameters of the flat surface can be exactly determined from the low-energy asymptote for different potential strengths of the prepared surfaces. From these potential parameters the dielectric constant of the material or the static polarizability of the atom can be inferred. Moreover, the preparation of such surfaces with small atom densities allows not only to significantly increase the value of the reflection coefficient but also to know its exact value from the simple analytical exponential form. This can be useful for experiments in atom optics and atom interferometry. Nevertheless, the exact dependence of the reflection coefficient on the parameters of the ridged surface should be investigated in more detail.

It is also important to note that the investigation of the high-energy behavior of the reflection coefficient by using metastable neon atoms is not possible. Firstly, the neon atom is factor 6.7 heavier than the ^{3}He-atom. This leads to very small values of the reflected intensities at higher energies, which are hard to detect. Secondly, a metastable atom is quenched into its electronic ground state long before it reaches the surface as a result of the interaction with surface electrons. The metastable neon atoms are quenched at the distance of about 10 nm and do not contribute to specular reflection. This means that at beam velocities larger than 7 m/s the observation of quantum reflection from a smooth silicon surface is not possible. The corresponding incident kinetic energy for this limit is equal to 0.5 μeV. For ridged surfaces this energy limit is even smaller.

4.5 Summary

In this chapter, experimental data on quantum reflection are theoretically analyzed. The experiments are performed using scattering of light and stable ^{3}He atoms from the surface of a solid. The ^{3}He atom is diffusively scattered from a rough surface which allows to measure pure quantum reflection from the attractive part of the interaction potential. The scattering energy normal to the surface of the atomic beam can be varied in the range of 1 meV to 1 neV by altering the incident angle. This energy interval includes the high-energy range of quantum reflection. Using the spin echo method the wavelength distribution before and after the scattering process can be exactly determined. Two different surfaces are investigated: The dielectric and disordered surface of an α-quartz crystal and the conductive and smooth (111)-surface of gold. The influence of the surface disorder was corrected using a simple model. The numerical simulation of the reflection coefficient discussed in chapter 2 is fitted to the experimental data and shows excellent agreement. From the simulation the Casimir-van der Waals potential parameters can be determined. The parameters extracted from the fit are in good agreement with literature values. The behavior of the reflection coefficient in dependence on the potential strength is studied in experiments by [Shimizu and Fujita, 2002] in the low-energy limit of quantum reflection. In this chapter, the experimental data are compared with theory and show qualitative agreement.

Chapter 5

Conclusion and outlook

In this thesis experimental data on quantum reflection of ^{3}He atoms from the surface of a solid is analyzed in detail. By using both a numerical model and analytic expressions for the asymptotic behavior, the quantum reflection coefficient very close to the high-energy asymptote is identified for the first time [Druzhinina and DeKieviet, 2002]. The high sensitivity of the quantum reflection coefficient to the potential energy allows the first quantitative measurement of the Casimir effect in the system atom-surface [Druzhinina et al., 2003]. In Chapter 2 the theory of quantum reflection from the attractive part of the interaction potential is compared with the non-sticking behavior of very slow atoms at the surface of liquid helium. For a long time, the latter was commonly referred to as quantum reflection in literature. In this chapter it is shown that the universal behavior of the sticking coefficient appears only in the low-energy limit. This is the result of quantum reflection from the attractive part of the potential at large distances from the surface. We find that the definition of the quantum reflection coefficient as the deviation of the sticking coefficient from unity, is valid only when scattering a light atom from liquid helium at energies, which are negligible with respect to the only bound state of the system. Only in this case, reflection from the repulsive wall can be neglected. In all other systems (and at higher energies also in this system) the repulsive wall contributes. In general, it is impossible to separate this semi-classical reflection from the one originating from the attractive part of the potential.

The first theoretical description of quantum reflection by [Pokrovskii et al., 1958] was extended to very low energies by [Friedrich et al., 2002] and provides analytic expressions for the asymptotic high-energy behavior of the quantum reflection coefficient. A more accurate validity range for these asymptotes is calculated in this work and presented in Sec. 2.3.2. In order to fit the experimental data obtained on the ^{3}He

atomic spectrometer a numerical simulation is developed in *Mathematica* based on the suggestions given in [Côté et al., 1997] and presented in Sec. 2.2.

Detailed analysis of the ^{3}He scattering experiment from a microscopically disordered α-quartz dielectric surface is presented in Chapter 4. The quantum reflection coefficient is measured at an atomic beam energy perpendicular to the surface in the range between μeV and neV and takes values between $\sim 10^{-7}$ and $\sim 10^{-2}$. The influence of microscopic surface disorder is modelled in Sec. 3.4.1 and taken into account when fitting the data. The resulting corrected values for the quantum reflection coefficient correspond to those for reflection from a flat surface and range between $\sim 10^{-5}$ and $\sim 10^{-1}$. We find that the experimental data lie close to the high-energy asymptote, which has a simple analytical form. This asymptote is determined by the non-retarded van der Waals potential and can be experimentally observed only using a light and stable atom such a helium. The parameters of the interaction potential extracted from the fit are compared with literature values and show very good agreement.

Quantum reflection is a sensitive method for probing the long-range attractive atom-surface potential. In many cases, surface roughness can be assumed to be small, so that it does not change the potential value at distances at which the incident wave is quantum reflected. One can then extract the strength parameter of the Casimir potential from the quantum reflection coefficient measured as a function of the incident atom energy. On the other hand, however, the surface must be sufficiently rough, in order to destroy semi-classical specular reflection from the repulsive part of the potential. Such quantitative measurement is performed by scattering a ^{3}He atomic beam from an atomically rough conductive gold surface under grazing incidence. The analysis of this measurement is also presented in chapter 4. It allows us to compare the parameters extracted from fits within this analysis to the values of the potential parameters from literature. A correction, which takes into account that the gold surface is not a perfect conducter, is derived in Sec. 3.3. This correction is also included in the above determination of potential parameters.

Vice versa, we would like to stress, that through quantum reflection one has the possibility of studying surface roughness and disorder. As discussed in Sec. 3.4.2, one can obtain information about the scale and form of surface roughness from the deviation of the measured potential strength from the value expected for a flat surface. This type of experiment is particularly promising at energies lying in the high-energy limit, at which quantum reflection occurs at distances close to the surface.

The quantitative undestanding of the reduction of the quantum reflection

coefficient from the ridged surface, as mentioned in Sec. 4.4, opens up the possibility of using such a surface as an efficient mirror for ultra-cold atoms with controllable losses.

Another intriguing idea is to exploit quantum reflection in the high-energy limit to guide cold ^{3}He atoms through nanotubes. This type of wave guide might be of interest in the field of atom optics and atom interferometry. Moreover, the potential between an atom and the cylindric walls of a nanotube (i.e. geometricaly modified Casimir atom-surface potential) can be measured in order to compare with very recent theoretical predictions.

Appendix A

Transformation into dimensionless form

• 1. The Schrödinger equation

$$-\frac{\hbar^2}{2m}\Psi^{''}(r) + (V(r) - E)\Psi(r) = 0 \tag{A.1}$$

is to be written in dimensionless form. Here, $\Psi^{''}(r) = d^2\Psi(r)/dr^2$. By dividing this equation by the incident kinetic energy E and by taking into consideration that $E = p_0^2/(2m) = h^2\lambda_{dB}^2/(2m)$ we obtain

$$\frac{\lambda_{dB}^2}{(2\pi)^2}\Psi^{''}(r) + \left(1 - \frac{V(r)}{E}\right)\Psi(r) = 0. \tag{A.2}$$

By introducing the dimensionless coordinate $\xi = r/a$ and the dimensionless parameters $\alpha = \lambda_{dB}/(2\pi a)$ and $k^2(\xi) = k^2(r)/k_0^2 = 1 - V(r)/E$ the Schrödinger equation in the dimensionless coordinate takes the form

$$\alpha\frac{d^2\Psi(\xi)}{2\xi^2} + k^2(\xi)\Psi(\xi) = 0. \tag{A.3}$$

• 2. The incoming semi-classical wave function is given in Eq. (2.14) by

$$\Psi(r) = \frac{C_1}{\sqrt{p(r)}}\exp\left[\frac{i}{\hbar}\int_{r_0}^{r} p(r)\,dr\right]. \tag{A.4}$$

We rewrite the wave function in dimensionless form by introducing the dimensionless coordinate $\xi = r/a$,

$$\Psi(\xi) = \frac{C_1}{\sqrt{p(\xi)}}\exp\left[\frac{ia}{\hbar}\int_{\xi_0}^{\xi} p(\xi)\,d\xi\right]. \tag{A.5}$$

By taking into consideration that the local momentum is defined by $p(\xi) = \sqrt{2m(E - V(\xi))}$ and by transforming the expression $2m(E - V(\xi))$ into $2mE(1 - V(\xi)/E) = 2mEk^2(\xi)$ we can write

$$\Psi(\xi) = \frac{C_1}{(2mEk^2(\xi))^{\frac{1}{4}}} \exp\left[\frac{ia}{\hbar}\int_{\xi_0}^{\xi} \sqrt{2mE} \cdot k(\xi)\, d\xi\right]. \tag{A.6}$$

Since $2mE = p_0^2 = \hbar^2 k_0^2$ and $\hbar/(ap_0) = 1/(ak_0) = \lambda_{dB}/(2\pi a) \stackrel{def}{=} \alpha$ the expression for the wave function takes the form

$$\Psi(\xi) = \frac{C_1}{\sqrt{\hbar k_0}} \frac{1}{\sqrt{k(\xi)}} \exp\left[\frac{i}{\alpha}\int_{\xi_0}^{\xi} k(\xi)\, d\xi\right]. \tag{A.7}$$

By assuming the constant $C_1/\sqrt{\hbar k_0}$ to be equal to unity the final expression for the semiclassical in-coming wave function in dimensionless coordinates is given by

$$\Psi(\xi) = \frac{1}{\sqrt{k(\xi)}} \exp\left[\frac{i}{\alpha}\int_{\xi_0}^{\xi} k(\xi)\, d\xi\right]. \tag{A.8}$$

• 3. We find the solution of the equation (A.3) in the form $\Psi(\xi) = e^{S(\xi)/\alpha}$ and expand the function $S(\xi)$ into a series of powers of α,

$$S(\xi) = \sum_{i=0}^{\infty} S_i(\xi)\alpha^i \tag{A.9}$$

By placing this expression into equation (A.3) and by comparing the coefficients for similar order of α we obtain the wave function with an accuracy up to the first order of α,

$$\Psi(\xi) = \frac{1}{\sqrt{k(\xi)}} \exp\left[\frac{i}{\alpha}\int_{\xi_0}^{\xi} k(\xi)\, d\xi\right]. \tag{A.10}$$

This expression is compared with the wave function in semi-classical representation Eq. (A.8). This confirms the expansion (A.9).

Appendix B

Remarks on quantum reflection theory

• Solving the integral Eq. (2.65).
In order to solve the integral $I_n = \hbar k_0 \int_{r_s}^{r_t} \sqrt{1+\beta_n^{n-2} r^{-n} k_0^{-2}}\, dr$ let us choose the path dr from r_s to r_t in the complex plane, in which every point r can be presented as $r = r_t' \xi_1 + i r_t'' \xi_2$. Here, ξ_1 and ξ_2 are real parameters and r_t' and r_t'' denote the real and imaginary parts of r_t. It follows that dr is equal to $r_t' d\xi_1 + i r_t'' d\xi_2$. Since an atom moves into the interaction potential from real infinity, it is convenient to choose the root as shown in Fig. B.1(a). The integral over the given path is then

$$I_n = \hbar k_0 \left(\int_{+\infty}^{1} f(\xi_1, \xi_2 = 0) r_t'\, d\xi_1 + i \int_0^1 f(\xi_1 = 1, \xi_2) r_t''\, d\xi_2 \right). \qquad \text{(B.1)}$$

Here, $f(\xi_1, \xi_2)$ substitutes the square root $\sqrt{1+\beta_n^{n-2} k_0^{-2} (\xi_1 r_t' + i \xi_2 r_t'')^{-n}}$. Since $r_t = r_0 \left(\cos\frac{\pi}{n} + i \sin\frac{\pi}{n}\right)$ its real and imaginary parts r_t' and r_t'' are equal

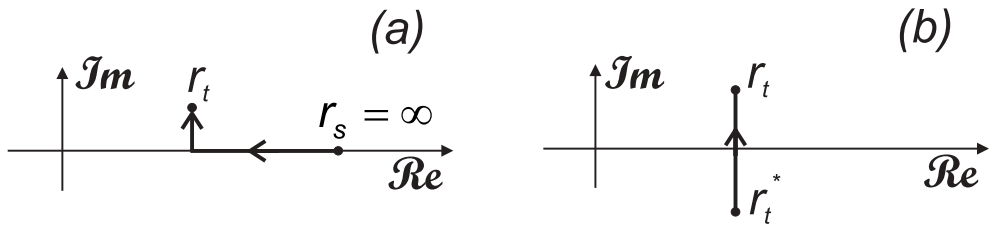

Figure B.1: The simplest paths in the complex coordinate plane for solving the integrals I_n and Δ. (a) From real infinity to complex r_t and (b) from r_t^* to r_t.

to $r_0 \cos\frac{\pi}{n}$ and $r_0 \sin\frac{\pi}{n}$, respectively. The integral I_n can then be written as

$$I_n = \hbar k_0 r_0 \left(\cos\frac{\pi}{n} \cdot I_{1n} + i \sin\frac{\pi}{n} \cdot I_{2n}\right), \tag{B.2}$$

where $I_{1n} = \int_{+\infty}^{1} \sqrt{1 + \beta_n^{n-2} k_0^{-2} \xi_1^{-n} \cos^{-n}\frac{\pi}{n} r_0^{-n}}\, d\xi_1$ and $I_{2n} = \int_0^1 \sqrt{1 + \beta_n^{n-2} k_0^{-2} (\cos\frac{\pi}{n} + i\xi_2 \sin\frac{\pi}{n})^{-n} r_0^{-n}}\, d\xi_2$. By taking into account that $\beta_n^{n-2}/r_0^n = k_0^2$ the expressions for I_{1n} and I_{2n} can be simplified,

$$I_{1n} = \int_{+\infty}^{1} \sqrt{1 + \frac{1}{\xi_1^n \cos^n\frac{\pi}{n}}}\, d\xi_1, \tag{B.3}$$

$$I_{2n} = \int_0^1 \sqrt{1 + \frac{1}{(\cos\frac{\pi}{n} + i\xi_2 \sin\frac{\pi}{n})^n}}\, d\xi_2. \tag{B.4}$$

The integral I_{1n} is real and the integral $I_{2n} = \Re I_{2n} + i\Im I_{2n}$ is complex. The complexity of I_{2n} plays the crucial role in above-barrier reflection.

• The validity range of the formula (2.72).

The difference between the phases from one virtual turning point r_t and its complex conjugate r_t^* is given through $\Delta = \tau_0 - \tau_0^* = \int_{r_s}^{r_t} k(r)dr - \int_{r_s}^{r_t^*} k(r)dr = \int_{r_t^*}^{r_t} k(r)dr$. We will take into consideration that the function $k^2(r)$ has n roots and a pole $r_1 = 0$ of the n-th degree, $k^2(r) = (r^n - r_t^n)/r^n$. The path $dr = r_t' d\xi_1 + i r_t'' d\xi_2$ from r_t^* to r_t is chosen as presented in Fig. B.1(b), i.e. $\xi_1 = 1$ and ξ_2 is varied between -1 and 1. Thus, $dr = i r_0 \sin\frac{\pi}{n} d\xi_2$ and Δ is equal to

$$\Delta = i k_0 r_0 \cdot \sin\frac{\pi}{n} \cdot \int_{-1}^{1} \sqrt{1 + \frac{1}{(\cos\frac{\pi}{n} + i\xi_2 \sin\frac{\pi}{n})^n}}\, d\xi_2. \tag{B.5}$$

The validity range of the formula (2.72) in the dimensional coordinates, $|\Delta| \gg k_0^{-1}$, is given by

$$k_0 r_0 \cdot \sin\frac{\pi}{n} \cdot |I_{3n}| \gg k_0^{-1}, \tag{B.6}$$

where $I_{3n} = \int_{-1}^{1} \sqrt{1 + (\cos\frac{\pi}{n} + i\xi_2 \sin\frac{\pi}{n})^{-n}}\, d\xi_2$. Since $r_0 = \beta_n^{1-2/n}/k_0^{2/n}$, the expression (B.6) in terms of the interaction potential takes the form

$$(k_0 \beta_n)^{1-\frac{2}{n}} \gg \frac{1}{\sin\frac{\pi}{n} \cdot |I_{3n}|}. \tag{B.7}$$

Finally we obtain

$$k_0 \beta_n \gg (\sin\frac{\pi}{n} \cdot |I_{3n}|)^{\frac{n}{2-n}}. \tag{B.8}$$

Bibliography

[Tab, 1980] (1979-1980). In: Weast, R. C. (Ed.), *CRC Handbook of Chemistry and Physics*. Florida.

[Abramovitz and Stegun, 1984] Abramovitz, M. and Stegun, I. A. (1984). In: Danos, M. and Rafelski, J. (Eds.), *Pocketbook of Mathematical Functions* , p. 154. Verlag Harri Deutsch.

[Ashcroft and Mermin, 2001] Ashcroft, N. N. and Mermin, N. D. (2001). In: *Festkörperphysik*. Oldenbourg Verlag.

[Barton, 1987] Barton, G. (1987). *Proc. R. Soc. London. Ser. A* **410**, 141.

[Basdevant and Dalibard, 2000] Basdevant, J.-L. and Dalibard, J. (2000). Quantum Reflection of Atoms from a Surface. In: *The Quantum Mechanics Solver* , p. 205. Springer, Berlin.

[Beeby, 1971] Beeby, J. L. (1971). The scattering of helium atoms from surfaces. *J. Phys. C* **4**, 359.

[Berkhout et al., 1989] Berkhout, J. J., Luiten, O. J., Setiya, J. D., Hijmans, T. W., Mizusaki, T., and Walraven, J. T. M. (1989). Quantum Reflection: Focusing of Hydrogen Atoms with a Concave Mirror. *Phys. Rev. Lett.* **63**, 1689.

[Berkhout and Walraven, 1992] Berkhout, J. J. and Walraven, J. T. M. (1992). Scattering of hydrogen atoms from liquid-helium surfaces. *Phys. Rev. B* **47**, 8886.

[Bezerra et al., 2000] Bezerra, V. B., Klimchitskaya, G. L., and Romero, C. (2000). Surface roughness contribution to the Casimir interaction between an isolated atom and a cavity wall. *Phys. Rev. A* **61**, 022115.

[Böheim and Brenig, 1982] Böheim, J. and Brenig, W. (1982). On the Low Energy Limit of Reflection and Sticking Coefficients in Atom Surface Scattering. *Z. Phys. B* **48**, 43.

[Bruder, 1997] Bruder, C. (1997). Van der Waals- und Casimir-Kräfte. http://www.ubka.uni-karlsruhe.de/.

[Carraro and Cole, 1998] Carraro, C. and Cole, M. W. (1998). Sticking coefficient at ultralow energy: Quantum Reflection. *Prog. Surf. Sci.* **57**, 61.

[Casimir and Polder, 1948] Casimir, H. B. G. and Polder, D. (1948). The Influence of Retardation on the London-van der Waals Force. *Phys. Rev.* **73**, 360.

[Cassels, 1982] Cassels, J. M. (1982). In: *Basic quantum mechanics* , pp. 73,179. The Macmillan Press LTD.

[Chen et al., 2002] Chen, F., Mohideen, U., Klimchitskaya, G. L., and Mostepanenko, V. M. (2002). Demonstration of the Lateral Casimir Force. *Phys. Rev. Lett.* **88**, 101801.

[Chung and George, 1988] Chung, S. G. and George, T. F. (1988). Theory of low-temperature adsorption. *Surf. Sci.* **194**, 347.

[Comsa, 1979] Comsa, G. (1979). *Surf. Sci.* **81**, 57.

[Côté et al., 1997] Côté, R., Friedrich, H., and Trost, J. (1997). Reflection above potential steps. *Phys. Rev. A* **56**, 1781.

[Côté et al., 1998] Côté, R., Segev, B., and Raizen, M. G. (1998). Retardation effects on quantum reflection from an evanescent-wave atomic mirror. *Phys. Rev. A* **58**, 3999.

[Davydov, 1976] Davydov, A. S. (1976). In: *Quantum mechanics.* Pergamon Press.

[DeKieviet et al., 1997] DeKieviet, M., Dubbers, D., Klein, M., Schmidt, C., and Skrzipczyk, M. (1997). Surface science using molecular beam spin echo. *Surf. Sci.* **377-379**, 1112.

[DeKieviet et al., 1995] DeKieviet, M., Dubbers, D., Schmidt, C., Scholz, D., and Spinola, U. (1995). ^{3}He Spin Echo: New Atomic Beam Technique for Probing Phenomena in the neV Range. *Phys. Rev. Lett.* **75**, 1919.

[Derjaguin and Abrikossova, 1954] Derjaguin, B. V. and Abrikossova, I. I. (1954). *Disscuss. Faraday Soc.* **18**, 24.

[Doak and Chizmeshya, 2001] Doak, R. B. and Chizmeshya, A. V. G. (2001). Sufficiency conditions for quantum reflection. *Europhys. Lett.* **51**, 381.

[Doyle et al., 1991] Doyle, J. M., Sandberg, J. C., Yu, I. A., Cesar, C. L., Kleppner, D., and Greytak, T. J. (1991). Hydrogen in the Submillikelvin Regime: Sticking Probability on Superfluid ^{4}He. *Phys. Rev. Lett.* **67**, 603.

[Druzhinina and DeKieviet, 2002] Druzhinina, V. and DeKieviet, M. (2002). Experimental Observation of Quantum Reflection far from Threshold. http://lanl.arxiv.org/abs/quant-ph/0212076.

[Druzhinina et al., 2003] Druzhinina, V., Stöferle, T., and DeKieviet, M. (2003). Measurement of the Attractive Atom-Conductive Surface Casimir Force. To be published.

[Dzyaloshinskii et al., 1961] Dzyaloshinskii, I. E., Lifshitz, E. M., and Pitaevskii, L. P. (1961). The general theory of van der Waals Forces. *Adv. Phys.* **10**, 165.

[Eberlein, 1996] Eberlein, C. (1996). Sonoluminescence as Quantum Vacuum Radiation. *Phys. Rev. Lett.* **76**, 3842.

[Eltschka et al., 2000] Eltschka, C., Moritz, M. J., and Friedrich, H. (2000). Near-threshold quantization and scattering for deep potentials with attractive tails. *J. Phys. B: At. Mol. Opt. Phys.* **33**, 4033.

[Friedrich, 1994] Friedrich, H. (1994). In: *Theoretische Atomphysik* , p. 45. Springer Verlag.

[Friedrich et al., 2002] Friedrich, H., Jacoby, G., and Meister, C. G. (2002). Quantum reflection by Casimir-van der Waals potential tails. *Phys. Rev. A* **65**, 032902.

[Hafner, 1999] Hafner, S. (1999). *Messung dynamischer Systeme mit dem ^{3}He-Spinecho-Spektrometer.* Dissertation University of Heidelberg.

[Haken and Wolf, 1993] Haken, H. and Wolf, H. C. (1993). In: *Atom- und Quantenphysik* , p. 304. Springer Verlag.

[Hellwege, 1981] Hellwege, K. H. (1981). In: *Einfürung in die Festkörperphysik* , p. 30. Springer Verlag.

[Henkel et al., 1997] Henkel, C., Moller, K., Kaiser, R., Vanteenkiste, N., Westbrook, C. I., and Aspect, A. (1997). Diffuse atomic reflection at a rough mirror. *Phys. Rev. A* **55**, 1160.

[Henkel et al., 1996] Henkel, C., Westbrook, C. I., and Aspect, A. (1996). Quantum reflection: atomic matter-wave optics in an attractive exponential potential. *J. Opt. Soc. Am. B* **13**, 233.

[Israelachvili, 1985] Israelachvili, J. N. (1985). In: *Intermolecular and surface forces*. Akademie Press.

[Israelachvili and Adams, 1978] Israelachvili, J. N. and Adams, G. E. (1978). *J. Chem. Soc. Faraday Trans. 1* **74**, 975.

[Jones, 2000] Jones, K. (2000). Polarizability of Helium. http://www.physics.uq.edu.au/people/jones/phys6040/tut04/node4.html.

[Klimchitskaya et al., 1999] Klimchitskaya, G. L., Roy, A., Mohideen, U., and Mostepanenko, V. M. (1999). Complete roughness and conductivity corrections for Casimir force measurement. *Phys. Rev. A* **60**, 3487.

[Kunc and Shemansky, 1985] Kunc, J. A. and Shemansky, D. E. (1985). The Potential Curve of the He-α-quartz Surface Interaction. *Surf. Sci.* **163**, 237.

[Lambrecht et al., 1996] Lambrecht, A., Jaekel, M.-T., and Reynaud, S. (1996). Motion Induced Radiation from a Vibrating Cavity. *Phys. Rev. Lett.* **77**, 615.

[Landau and Lifschitz, 1985] Landau, L. D. and Lifschitz, E. M. (1985). In: *Lehrbuch der Theoretischen Physik*. Akademie Verlag, Berlin.

[Lang, 1998] Lang, F. (1998). Coronen auf rekonstruiertem Gold(111). Untersuchungen mit dem ^{3}He-Spinecho-Spektrometer. Diplomarbeit University of Heidelberg.

[Lennard-Jones and Devonshire, 1936] Lennard-Jones, J. E. and Devonshire, A. F. (1936). *Proc. R. Soc. London* **Ser. A**, 6(36).

[Lifshitz and Pitaevskii, 1980] Lifshitz, E. M. and Pitaevskii, L. P. (1980). In: *Statistical Physics, Part 2*. Pergamon Press, Oxford.

[Lüth, 1993] Lüth, H. (1993). In: *Surfaces and Interfaces of Solids* , p. 430. Springer Verlag.

[Maradudin and Mazur, 1980] Maradudin, A. A. and Mazur, P. (1980). Effects of surface roughness on the van der Waals force between macroscopic bodies. *Phys. Rev. B* **22**, 1677.

[Marinescu et al., 1997] Marinescu, M., Dalgarno, A., and Babb, J. F. (1997). Retarded long-range potentials for the alkali-metal atoms and a perfectly conducting wall. *Phys. Rev. A* **55**, 1530.

[Mazur and Maradudin, 1981] Mazur, P. and Maradudin, A. A. (1981). Effects of surface roughness on the van der Waals force between macroscopic bodies. 1. Two rough surfaces. *Phys. Rev. B* **23**, 695.

[Milonni, 1994] Milonni, P. W. (1994). In: *The Quantum Vacuum.* Akademie Press.

[Mohideen and Roy, 1998] Mohideen, U. and Roy, A. (1998). A Precision Measurement of the Casimir force between 0.1 to 0.9 mm. *Phys. Rev. Lett.* **81**, 4549.

[Mostepanenko and Trunov, 1997] Mostepanenko, V. M. and Trunov, N. N. (1997). In: *The Casimir Effect and Its Applications.* Clarendon Press.

[Nayak et al., 1983] Nayak, V. U., Edwards, D. O., and Masuhara, N. (1983). Scattering of ^{4}He Atoms Grazing the Liquid-^{4}He Surface. *Phys. Rev. Lett.* **50**, 990.

[NIST, 1999] NIST (1999). http://physics.nist.gov/.

[Pokrovskii et al., 1958] Pokrovskii, V. L., Savvinykh, S. K., and Ulinich, F. K. (1958). Reflection from a barrier in the quasi-classical approximation. *Sov. Phys. JETP* **34**, 879.

[Polyanin and Zaitsev, 1996] Polyanin, A. D. and Zaitsev, V. F. (1996). In: *Handbuch der Linearen Differentialgleichungen* , p. 46. Spectrum Akad. Verlag, Heidelberg.

[Reetz-Lamour, 2001] Reetz-Lamour, M. (2001). Messungen an $^4\mathrm{He}_N$-Clustern mit dem ^{3}He-Spinecho-Spektrometer. Diplomarbeit University of Heidelberg.

[Rowntree, 1990] Rowntree, P. A. (1990). *The Characterization of Layers of Polar Molecules Physisorbed on Single Crystal Graphite using Helium Atom Diffraction.* Dissertation Princeton University.

[Schmidt, 1996] Schmidt, C. (1996). *Entwicklung, Aufbau und Erprobung eines ^{3}He-Atomstrahl-Spinecho-Spektrometers für die Untersuchung des dynamischen Verhältnis zweidimensioneler Systeme.* Dissertation University of Heidelberg.

[Schmidt, 2002] Schmidt, U. (2001-2002). Private communication.

[Segev et al., 1997] Segev, B., Côté, R., and Raizen, M. G. (1997). Quantum reflection from an atomic mirror. *Phys. Rev. A* **56**, R3350.

[Shimizu, 2001] Shimizu, F. (2001). Specular Reflection of Very Slow Metastable Neon Atoms from a Solid Surface. *Phys. Rev. Lett.* **86**, 987.

[Shimizu and Fujita, 2002] Shimizu, F. and Fujita, J. (2002). Giant Quantum Reflection of Neon Atoms from a Ridged Silicon Surface. *J. Phys. Soc. J.* **71**, 5.

[Spruch and Tikochinsky, 1993] Spruch, L. and Tikochinsky, Y. (1993). Elementary approximate derivations of some retarded Casimir interactions involving one or two dielectric walls. *Phys. Rev. A* **48**, 4213.

[Stöferle, 2001] Stöferle, T. (2001). Untersuchungen an den Adsorbatsystemen Xe/Au(111) und Alkanthiole/Au(111) mit dem ^{3}He-Spinecho-Spektrometer. Diplomarbeit University of Heidelberg.

[Sukenik et al., 1993] Sukenik, C. I., Boshier, M. G., Cho, D., Sandoghdar, V., and Hinds, E. A. (1993). Measurement of the Casimir-Polder Force. *Phys. Rev. Lett.* **70**, 560.

[Teichert, 1999] Teichert, H. (1999). Untersuchungen mit dem ^{3}He Spinechospektrometer: Coronen auf Gold(111). Diplomarbeit University of Heidelberg.

[Tikochinsky and Spruch, 1993] Tikochinsky, Y. and Spruch, L. (1993). Retarded Casimir interaction in the asymptotic domain of an electron and a dielectric wall. *Phys. Rev. A* **48**, 4223.

[Vidali et al., 1991] Vidali, G., Ihm, G., Kim, H.-Y., and Cole, M. W. (1991). Potentials of Physical Adsorption. *Surf. Sci. Rep.* **12**, 133.

[Webster et al., 1980] Webster, G. D. L., Chester, M., Webster, E., and Oestereich, T. (1980). *J. Low Temp. Phys.* **40**, 207.

[Yu et al., 1993] Yu, I. A., Doyle, J. M., Sandberg, J. C., Cesar, C. L., Kleppner, D., and Greytak, T. J. (1993). Evidence for Universal Quantum Reflection of Hydrogen from Liquid ^{4}He. *Phys. Rev. Lett.* **71**, 1589.

[Zimmerman and Berlinsky, 1983] Zimmerman, D. S. and Berlinsky, A. J. (1983). The sticking probability for hydrogen atoms on the surface of liquid ^{4}He. *Can. J. Phys.* **61**, 508.

Danksagung

Ich möchte mich bei all denjenigen bedanken, die während meiner Promotion am Physikalischen Institut dazu beigetragen haben, dass die Zeit schön und erfolgreich war:

...Maarten DeKieviet, für die Freiheit, die er mir gegeben hat, für das Vertrauen in meine Rechnungen ("Du, Theoretikerin...") und die Geduld bei Diskussionen und gemeinsamen Paper-Schreiben,

...Die Konrad-Adenauer-Stiftung, für die finanzielle Unterstützung, die mir die Durchfürung meiner Arbeit ermöglicht hat, und für lehrreiche Stipendiatentreffen und Seminare,

...Christian Schmidt und Thilo Stöferle, für die experimentallen Daten, bei dessen Auswertung ich auch die theoretische Formeln besser verstehen konnte,

...Frank Lang und (nochmal) Thilo Stöferle, für ständige und geduldige Hilfe in meinem Kampf mit dem Computer,

...Ulrich Schmidt (Utz), für freundliche Unterstützung, die Bereitschaft über jede Frage zu diskutieren und die unschätzbare Möglichkeit gleich von meinem Arbeitsplatz aus die schnellsten Prozessoren zu benutzen,

...meinen Kollegen: Martin Dürr, Ruth Barth, Simon Aigner, Sascha Epp und Lodewijk Arntzen, für nette Gespräche im Büro und ein schönes Arbeitsklima,

...den Ehemaligen: Markus Reetz-Lamour, Matthias Theis, Jens Herbig und Frank Eisele, für die Unterstützung in der ersten Phase meiner Arbeit,

...den Neutronphysikern: Hartmut Abele, Daniela Mund, Markus

Brehm, Thomas Ferger, Frank Rüss, Barbara Böhm, Kerstin Schindler, Martin Klein, Bastian Märkisch, Verner Hinderer, Andreas Hillenbach, Michael Kreuz, Arnd Gildemeister und Marc Schumann, für die netten Treffen bei Seminaren und unterhaltsames Kuchenessen,

...Prof. Dubbers, für seiner Engagement in Fragen der allgemeinen Bildung der Gruppe und seine ansteckende Energie,

...die Sekräterinnen: Frau Wallenwein und Frau Krämer, für ihre Hilfe beim ganzen Dokumenten-Kram,

...meinen Freunden, für immer gefundene warme Worte und die besondere Unterstützung in der letzten Phase meiner Arbeit,

...meine Familie, die am meisten gelitten hat deswegen, dass ich keine Zeit für Besuche hatte, und die Familie meines Freundes, die immer grossen Anteil an meiner Arbeit genommen hat,

...meinen liebsten Freund Marcel Mudrich, ohne dem und seine liebe- und geduldvolle Unterstützung, ich mir die Promotionszeit gar nicht vorstellen kann,

...und schliesslich mein noch ungeborenes Baby, das den ganzen Stress den letzten Arbeitsmonate mit mir teilen musste.